ABSTRACT

Title of Dissertation:	Additive Manufacturing of Microfluidic Technologies *via In Situ* Direct Laser Writing
	Abdullah T. Alsharhan, Doctor of Philosophy, 2021
Dissertation directed by:	Assistant Professor, Ryan D. Sochol, Department of Mechanical Engineering

Innovations in microfluidic technologies hold great promise for a wide range of chemical, biomedical, and soft robotic applications. Unfortunately, key drawbacks associated with soft lithography-based microfabrication processes hinder such progress. To address these challenges, we advance a novel submicron-scale additive manufacturing (AM) strategy, termed "*in situ* direct laser writing (*is*DLW)". *Is*DLW is an approach that benefits from the architectural versatility and length scales inherent to two-photon polymerization (2PP), while simultaneously supporting the micro-to-macro interfaces required for its effective utilization in microfluidic applications. In this dissertation, we explore *is*DLW strategies that enable passive and active 3D microfluidic technologies capable of enhancing "on-chip" autonomy and sophistication. Initially, we use poly(dimethylsiloxane) (PDMS)-based *is*DLW to fabricate microfluidic diodes that enable unidirectional rectification of fluid flow. We introduce a novel cyclic olefin polymer (COP)-based *is*DLW strategy to address several

limitations related to structural adhesion and compatibility of PDMS microchannels. We use this COP-based approach to print microfluidic transistors comprising flexible and free-floating components that enable both "normally open" (*NO*) and "normally closed" (*NC*) functionalities—*i.e.*, source-to-drain fluid flow (Q_{SD}) through the transistor is either permitted (*NC*) or obstructed (*NO*) when a gate input (P_G) is applied. As an exemplar, we employ COP-based *is*DLW to print an integrated microfluidic circuit (IMC) comprised of soft microgrippers downstream of *NC* microfluidic transistors with distinct P_G thresholds. All of these microfluidic circuit elements are printed within microchannels $\leq$ 40 μm in height, representing the smallest such components (to our knowledge). Theoretical and experimental results illustrate on the operational efficacy of these components as well as characterize their performance at different input conditions, while IMC experimental results demonstrate sequential actuation of the microrobotic components to realize target gripper operations with a single P_G input. Furthermore, to investigate the utility of this strategy for static microfluidic technologies, we fabricate: (*i*) interwoven bioinspired microvessels (inner diameters < 10 μm) capable of effective isolation of distinct microfluidic flow streams, and (*ii*) deterministic lateral displacement (DLD) microstructures that enable continuous sorting of submicron particles (860 nm). In combination, these results suggest that the developed AM strategies offer a promising pathway for advancing state-of-the-art microfluidic technologies for various biological and soft robotic applications.

ADDITIVE MANUFACTURING OF MICROFLUIDIC TECHNOLOGIES *VIA IN SITU* DIRECT LASER WRITING

by

Abdullah T. Alsharhan

Dissertation submitted to the Faculty of the Graduate School of the
University of Maryland, College Park, in partial fulfillment
of the requirements for the degree of
Doctor of Philosophy
2021

Advisory Committee:
  Professor Ryan Sochol, Chair
  Professor Don DeVoe
  Professor Axel Krieger
  Professor Eleonora Tubaldi
  Professor Reza Ghodssi, Dean's Representative

Dedication

I dedicate this work to my parents and my family. This was only possible with your endless love, support, and sacrifice.

Acknowledgements

I would like to first recognize and thank my advisor Prof. Ryan Sochol. He invested a great deal of time and effort as he mentored me through the past three and a half years, for which I will forever be indebted. I'm thankful for the thought-provoking feedback he shared during our discussions, and for his invaluable guidance and contributions in preparing our journal manuscripts and conference presentations. But most of all, I'm truly grateful for the productive and creative environment he helped sustain with continuous support and encouragement, and for the patience and understanding he showed when addressing our disagreements. In short, thank you Dr. Sochol for making this challenging experience both rewarding and enjoyable, I don't know many in my place who can say the same.

I would also like acknowledge my fellow lab mates, and close friends, who worked by my side since the start of my PhD journey, Andrew Lamont, Michael Restaino, and Ruben Acevedo. Their knowledge and expertise were a valuable resource that benefited my work in many aspects and assisted me with my experiments on several occasions. Specifically, I'm grateful to Andrew Lamont for taking me under his wing when I first joined the team and for showing me the ropes around the lab. I learned a lot from working with him on our first project and am thankful for his contributions which included the sol-gel channel coating as well as the design, fabrication, and burst-pressure experimentation with the fluidic barriers (highlighted in chapter 1). I'm also very thankful to Michael Restaino for his instrumental help with the different equipment around the lab, and for his feedback during the initial phase of creating the

COP-COP microdevice fabrication procedures. I'm also really appreciative of Ruben Acevedo's contribution in the work presented in chapter 2. He produced the CAD models and conceptual illustrations for the microvessels and microfluidic transistor and helped with testing the microfluidic barriers. My appreciation also goes to all my fellow BAM lab members, and to the undergraduate researchers, especially Anthony Stair, who worked by my side and helped me with my projects by fabricating COP microfluidic platforms and by assisting me with my experiments. I also extend my gratitude to the new PhD students who recently joined our lab in 2020. Specifically, to Olivia Young and Xin Pannie Xu, they also helped in generating most of the figures and illustrations presented in chapter 3.

Outside of our BAM lab family, I would like to thank Dr. Don DeVoe and his team, especially Dr. Jung Yeon Han, for their input on the fabrication process of the COP microfluidic platforms. Additionally, I extend my appreciation to Dr. Roseanne Warren and Talha Razaulla from the University of Utah for their involvement and contributions to the work featured in chapter 4. The experimental nature of the work presented here makes it so that it is highly dependent on the ability to access different facilities and equipment. For that, I extend my gratitude to TerrapinWorks Research Prototyping Laboratory staff for providing training and access to the Nanoscribe 3D printer, as well as to the staff of the Nanocenter and AIM lab at the University of Maryland for providing training and access to the clear-room facilities and scanning electron microscopy (SEM) equipment.

Table of Contents

List of Figures

List of Abbreviations

3D	Three-dimensional
APTES	(3-Aminopropyl)triethoxysilane
DLD	Deterministic Lateral Displacement
CAD	Computer-Aided Design
CAM	Computer-Aided Manufacturing
CCD	Charge-Coupled Device
COP	Cyclic Olefin Polymer
D_C	Critical Diameter
DiLL	Dip-in Laser Lithography
DLW	Direct Laser Writing
$\mathrm{D_P}$	Particle Diameter
DRIE	Deep Reactive Ion Etching
FDA	United States Food and Drug Administration
FDM	Fused Deposition Modeling
FEA	Finite Element Analysis
FEP	Fluorinated Ethylene-Propylene
FSI	Fluid-Structure Interaction
G	Post-to-post Gap
IPA	Isopropyl Alcohol
IMC	Integrated Microfluidic Circuit
*is*DLW	In-Situ Direct Laser Writing
MFCS	Microfluidic Control System

N.A.	Numerical Aperture
NC	Normally closed
NO	Normally Open
PDMS	Polydimethylsiloxane
P_G	Gate Pressure
PGMEA	Propylene Glycol Monomethyl Ether Acetate
PMMA	Poly(methyl methacrylate)
P_S	Source Pressure
PS	Polystyrene
Q_{SD}	Source-to-Drain Flow rate
SEM	Scanning Electron Microscopy
SLA	Stereolithography
STL	Standard Triangle Language

List of Supplementary Movies

Movie 1.1. CAM simulation (Left) and corresponding *is*DLW fabrication results (Right) for the *is*DLW -based printing of a microfluidic barrier wall structure (10 μm in thickness) within a sol-gel-coated PDMS microchannel with a triangular cross-sectional profile and a height of 50 μm. Video speed = 4x; Scale bar = 50 μm.

Movie 1.2. Deflection behavior of an *is*DLW -printed helical coil spring in response to varying pressure input. Video speed = 10x; Scale bar = 40 μm

Movie 1.3. Theoretical simulation results for the microfluidic coil spring diode under (a) forward flow, and (b) reverse flow conditions. Structure color represents displacement in μm; Arrows represent fluid velocity field vectors.

Movie 1.4. *Is*DLW fabrication results for printing a 3D microfluidic coil spring diode within a sol-gel-coated PDMS-on-glass microchannel with a semi-ovular cross-sectional profile and height of ~25 μm. Video speed = 6x; Scale bar = 10 μm.

Movie 1.5. Deformation behavior of the PDMS channel during the transition from pressures of 0 kPa to 150 kPa applied in the (a) forward flow direction (*rightward*), and (b) reverse flow direction (*leftward*). Scale bar = 10 μm.

Movie 2.1. Fabrication of a 100-μm-tall trapezoidal microchannel negative master mold pattern onto a Si substrate *via* "stitching"-based DLW. Video speed = 30x; Scale bar = 100 μm.

Movie 2.2. Fabrication results for *is*DLW-printing of a 10-μm-thick fluidic barrier structures inside a 100-μm-tall channel with (**a**) rectangular, (**b**) trapezoidal, and (**c**) semi-elliptical cross-sectional profiles by varying the laser power with height. Video speed = 10x; Scale bar = 25 μm.

Movie 2.3. CAM simulations (*left*) and corresponding fabrication results (*right*) for the *is*DLW printing process of interwoven microvessel- inspired structures. Video speed = 30x; Scale bar = 50 μm.

Movie 2.4. Experimental results for COP-based *is*DLW-printed microvessel-inspired structures during loading of rhodamine B-labelled fluid (*pink*) and methylene blue-labelled fluid (*blue*). Scale bar = 50 μm.

Movie 2.5. Results for COMSOL Multiphysics fluid-structure interaction (FSI) simulations of fluid velocity field (*colored arrows*) and displacement distributions for the 3D microfluidic bellow-type *NO* transistor with P_S = 10 kPa and P_G increasing from 0 kPa to 90 kPa.

Movie 2.6. CAM simulations (*left*) and corresponding fabrication results (*right*) for the *is*DLW printing process of the *NO* microfluidic transistor. Video speed = 15x; Scale bar = 50 μm.

Movie 2.7. Experimental results for the microfluidic bellow-type *NO* transistor during dynamic operation of the gate. Video speed = 5x; Scale bar = 50 μm.

Movie 2.8. Microfluidic loading of a methylene blue-labelled fluid into the gate region of a 3D microfluidic bellow-type *NO* transistor *is*DLW-printed inside of a PDMS-on-glass device. Scale bar = 50 μm.

Movie 2.9. Microfluidic loading of a rhodamine B-labelled fluid and a methylene blue-labelled fluid into the source-to-drain region and gate region, respectively, of a 3D microfluidic bellow-type transistor *is*DLW-printed inside of a COP-COP device. Scale bar = 50 μm.

Movie 3.1. CAM simulations (*left*) and corresponding fabrication results (*right*) for the *is*DLW printing process of the *NC* microfluidic transistor. Video speed = 30x; Scale bar = 50 μm.

Movie 3.2. Experimental results for the microfluidic *NC* transistor during dynamic operation of the gate, and floating disc actuation. Video speed = 2x; Scale bar = 25 μm.

Movie 3.3. CAM simulations (*left*) and corresponding fabrication results (*right*) of a 40-μm-tall trapezoidal microchannel negative master mold for the IMC onto a Si substrate. Total time ≈ 16 min. Video speed = 10x; Scale bar = 25 μm.

Movie 3.4. CAM simulations (*left*) and corresponding fabrication results (*right*) for the *is*DLW printing process of the *soft microrobotic grippers*. Video speed = 4x; Scale bar = 50 μm.

Movie 3.5. Experimental results for the single *NC* transistor and soft microgripper pair during actuation. Video speed = 1x; Scale bar = 50 μm.

Movie 3.6. Experimental results for the IMC with two *NC* transistor and soft microgripper pairs during operation. Video speed = 1x; Scale bar = 50 μm.

Introduction

Recent advances in the capabilities of additive manufacturing or “three-dimensional (3D) printing” technologies have dramatically expanded the degree of architectural freedom with which researchers can design and manufacture systems at micron-to-submicron scales [1,2]. At present, extrusion-based methods (*e.g.*, direct ink writing) have garnered significant interest in the scientific community due to the vast material selection and low equipment costs afforded by such approaches [3–5]. The key limitations, however, stem from the condition that the nozzle be physically positioned at each location of material deposition, which not only increases printing times, but also prevents the fabrication of structures for which nozzle access is obstructed [6,7]. In addition, challenges associated with nozzle-material interactions and controls have typically restricted the utility of extrusion-based methods to structures with feature sizes of approximately 10 μm or larger [8]. Thus, for 3D printing applications at smaller scales, researchers have focused on utilizing an alternative technology called direct laser writing (DLW) [9–11].

Direct Laser Writing (DLW)

DLW is a 3D manufacturing approach that relies on using tightly focused femtosecond laser pulses to initiate spatially controlled polymerization of a liquid-phase photocurable material *via* two-photon (or multi-photon) absorption phenomena [12–15]. It has emerged as an unparalleled 3D manufacturing technology for the fabrication of structures with feature resolutions on the order of 100 nm [16–18]. A fundamental trade-off inherent to DLW, however, is that the submicron feature size of the curing voxel is poorly suited for fabricating the macro-to-micro interfaces – *i.e.*, inlet and outlet fluidic access ports – that are requisites for DLW-based microfluidic applications [19,20]. Consequently, DLW-based studies have predominantly involved the use of unenclosed micro and nanostructures [21–23]. Nonetheless, due to the potential of DLW for fluidic applications [24], an increasing number of groups have developed methods to facilitate the aforementioned macro-to-micro interfaces.

Previously, researchers have reported two main classes of techniques for using DLW to additively manufacture fluidic systems: (*i*) full device printing, and (*ii*) *in situ* fabrication. Recently, Marino *et al*. demonstrated an example of the former in which a complete system comprised of 3D microfluidic blood-brain barrier models that are fully integrated with larger-scale coupling ports (*i.e.*, for the manual insertion of external tubing) was constructed in a single print run [25]. Although only two coupling ports were manufactured (one input and one output), using DLW to generate multiple structures with feature sizes in the meso-to-milliscale range typically requires print times on the order of days, times that would be compounded in cases that demand additional input and/or output coupling ports. As a result, researchers have primarily refrained from using DLW exclusively to manufacture entire devices, opting instead for hybrid protocols that rely on standard micromanufacturing methods for bulk device fabrication, with DLW utilized only for *in-situ* fabrication of critical 3D nanostructured features [26–29].

In Situ Direct Laser Writing (isDLW)

In situ DLW (*is*DLW) encompasses a variety of approaches that involve first manufacturing a microfluidic channel using alternative fabrication processes (*e.g.*, micromolding or laser ablation), then inputting a photocurable material into the microfluidic channel, and lastly, using DLW to print structures directly inside of the channel [30]. Researchers have utilized a number of microchannel materials for *is*DLW. For example, although glass microchannels are compatible with *is*DLW processes [31–34], the protocols for manufacturing glass microdevices, such as laser ablation and wet etching (*e.g.*, with HF), are typically associated with undesired fabrication times, costs, labor requirements and/or safety concerns [35]. As a result, many groups have instead employed soft lithography protocols with PDMS to demonstrate *is*DLW with PDMS-on-glass microchips [36,37]. One challenge associated with the gas permeability of PDMS is that a thin oxygen layer on the channel surface can disrupt photopolymerization phenomena, which while beneficial to applications including optofluidic lithography and continuous liquid interface production [38–40], can lead to print failures for *is*DLW. Consequently, *is*DLW for PDMS-on-glass systems typically involves printing structures onto the glass surface (rather than PDMS surfaces) of the microchannel interior [36,37]. Other groups have developed PDMS-photoresist-glass sandwich-chip approaches in which 3D structures are first printed in unenclosed photoresist-on-glass channels, and then a PDMS slab is sealed atop the photoresist to form enclosed microchannels (with DLW-based structures sealed only to the photoresist sidewalls and glass base) [26–28].

The efficacy of *is*DLW for fluidic applications is predicated on new methods that yield full sealing interactions between DLW-printed structures and the entire luminal surface of the microchannel, while bypassing limitations inherent to glass microchip fabrication. Recently, our group has observed that using *is*DLW to build microfluidic structures within soft lithography-based PDMS-on-glass devices can lead to malformed prints at taller heights (≥ 50 μm) [41], and consistent with prior works, diminish sealing performance at PDMS interfaces. To limit the effects of these failure modes, Lölsberg *et al*. utilized a PDMS-on-glass device with trapezoidal microchannels (~30 μm in height) to manufacture a microfluidic spinneret head *via* an inverted *is*DLW process [42]; however, persisting sealing issues necessitated the inclusion of additional intersecting sacrificial channels for silane-based glues to be manually loaded in an effort to improve mechanical and sealing integrity. Although fluidic experimentation (*e.g*., burst-pressure measurements) to assess the influence of the silane-based glue on sealing performance was not reported, the results suggest a possible role for microchannel geometry in *is*DLW.

Outline

In **chapter 1** of this work, we address the structural sealing limitation of *is*DLW structures printed in PDMS-on-glass microchannels by presenting a sol-gel-based *is*DLW strategy [43], where we investigate the role of the coating process as well as the microchannel geometry (*e.g.*, cross-sectional shape and size) in the sealing performance of *is*DLW-printed structures. Additionally, and as a demonstrative example, we employ this strategy to 3D print a microfluidic helical coil spring diode and characterize its fluid flow rectification performance. Although the application of a sol–gel coating to PDMS-on-glass microchannels improved structure-to-channel adhesion of *is*DLW-printed microstructures, sealing performance was compromised at higher pressures (e.g., operational pressures <50–75 kPa). Furthermore, employing *is*DLW with PDMS-on-glass microdevices also restricted which developers can be used following the printing process, as many conventional DLW developers are organic solvents that can degrade PDMS [42–44].

To bypass these issues, in **chapter 2**, we explore – for the first time – the use of Cyclic Olefin Polymer (COP) as an enabling microchannel material for *is*DLW [45] by investigating three fundamental classes of microfluidic systems corresponding to increasing degrees of sophistication: (*i*) functionally static fluidic barriers (10–100 μm in height), which supported uncompromised structure-to-channel sealing under applied input pressures of up to 500 kPa; (*ii*) 3D static interwoven microvessel-inspired structures (inner diameters < 10 μm); and (*iii*) 3D dynamically actuated *NO* microfluidic transistors, which comprises bellowed sealing elements (wall thickness ≈

500 nm) that could be actively deformed *via* an applied gate pressure to fully obstruct source-to-drain fluid flow. Results from investigating these systems suggest that COP-based isDLW offers a promising pathway for microfluidic applications that demand significant architectural versatility with invariable sealing integrity.

In **chapter 3**, we leverage our COP-based *is*DLW process to first introduce *NC* microfluidic transistors that comprise bellowed elements and free-floating sealing discs designed to block source-to-drain fluid flow until a target gate pressure (P_G) is applied [46]. We then theoretically and experimentally investigate the performance of the transistor, as well as characterize the effect that geometric variations in the disc size have on the gate activation pressure. Next, as an exemplar, we print microfluidic transistors with distinct gate activation properties as well as identical soft microgrippers downstream of each drain to demonstrate controlled actuation of the microgrippers – by varying the magnitude of a single gate input – in an integrated microfluidic circuit (IMC) [47].

In **chapter 4**, we employ the developed COP-based process (with a slight modification to the device fabrication order and print configuration) to facilitate size-based sorting of nanoparticles [48]. Specifically, we print a structure that is based on DLD microfluidic technology. DLD is a technique in which micro/nanoposts arrayed inside of a microfluidic channel enable transport of target suspended particles away from their initial flow streams. It is a passive technology that relies on geometric design variables, such as the gap spacing between the arrayed posts, to induce the hydrodynamic effect required for particle separation. For applications that involve DLD processing of submicron-scale particles (e.g., extracellular vesicles), however, achieving the requisite geometric control via conventional microfabrication protocols represents a technically challenging manufacturing hurdle. To bypass such barriers, we explore the use of two-photon DLW to additively manufacture DLD arrays capable of submicron particle handling, by demonstrating effective railing of 860 nm fluorescent particles.

Chapter 1: PDMS-based *is*DLW of Microfluidic Diodes

1.1. Scope

In this chapter, we address the structural sealing issues associated with PDMS-on-glass microchannels by introducing a sol-gel-based *is*DLW strategy (**Fig. 1.1**)**.** We utilize this approach to investigate the effects of microchannel geometric factors – namely, channel height and cross-sectional shape – on the sealing performance of *is*DLW-printed structures. Specifically, we employ theoretical and experimental methods to characterize the microfluidic sealing integrity of *is*DLW-printed 10-μm-thick barrier wall structures sealed to sol-gel-coated PDMS-on-glass microchannels with heights of 10, 25, 50, and 100 μm, and six distinct cross-sectional profiles. Three of the microchannel profiles are inspired by those resulting from conventional soft lithography protocols corresponding to: (*i*) deep reactive-ion etching (DRIE) processes that produce relatively straight channel sidewalls [49] (**Fig. 1.2a**), (*ii*) positive-tone photoresists that result in sidewalls that are slightly tapered outward [50] (**Fig. 1.2b**), and (*iii*) negative-tone photoresists that result in inward-tapered sidewalls [51] (**Fig. 1.2c**). Additional microchannel profiles that feature outward-tapering geometries include semi-circular (**Fig. 1.2d**), semi-ovular (**Fig. 1.2e**), and triangular (**Fig. 1.2f**) cross-sections. Additionally, as an exemplar, we examine the flow rectification performance of an *is*DLW-printed 3D microfluidic coil spring diode for which functionality is inextricably linked to luminal microchannel sealing. The presented sol-gel-based *is*DLW protocols and results provide a critical foundation for researchers to bypass the challenges associated with achieving micro-to-macro interfaces and microfluidic sealing, and ultimately, leverage the 3D geometric and scaling-induced benefits of DLW for a diversity of chemical, mechanical, and biological fluidic applications

1.2. PDMS-based isDLW

1.2.1. PDMS-on-Glass Device Fabrication

To fabricate the master molds used for device replication, first, 3D models of the channel designs were created using the computer-aided design (CAD) software, SolidWorks (Dassault Systemes, France). The CAD models were then imported into the computer-aided manufacturing (CAM) software, DeScribe (Nanoscribe GmbH, Germany), and converted to writing-path code. Si substrates (25 mm × 25 mm) were successively rinsed with acetone and isopropyl alcohol (IPA), dried with inert N2 gas, and then baked at 100 °C for 15 minutes. The Nanoscribe Photonic Professional GT (Nanoscribe) was used with a 25× objective lens in DiLL mode to print the master molds comprised of the negative-tone photoresist, IP-S (Nanoscribe), onto the Si substrates (**Fig. 1.1a**). The channel molds were fabricated with layer heights of 1 μm and hatching distances of 500 nm. For DLW, the laser power and scan speed were set to 45 mW and 100 mm/s, respectively. The writing times for the negative master molds were 6, 10.5, 11, and 12.5 minutes corresponding to channel heights of 10, 25, 50, and 100 μm, respectively.

Following the DLW process, substrates were developed first in a bath of propylene glycol monomethyl ether acetate (PGMEA) for 20 minutes, and then in IPA for 2 minutes to remove any remaining uncured photoresist (**Fig. 1.1b**). A 10:1 mixture of PDMS (Sylgard 184, Dow Corning, Corning, NY) was then poured over the master molds and placed on a hot plate set at 60 °C for 3 hours (**Fig. 1.1c**). Cured PDMS was then peeled from the molds and punched to create 0.75 mm inlet and outlet ports. The PDMS was rinsed with IPA, and then O2 plasma bonded to 30 mm circular borosilicate glass substrates (#1.5, Bioptechs Inc., Butler, PA) (**Fig. 1.1d**).

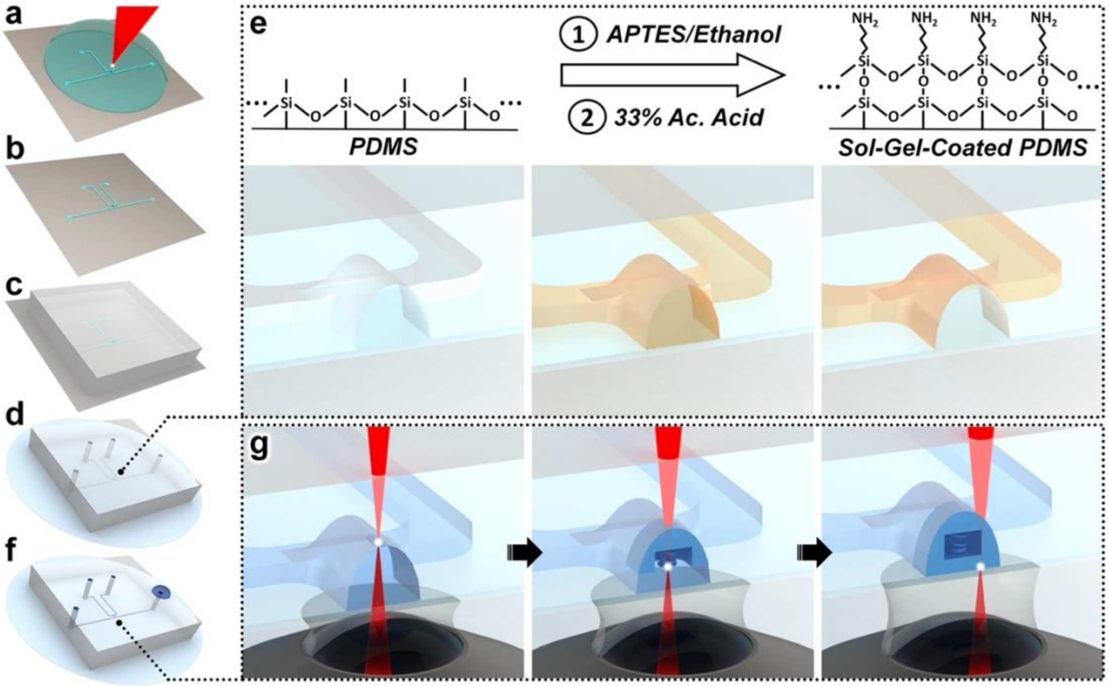

Figure 1.1: *Sol-gel-based isDLW concept. (**a**–**g**) Illustrations of the isDLW fabrication protocol for a microfluidic element printed inside a semi-ovular microchannel. (**a**) DLW of the channel mold structures. (**b**) Fabricated negative master mold. (**c**) Micromolding of PDMS. (**d**) Micromolded PDMS bonded to a glass substrate. (**e**) Acetic (Ac.) Acid-catalyzed sol-gel reaction for coating the PDMS microchannels with an adhesive layer of (3-Aminopropyl)triethoxysilane (APTES). (**f**) Vacuum loading of a liquid-phase photocurable material into the sol-gel-coated microchannels. (**g**) The "ceiling-to-floor" isDLW process. Focused femtosecond laser pulses (red) pass through an objective lens, immersion oil, glass substrate, and liquid-phase photomaterial to initiate spatially controlled photopolymerization (white) in a point-by-point, layer-by-layer methodology, ultimately producing a structure comprised of cured photomaterial (blue) that is fully sealed to the entire luminal surface of the sol-gel-coated microchannel.*

1.2.2. Sol-gel coating

The PDMS-on-glass microfluidic devices were chemically coated using an acid-catalyzed sol-gel reaction presented by Beal *et al*. [52] (**Fig. 1.1e**). First, a solution of 33% APTES in ethanol was perfused into the channels for 5 minutes and cleared with air pressure. Then, a solution of 33% Acetic Acid was perfused into the channel for 3 minutes, catalyzing APTES onto the surface of the PDMS channel. Lastly, the Acetic Acid was cleared from the channels with air pressure, and the device was placed on a hot plate set at 100 °C for 5 minutes.

1.2.3. isDLW Fabrication of Barriers and Microfluidic Diodes

For fabrication of both the barrier wall structures and the 3D microfluidic coil spring diode, 3D models of the designs were created using SolidWorks (Dassault Systemes) and then imported into DeScribe (Nanoscribe) for writing-path code generation. The negative-tone photoresist, IP-L 780 (Nanoscribe), was vacuum-loaded into the sol-gel-coated PDMS-on-glass microchannels (**Fig. 1.1f**). The Nanoscribe Photonic Professional GT (Nanoscribe) was used with a 63× objective lens in oil-immersion mode to print the structures inside of the microchannels (**Fig. 1.1g**). Briefly, this printing strategy involves placing a droplet of immersion oil between the objective lens and the bottom of the glass substrate to maintain the focal path of the laser. All microstructures were printed in a “ceiling-to-floor”, point-by-point, layer-by-layer process. Following *is*DLW completion, the microfluidic devices were placed in a bath of PGMEA for approximately 4 hours. Thereafter, the Fluigent Microfluidic Control

System (MFCS) (Fluigent, France) was used to perfuse PGMEA through the channels for 5 minutes, and then IPA for 1 minute at pressures of <10 kPa.

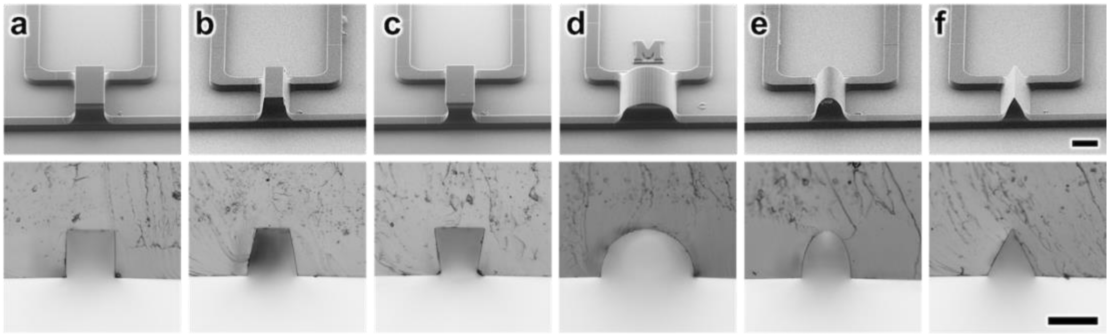

***Figure 1.2**: Micrographs of (Top) DLW-printed negative master molds, and (Bottom) replicated PDMS profiles corresponding to distinct microchannel cross-sectional geometries: (**a**) rectangular (deep reactive-ion etching (DRIE) mimetic), (**b**) outward-tapered (positive-tone photoresist mimetic), (**c**) inward-tapered (negative-tone photoresist mimetic), (**d**) semi-circular, (**e**) semi-ovular, and (**f**) triangular). Scale bars = 100 µm.*

<u>*1.3. Fluidic Sealing Efficacy of Barriers*</u>

1.3.1. Effects of Sol-gel Coating

The methodology presented here utilizes two distinct DLW approaches for two different fabrication roles: (*i*) Dip-in Laser Lithography (DiLL) mode-based DLW for channel mold manufacturing, and (*ii*) *is*DLW for microstructure 3D printing. Previously, several research groups have demonstrated the use of DLW for generating microchannel master molds with arbitrary geometries for elastomer replication [42,53–56]. Here, we utilized the negative-tone photoresist, IP-S, to print negative master molds onto Si substrates *via* DiLL mode-based DLW (**Fig. 1.1a**). Following development (**Fig. 1.1b**), the negative master was used to micromold the silicone elastomer, PDMS (**Fig. 1.1c**). After curing, the PDMS was removed from the molds, hole-punched at inlet and outlet locations, and then plasma-bonded to borosilicate glass substrates (**Fig. 1.1d**).

In prior reports, researchers have presented a variety of protocols for applying sol-gel coatings to microfluidic channels. [57–59] Here, we employed an acid-catalyzed sol-gel reaction developed by Beal *et al*. [52] to chemically coat the inner surface of the PDMS microchannel with (3-Aminopropyl)triethoxysilane (APTES) (**Fig. 1.1e**). Thereafter, we applied previously described microfluidic vacuum-loading approaches [60] to infuse the liquid-phase photoresist, IP-L 780, into the microchannels (**Fig. 1.1f**). For the oil-immersion mode-based *is*DLW step, we utilized a "ceiling-to-floor" DLW strategy in which structures were printed starting at the tallest point of the sol-gel-coated PDMS microchannel (**Fig. 1.1g–*left***). The point-by-point, layer-by-layer DLW routine followed a layering sequence from the top down, with attachment to the glass substrate occurring at the end of the printing process (**Fig. 1.1g–*right***).

After development to remove any residual uncured photoresist, the devices were ready for use and did not require any additional post-processing (*e.g.*, with sealant glues) [42]. The efficacy of the "ceiling-to-floor" *is*DLW protocol is directly linked to the adhesion between the cured photoresist and the top of the PDMS channel, which serves as an anchoring substrate during the layer-by-layer printing process (**Fig. 1.1g**). To initially characterize the influence of the sol-gel coating on the adhesion dynamics, we performed *is*DLW test prints using both uncoated and sol-gel-coated PDMS microchannels. The *is*DLW fabrication results for the uncoated PDMS-on-glass devices revealed structure detachment from the top surface of the microchannel during the printing process–a critical failure mode. In contrast, we did not observe such print failures for cases in which the PDMS microchannels included the sol-gel coating.

1.3.2. Microfluidic Testing Setup

In all experimental tests, MAESFLO software (Fluigent), which operates the MFCS and Flow Rate Platform, was utilized to regulate input pressures and record concurrent pressure and flow rate data during IPA perfusion through microfluidic channels at room temperature (20–25 °C). Microchannels were connected to the MFCS through fluorinated ethylene propylene (FEP) tubing (Cole-Parmer, Vernon Hills, IL) and 20 ga. stainless steel catheter couplers (Instech, Plymouth Meeting, PA). Experiments were conducted on at least three separately fabricated components, and all results were compiled, processed, and plotted using a binning MATLAB script. For burst-pressure testing of the barrier walls, an MFCS pressure source was connected to the device on one side of the barrier, and outlet tubing was connected to the device on the other side of the barrier, while the remaining two ports were sealed with 20 ga. stainless steel plugs (Instech). Flow units were connected in series to the inlet and outlet tubing to record the magnitude of fluid flow on each side of the barrier. A script written in the Fluigent software was used to increase the pressure input in a stepwise manner from 0 kPa to 75 kPa with increments of 2.5 kPa and a 10 s settling time.

1.3.3. Microfluidic Testing of Barrier Structures

To elucidate the role of microchannel geometry in the fluidic sealing performance of *is*DLW-printed structures, we performed burst-pressure experiments for 10-μm-thick fluidic barrier walls constructed in sol-gel-coated PDMS-on-glass microchannels with varying height and cross-sectional shape. We utilized CAM methods to convert 3D models of the barriers to the writing-path code that governs the point-by-point, layer-by-layer positioning of the laser during *is*DLW fabrication. Four primary sets of code were generated corresponding to the four microchannel heights tested: 10, 25, 50, and 100 μm. Specifically, to maintain consistency among experiments, identical barrier wall writing-path code was used for each cross-sectional profile of a given height, with the exception of the semi-circular profiles, which necessitated unique writing-path codes to account for the significantly larger channel widths. The writing-path code was designed for rectangular barrier structures that are slightly larger in width and height than the microchannel cross-sections (**Fig. 1.3–*top***), which resulted in the laser focal point being positioned at various locations inside of the solid PDMS throughout the printing process. Because the photoresist was not present at such locations, however, barrier wall fabrication was inherently restricted to the photoresist-filled microchannel interior, thereby ensuring that the resulting barrier geometry conformed to that of the local channel profile (**Fig. 1.3 – *bottom*; Movie 1.1**).

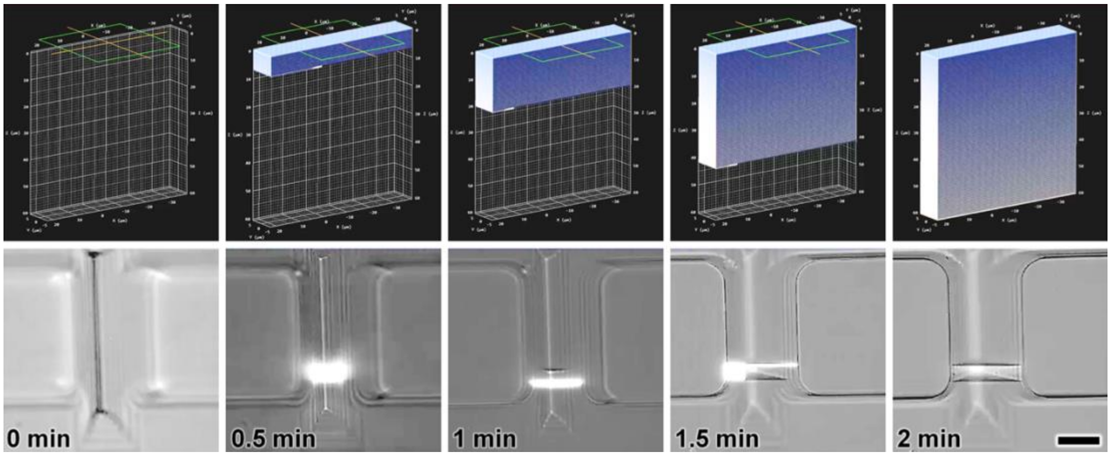

***Figure 1.3**: Sequential CAM simulations (Top) and corresponding isDLW fabrication results (Bottom) for printing a microfluidic barrier wall structure (10 μm in thickness) within a sol-gel-coated PDMS microchannel with a triangular cross-section and height of 50 μm (see also **Movie 1.1**). Scale bar = 25 μm.*

To quantify the burst-pressure dynamics associated with each microchannel height and cross-sectional profile, we incrementally increased the input pressure from 0 kPa to 75 kPa on one side of the *is*DLW-printed barrier wall, while simultaneously monitoring the rate of fluid flow passing (*i.e.*, leaking) through the barrier structure (**Fig. 1.4**). The experimental results revealed three general trends. First, for cases in which fluid leaked past the barrier, we did not observe the types of abrupt changes in flow rate (*e.g.*, a dramatic increase in fluid flow at a critical pressure due to full detachment and dislodgement of the barrier) that are characteristic of fluidic burst-pressure experiments [61]. Instead, we found that the magnitude of leakage flow gradually increased with rising input pressure in such cases. Secondly, decreasing the height of a microchannel for a given profile yielded improvements in the sealing integrity of the 10-μm-thick barrier structures. Lastly, increasing the outward tapering of the microchannel sidewalls typically resulted in enhanced sealing performance.

The three conventional microfabrication-inspired channel profiles provided preliminary insight into the sidewall tapering effects (**Fig. 1.4a-c**). For example, we observed that the overall sealing dynamics for the rectangular (DRIE mimetic) channel profile (**Fig. 1.4a**) appeared to be inferior to those of the outward-tapered (positive-tone photoresist mimetic) profile (**Fig. 1.4b**), while slightly superior to those of the inward-tapered (negative-tone photoresist mimetic) profile (**Fig. 1.4c**). This trend continued for the semi-circular (**Fig. 1.4d**), semi-ovular (**Fig. 1.4e**), and triangular (**Fig. 1.4f**) cross-sectional profiles. For channel heights up to 50 μm, the barrier wall in the semi-circular microchannel effectively obstructed fluid flow for the pressures tested (**Fig. 1.4d**). Due to the 200 μm width of the 100-μm-tall semi-circular channel, a stitching approach was needed to print the barrier structure in two parts– the only case in this study for which a complete barrier could not be printed in a single step. Burst-pressure testing revealed leakage flow from the onset of input pressure (**Fig. 1.4d–*yellow***). Both the semi-ovular (**Fig. 1.4e**) and triangular (**Fig. 1.4f**) channel profiles did not exhibit significant changes in sealing performance over the range of microchannel heights investigated, demonstrating improved sealing efficacy compared to the microchannel profiles inspired by conventional microfabrication techniques (**Fig. 1.4**).

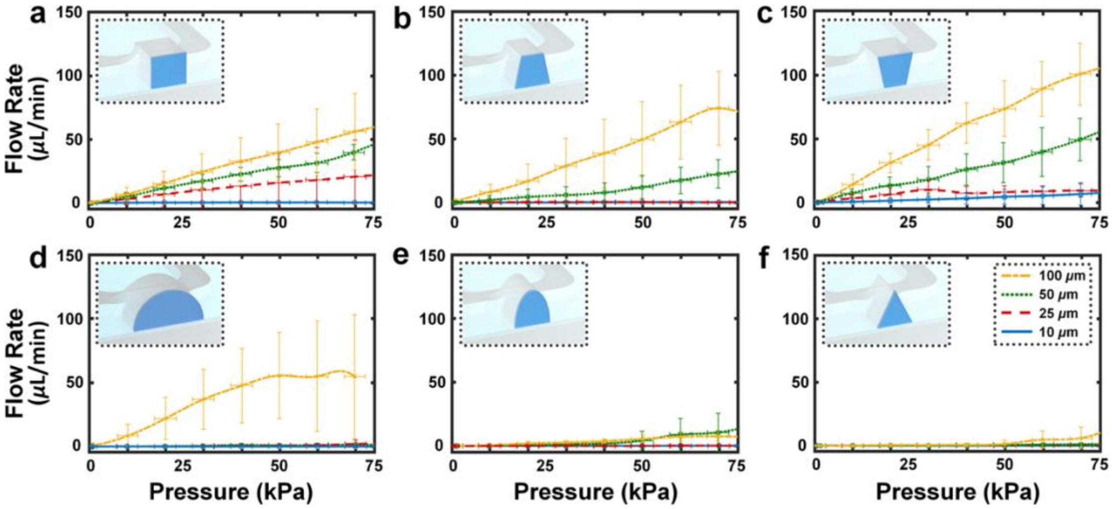

***Figure 1.4**: Experimental results for burst-pressure quantification of isDLW-printed microfluidic barrier wall structures (10 µm in thickness) corresponding to sol-gel-coated PDMS microchannels with 10 µm (blue), 25 µm (red), 50 µm (green), and 100 µm (yellow) channel heights, and (**a**) rectangular, (**b**) outward-tapered, (**c**) inward-tapered, (**d**) semi-circular, (**e**) semi-ovular, and (**f**) triangular cross-sectional profiles. (Insets) Conceptual illustrations of the microfluidic barrier wall structures (dark blue) and microchannel cross-sections corresponding to each profile. Scale bars denote standard deviation corresponding to experiments with three different devices.*

The burst-pressure experiments for the barrier structures also revealed that the shape of the microchannel cross-section serves as a key determinant of microfluidic sealing performance (**Fig. 1.4**). In general, the semi-circular, semi-ovular, and triangular channel profiles outperformed the profiles designed to mimic conventional microfabrication-based microchannels, results that may be due to a number of potential factors. Similar to changes in height, differences in the shape, and in turn, surface area of the barrier structure can lead to disparities in the applied force for a given pressure. Theoretical simulations of the barrier walls revealed that the semi-circular profile resulted in the largest sustained forces and stresses. Thus, if shape-based differences in applied force influence the sealing functions of barriers of the same height, then the semi-circular profile should exhibit the worst performance of all of the profiles examined. Experiments revealed that this was not the case, with the semi-circular geometry yielding superior performance compared to many of the other profiles for heights of 10, 25, and 50 μm (**Fig. 1.4**). These results suggest that force disparities cannot account for the shape-based differences in sealing integrity, which were likely caused by alternative mechanisms.

One of the trends elucidated during burst-pressure testing was that increasing the outward tapering of the microchannel sidewalls generally corresponded to improvements in sealing performance (**Fig. 1.4**). In addition, several cases for the conventional microfabrication-inspired profiles (**Fig. 1.4a-c**) exhibited leakage flow from the onset of pressure testing, which implies the absence of luminal adhesion prior to experiment initiation. A potential basis for these results stems from fabrication issues that led to a lack of sealing continuity between printed barrier structures and the channel walls. In particular, printing in certain locations within the microchannel (*e.g.*, the top corners of the rectangular, inward-tapered, and outward-tapered channels) can lead to unintended focusing deviation caused by interactions between the laser path and the lower portions of the PDMS through which the laser passes. Such disruptions of the laser path can inhibit photopolymerization initiation, thereby preventing curing of the photomaterial in specific locations–a phenomenon termed "shadowing" [42]. Additionally, these effects would be exacerbated in cases with taller channel heights, which include a longer distance in which disruptive laser-PDMS interactions can occur. The observed differences in sealing behaviors associated with the distinct tapering of the various microchannel profiles are consistent with those predicted by shadowing phenomena (**Fig. 1.4**). One note is that it may be possible to mitigate such shadowing effects by dynamically adjusting the laser power and/or scanning speed during the *is*DLW fabrication process to promote photoinitiation in shadowed regions; however, elucidating the optimal parameters to achieve successful prints may be experimentally challenging due to the difficulties in optically characterizing nanostructured features within enclosed microchannels. In contrast, we found that the use of semi-circular, semi-ovular, and triangular channel profiles bypassed the need for such experimental optimizations. Thus, due to the critical requirement for sufficient sidewall tapering in order to avoid shadowing failure modes, the results suggest that conventional soft lithography protocols are ill-suited for *is*DLW.

Although the semi-circular microchannel yielded effective barrier sealing for channel heights up to 50 μm, the 100-μm-tall profile exhibited fluid leakage from the onset of burst-pressure testing (**Fig. 1.4d**). The key difference between the 100 μm case and all of the other barrier structures was that the manufacturing restrictions of the DLW printer (build area ≈125 × 125 μm2) required that the 200-μm-wide barrier wall be fabricated in two separate parts (**Movie 1.2**). The results suggest that for this barrier structure design, effective joining of the two parts did not occur, leading to immediate leakage during testing (**Fig. 1.4d**–***yellow***). Thus, the observed leakage for the 100-μm-tall profile was likely a product of the multi-step fabrication process rather than adhesion issues between the barrier structure and the sol-gel-coated PDMS.

1.4. Microfluidic Diode

A number of groups have demonstrated the considerable advantages associated with using additive manufacturing technologies for the fabrication and integration of microfluidic circuit elements [62–65]. Previously, our group introduced the first 3D printed microfluidic diode – a fluidic circuit element that passively allows fluid to flow in one direction, while obstructing flow in the opposite direction [66]. Despite the functionalities enabled by prior 3D printed microfluidic circuits, the size of such systems has remained relatively large in the meso- to millimeter-scale range. To explore the potential of leveraging *is*DLW to drastically reduce the size of 3D microfluidic circuity, we designed and printed 3D microfluidic coil spring diodes inside of sol-gel-coated PDMS-on-glass microchannels.

The 3D microfluidic coil spring diode in this study comprised a helical coil spring connected to a cylindrical sealing disc and several pathways for fluid flow, including a bottom orifice, an intermediary structure with a center orifice and eight radially arrayed through-holes, and a top orifice (**Fig. 1.5**). Under forward flow conditions, fluid from the microchannel enters the element through the bottom orifice, bringing the sealing disc into contact with the intermediary structure as the coil spring compresses (**Fig. 1.5 – *left***). The intermediary structure serves as a physical boundary to prevent large spring deformations (**Movie 1.2**) that can result in spring/disc misalignment-based failures. Despite the sealing disc blocking flow through the center orifice of the intermediary structure, fluid is able to continue flowing through the radially arrayed through-holes and out the top orifice (**Fig. 1.5 – *left***). When the flow polarity is reversed, however, the coil spring extends to allow the cylindrical disc to seal atop the bottom orifice, thereby physically obstructing fluid flow through the microfluidic diode element (**Fig. 1.5 – *right***).

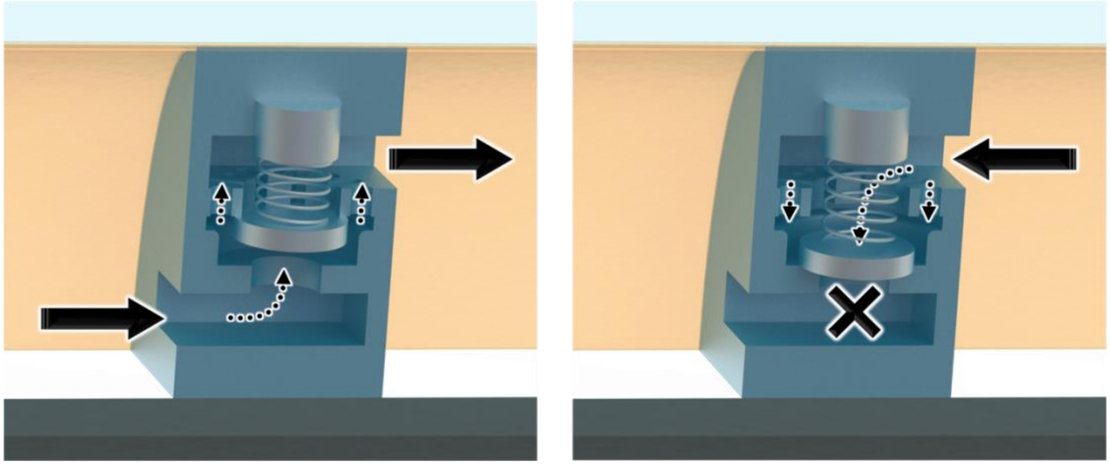

Figure 1.5: *IsDLW-based 3D microfluidic coil spring diode. Conceptual illustrations of flow rectification functionality. (Left) Under forward flow conditions, the helical coil spring compresses as the sealing disc is directed away from the bottom orifice, thereby permitting fluid flow through the radially arrayed through-holes and then out the top orifice. (Right) Under reverse flow conditions, the helical coil spring expands as the blocking disc forms a fluidic seal at the bottom orifice, which physically obstructs the flow of fluid through the element.*

1.4.1. Theoretical Simulations

To provide insight into the theoretical flow dynamics of the designed 3D microfluidic coil spring diode, we performed finite element analysis (FEA) fluid-structure interaction (FSI) simulations of the element (**Fig. 1.6; Movie 1.3**). FEA simulations were performed using the commercial software, COMSOL Multiphysics v.5.3a (COMSOL Inc., Sweden). Initially, 3D model of the microfluidic diode was created using SolidWorks (Dassault Systemes). The 3D CAD model was then imported into the COMSOL Multiphysics software. Then, FSI simulations were performed with the stokes flow physical model and quasi-static structural transient behavior. The structure material (IP-L 780) was modeled with material properties E = 1.75 GPa and ν = 0.49 [67]. The input pressure conditions were designed to ensure that the simulation terminates upon mesh intersection (*e.g.*, the surface of the sealing disc interacting with either the bottom orifice or the intermediary structure the source output channel) in order to avoid topological changes. IPA (ρ = 783 kg/m^3; η = 2.4 × 10^{-3} Pa·s) was modeled as the input fluid.

The simulation results revealed fundamental differences associated with each directional flow polarity (**Fig. 1.6a**). In particular, as the input pressure was incrementally increased in the forward flow direction, the magnitude of the flow rate also increased, with the caveat that these effects were non-linear due to the varying resistive effects corresponding to the decreasing distance between the sealing disc and the intermediary structure. After the sealing disc was immobilized, the flow rate increased linearly with increasing pressure. For the reverse flow case, the fluid flow rates through the element were similar to those of the forward flow case for lower pressures. As the reverse pressure continued to increase, however, the magnitude of fluid flow decreased until the sealing disc fully descended onto the bottom orifice and the fluid flow ceased (**Fig. 1.6; Movie 1.3**).

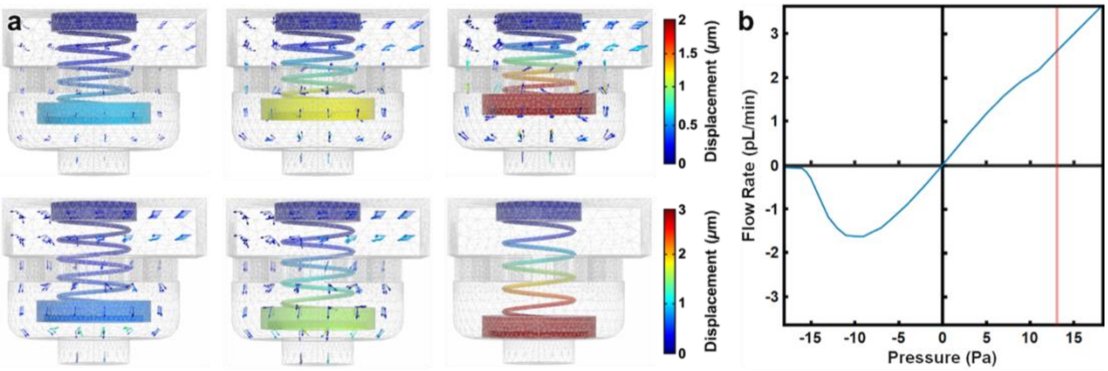

***Figure 1.6**: (**a**) Sequential COMSOL Multiphysics fluid-structure interaction (FSI) simulations of flow dynamics corresponding to forward flow (Top) and reverse flow (Bottom) (see also **Movie 1.3**). Arrows denote fluid velocity field vectors. (**b**) Quantified simulation results for the polarity-based flow dynamics of the 3D microfluidic coil spring diode. The dashed red line marks the pressure at which the sealing disc fully contacted the intermediary structure, physically blocking flow through the center orifice.*

To investigate the ideal functionalities of the microfluidic coil spring diode, we quantified the magnitude of the fluid flow with respect to input pressure for the theoretical FEA simulations (**Fig. 1.6b; Movie 1.3**). The simulation results revealed non-linearities in the flow behavior for both polarities. For pressures up to approximately 5 Pa applied in the forward direction, the flow rate appeared to increase linearly with the pressure. As the pressure continued to increase, the sealing disc approached the center orifice of the intermediary structure, which resulting in fluctuating increases in the hydraulic resistance, and in turn, impeded the flow of fluid through the element. In particular, we observed a relatively larger decrease in the rate of forward flow from approximately 9 Pa to 13 Pa, at which point the disc fully sealed to the intermediary structure (**Fig. 1.6b –** ***red line***).

For pressures applied above 13 Pa, the flow rate appeared to linearly increase with increasing pressure; however, the rate at which the flow increased with pressure – a function of the hydraulic resistance through the element – was slightly smaller than that observed from 0 Pa to 5 Pa. Although this behavior indicates that the hydraulic resistance through the element is slightly larger after the disc seals to the intermediary structure, the effect was limited to a nominal reduction in the overall magnitude of forward flow. For the reverse flow case, from 0 Pa to approximately -5 Pa, the flow behavior was essentially indistinguishable from that of the forward flow case for the same range of pressures. From -5 Pa to -10 Pa, however, the rate at which the reverse flow increased with increasing reverse pressure began to decrease, with a peak reverse flow at -10±1 Pa. Thereafter, the magnitude of reverse flow through the microfluidic element declined substantially as the sealing disc approached the bottom orifice, with full sealing interactions by -18 Pa (**Fig. 1.6b**)

1.4.2. Fabrication Results

We applied the aforementioned *is*DLW protocols to fabricate the 3D microfluidic diodes within sol-gel-coated PDMS-on-glass microchannels with semi-ovular cross-sectional profiles and approximately 25 μm height. Sequential CAM simulations and fabrication results are presented in **Fig. 1.7** (*see also* **Movie 1.4**). Preliminary flow rectification experiments revealed the effects on the expansion of the PDMS microchannels adjacent to the microfluidic diode (**Fig. 1.8a-c; Movie 1.5**). Due to the highly compliant nature of PDMS, increasing the input pressure resulted in an observable enlargement of the microchannel walls. For example, under an input pressure of 150 kPa in the forward flow direction (**Fig. 1.8b**), the microchannel walls on both sides of the diode showed significant expansion compared to their non-pressurized state (**Fig. 1.8a**). In contrast, for an input pressure of 150 kPa in the reverse direction, expansion of the microchannel walls was only observed upstream of the microfluidic diode, with no apparent downstream wall deformation (**Fig. 1.8c; Movie 1.5**).

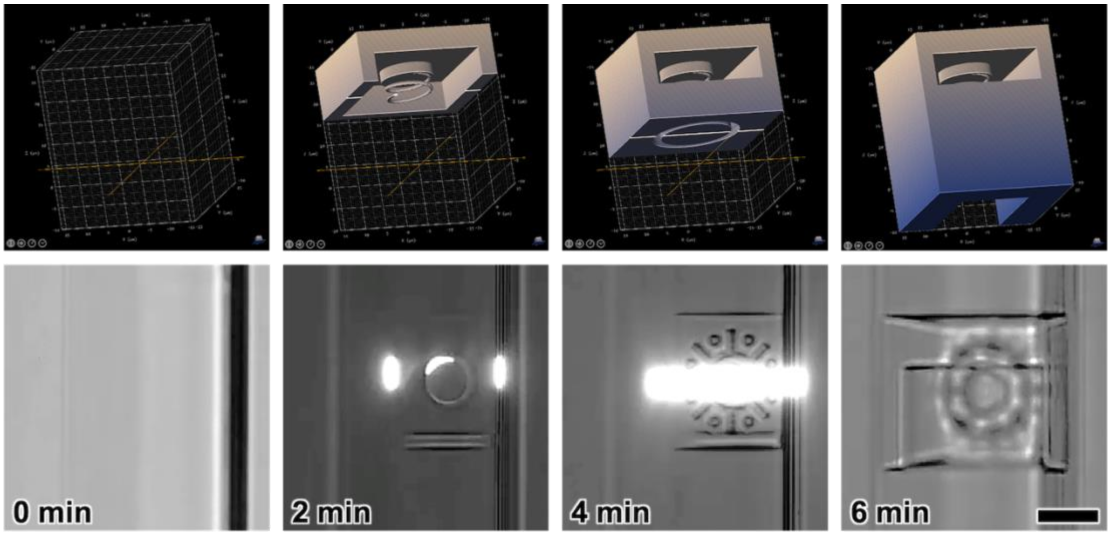

***Figure 1.7**: Sequential CAM simulations (Top) and corresponding isDLW fabrication results (Bottom) for printing a 3D microfluidic coil spring diode within a sol-gel-coated PDMS microchannel with a semi-ovular cross-sectional profile and height of ~25 μm (see also **Movie 1.4**). Scale bar = 10 μm.*

1.4.3. Microfluidic Testing Setup

For experimental testing of the microfluidic diode, all input parameters were controlled using scripts written in the Fluigent software, while flow rate measurements were collected from two flow units (connected to each end of the straight channel). For the half-wave rectification tests, three microfluidic diodes were tested by introducing a sinusoidal pressure input to the microchannel, with an amplitude of 150 kPa and time period of 60 s. For the steady-state flow behavior characterization, a total of 12 tests were performed using three different diodes. The pressure was first increased from 0 to 150 kPa in forward flow configuration with a 5 kPa step size and 10 s settling time– parameters set by the operational capabilities of the MFCS platform. Similarly, the procedure was repeated in the reverse flow configuration after a 30 s settling period. The data collected from both testing procedures were processed and plotted in MATLAB.

1.4.4. Flow Rectification of Microfluidic Diode

The ability for a microfluidic diode to serve as a half-wave fluidic rectifier is a critical metric of element functionality [66]. To test this capability, we introduced sinusoidal input pressures, which entailed repeatedly cycling the pressure from 150 kPa applied in the forward direction to 150 kPa applied in the reverse direction over a period of 60 seconds (**Fig. 1.8d and e**). The results revealed significant forward bias of the flow polarity, with the flow rate behavior closely matching the pressure changes for the forward direction, yet restricted flow rates despite increasing pressures in the reverse direction. For each change in the flow polarity from forward to reverse pressure as well as reverse to forward pressure, we observed initial spikes in the flow rate that quickly dissipated within approximately 2 seconds (**Fig. 1.8e**). We also found that the amplitude of the forward flow peaks appeared to wane slightly with time (**Fig. 1.8d**). An additional figure of merit for microfluidic diodes is the non-dimensional *Diodicity* (*Di*), which is calculated as:

$$Di = \frac{R_{Reverse}}{R_{forward}} \quad (1)$$

here, *R* is the hydrodynamic resistance associated with forward and reverse flow [68–71]. To characterize the *Di* performance of the 3D microfluidic coil spring diode, we further quantified the polarity-based flow behavior through non-oscillating experiments. These experiments provided insight into the steady-state flow rates associated with distinct forward and reverse pressures (**Fig. 1.8f**). The forward flow dynamics exhibited linear increases in the magnitude of fluid flow up to 22.8 ± 7.2 μL/min at 147.4 ± 2.5 kPa. This was in stark contrast to the reverse flow results, which revealed significant obstruction of fluid flow, with different flow behaviors at lower and higher pressures. Specifically, for pressures applied in the reverse direction of up to 67.4 ± 2.4 kPa, the average flow rate appeared to fluctuate between 0.61 ± 0.71 and 1.6 ± 1.3 μL/min. For reverse pressures from 77.3 ± 2.6 kPa to 147.4 ± 2.4 kPa, however, the average flow rate was consistently maintained below 0.64 ± 0.88 μL/min (**Fig. 1.8f**). These results correspond to an overall trend of improved *Di* performance at higher pressures, with a maximum *Di* of approximately 45.8 at the largest pressure magnitudes tested approaching 150 kPa.

The 3D microfluidic coil spring diode introduced here represents, to the best of our knowledge, the smallest fluidic diode and the smallest 3D printed mechano-fluidic circuit element reported in the literature. One caveat to this scale, however, is that fluidic operation is more susceptible to debris in the microchannel. Although we implemented filters to mitigate the effects of internal debris, the half-wave fluidic rectification results suggest that debris accumulation in the filters contributed to slight reductions in the maximum flow rates at the onset of fluidic testing (**Fig. 1.8d**). Specifically, flow rectification experiments for the microfluidic diode over 100 cycles revealed that such reductions were limited to the first 20 cycles as the overall flow behavior remained relatively constant thereafter (**Fig. S6**). The experimental results for half-wave flow rectification also revealed brief spikes in the flow rate corresponding to each reversal in the flow polarity (**Fig. 1.8d and e**).

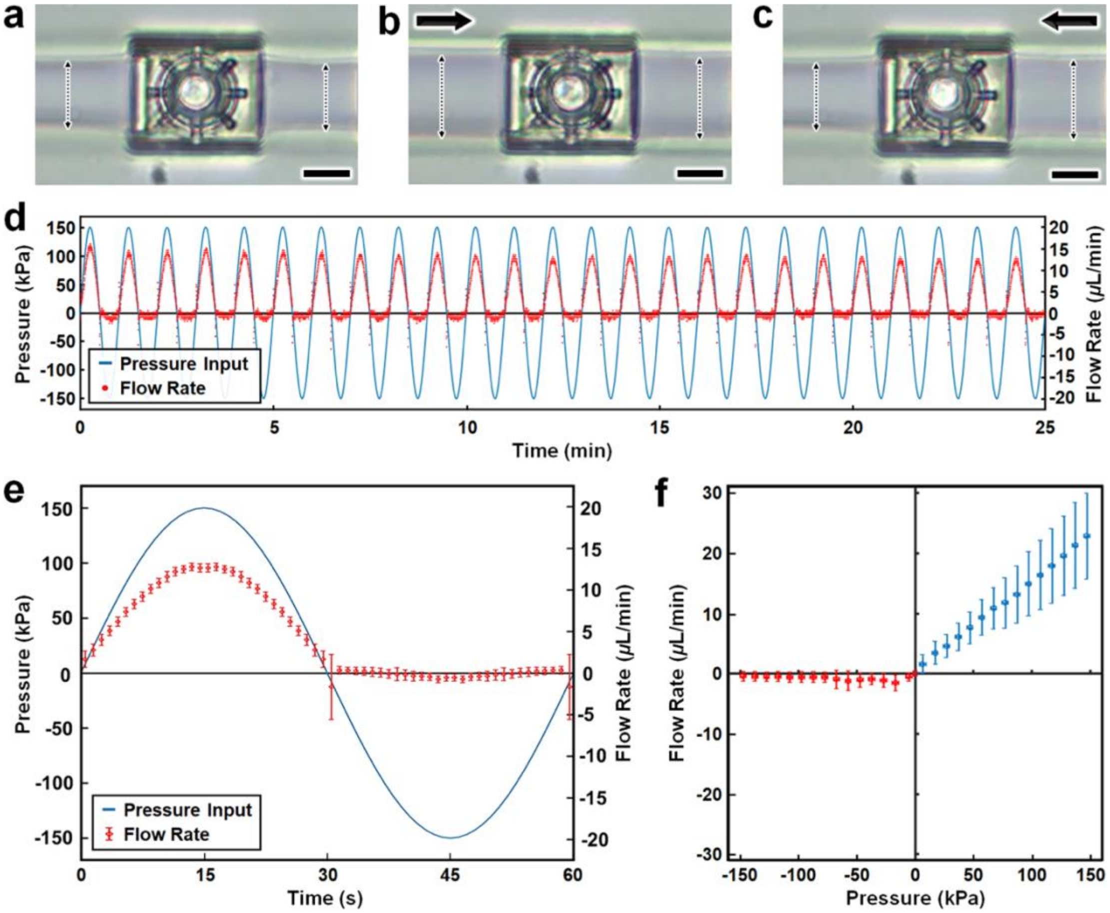

***Figure 1.8**: Experimental results for the isDLW-printed 3D microfluidic coil spring diode. (**a**–**c**) Micrographs of PDMS channel expansion adjacent to the microfluidic diode corresponding to applied pressures of: (**a**) 0 kPa (control), (**b**) 150 kPa in the forward direction, and (**c**) 150 kPa in the reverse direction (see also **Movie 1.5**). Arrows denote the direction of applied pressure; dotted double arrows mark the PDMS microchannel width; Scale bars = 10 μm. (**d,e**) Half-wave fluidic rectification results for (**d**) 25 minutes of testing, and (**e**) a single 60 second period averaged for three distinct tests. (**f**) Quantified results for directional fluid flow versus pressure. All error bars denote standard deviation; negative values for pressures and flow rates denote positive pressures and flow rates in the reverse direction.*

Two main factors could account for such behavior: (*i*) physical resistance to fluidic sealing due to a large coil spring stiffness, and (*ii*) fluid volume discharge due to the hydraulic capacitance of the PDMS channels. Based on the coil spring geometry and material properties, the coil spring stiffness is estimated to be on the order of 1 nN/μm– a stiffness that resulted in significant deformation of the spring at low pressures (**Movie 1.2**). Thus, it is more likely that the ability for the PDMS microchannels to operate as hydraulic capacitors [71,72] led to the aforementioned flow rate spikes. Under an applied pressure, the PDMS microchannels expand to store fluid volume; however, once the pressure is no longer applied, the PDMS microchannels contract to their initial state, releasing the previously stored fluid volume. Experimentation revealed expansion-contraction behaviors of the PDMS microchannels that are consistent with hydraulic capacitor functionalities (**Fig. 1.8a-c; Movie 1.5**). Nonetheless, the overall fluidic rectification functionalities of the *is*DLW-printed 3D microfluidic diode are unprecedented at this scale (**Fig. 1.8d-f**). Due to emerging applications in fields such as soft robotics and biofluidic processing that rely on the scaling of microfluidic circuitry, the 3D microfluidic diode in this study could serve as an important baseline for a new generation of microfluidic circuit elements that are constructed by means of *is*DLW.

Chapter 2: COP-based *is*DLW of "Normally Open" Microfluidic Transistors

2.1. Scope

In the previous chapter, we introduced a sol-gel coating-based strategy that can considerably improve structural adhesion of *is*DLW-printed structures in PDMS-on-glass microchannels. By conducting fluidic experiments on printed barrier structures, we demonstrated effective structure-to-channel fluidic sealing for input pressures up to 75 kPa (**Fig. 1.4**). A caveat to that approach, however, is that the sealing performance was limited to lower pressures, which restricts the use of this strategy for applications that require higher pressure inputs. Furthermore, incompatibility of PDMS with most of the organic solvents used in DLW (e.g. IPA, PGMEA, etc.) [42–44] restricts the use of these solvents in the development stage of the print and causes bulk degradation and swelling of the channel. One of the main consequences of this effect is increase in channel contamination due to the shedding of PDMS from the inlet ports into the channel. This issue can be solved partially by the introduction of filters into the channels, which is still prone to clogging and reduction of flowrate through the channel.

To overcome the aforementioned limitations associated with PDMS-on-glass systems while still benefiting from the accessibility of micromolding and bonding procedures. This chapter examines the use of COP as an alternative microchannel material for *is*DLW. COP is a thermoplastic material that exhibits properties that are advantageous for *is*DLW, including high optical transparency [73,74], resistance to polar organic solvents [75,76], effective micropattern replication [77–80] and bonding [81–83], and low gas permeability [78].

In this chapter we present a novel *is*DLW protocol that is based on COP-COP devices fabricated by hot embossing COP using DLW-printed molds with customizable geometries. We experimentally characterize key *is*DLW parameters (*e.g.*, laser power, microchannel shape and size) to elucidate the conditions under which microstructures of various heights can be manufactured effectively. We investigate the performance of COP-based *is*DLW-printed microstructures with hierarchical degrees of geometric and operational microfluidic complexity: (*i*) monolithic fluidic barriers that are designed to remain stationary while obstructing fluid flow (irrespective of input pressure) – an important measure of structure-to-channel sealing integrity; (*ii*) 3D interwoven microvessel-inspired tubular architectures, which while structurally immobile, are designed to permit fluid flow within their internal tortuous microfluidic pathways; and (*iii*) a 3D microfluidic bellowed *NO* transistor that can be dynamically actuated during operation to actively regulate the flow of fluid through the component. Establishing fundamental baselines with which to evaluate the utility of COP-based *is*DLW for a diversity of microfluidic studies and applications.

2.2. COP-based isDLW

2.2.1. Concept

The COP-based *is*DLW approach presented here includes five key steps: (*i*) master mold fabrication *via* DLW (**Fig. 2.1a and b**), (*ii*) COP channel replication (**Fig. 2.1c**

and d), (*iii*) inlet/outlet port integration (**Fig. 2.1e**), (iv) COP-COP bonding (**Fig. 2.1f-h**), and (v) *is*DLW of microstructures directly inside of the COP-COP microchannels (**Fig. 2.1i-k**). Several groups have demonstrated the use of DLW for micromold fabrication, particularly for cases that demand non-planar channel geometries [41,53–56]. Here, DLW is utilized in the dip-in laser lithography (DiLL) configuration to manufacture microchannels with varying architectures (**Fig. 2.1a**). After completion of the mold printing process and development (**Fig. 2.1b**), established COP hot embossing methods [84,85] are employed to replicate the microchannel structures (**Fig. 2.1c and d**). Thereafter, through holes for inlet and outlet ports are drilled at desired locations in the micromolded COP (**Fig. 2.1e**).

A thin, flat COP sheet serves as the base of the COP microchannels. To achieve vapor-phase solvent bonding, the COP base is first exposed to cyclohexane vapor (**Fig. 2.1f**), which results in a tacky surface. This surface is then brought into contact with the micromolded COP to achieve fully enclosed COP-COP microchannels (**Fig. 2.1g and h**). For the *is*DLW step, a liquid-phase photocurable material is infused into the COP-COP channel (**Fig. 2.1i**). DLW is then utilized in the oil-immersion mode for microstructure printing. In this configuration, the laser passes from the objective lens through an immersion oil, then the thin COP base, and finally, through the uncured photomaterial to begin the photopolymerization process only at the focal point (**Fig. 2.1j**). To avoid disruptions of the laser due to interactions with previously cured photomaterial, microstructures are printed in a “ceiling-to-floor”, point-by-point, layer-by-layer methodology. Once the DLW process is complete (**Fig. 2.1k**), developing agents are infused into the channel to remove any remaining uncured photomaterial.

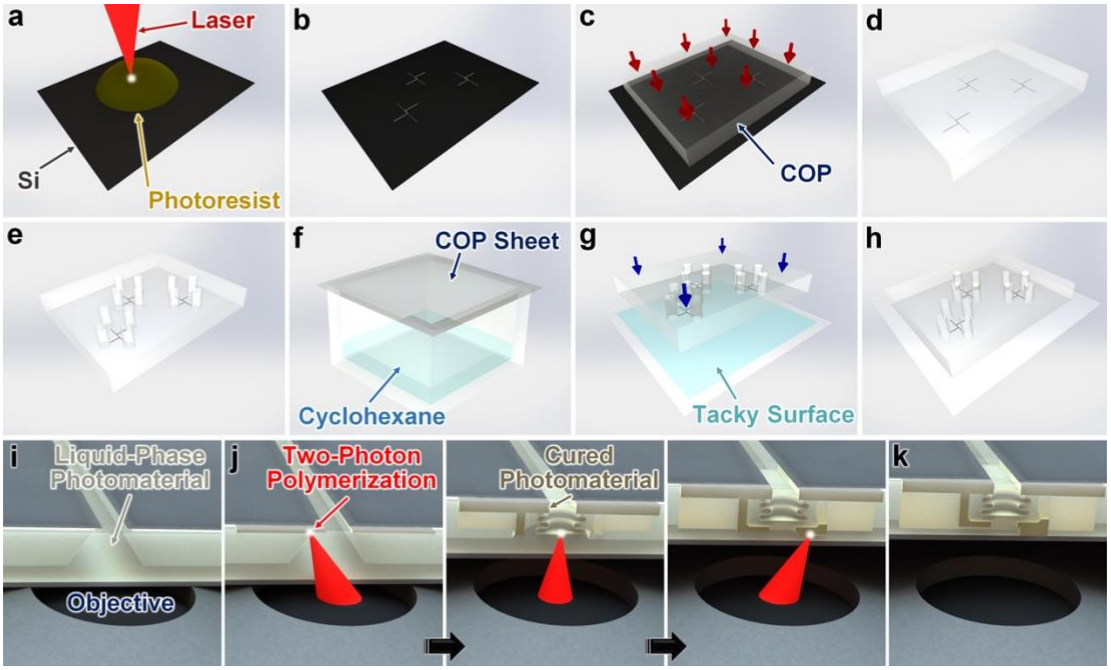

***Figure 2.1**: Conceptual illustrations of the COP-based isDLW) strategy. (**a**) DLW of microchannel mold structures. (**b**) Printed negative master mold. (**c**) Hot embossing-based COP replication of the microchannel molds. (**d**) Micromolded COP. (**e**) Integration of inlet and outlet ports. (**f**) Exposure of vapor-phase cyclohexane to a thin COP sheet. (**g**) Bonding of the micromolded COP to the thin COP sheet. (**h**) Enclosed COP-COP microdevice. (**i–k**) IsDLW fabrication. (**i**) Infusion of a liquid-phase photomaterial into the COP-COP microchannels. (**j**) "Ceiling-to-floor", point-by-point, layer-by-layer photopolymerization via a focused femtosecond IR laser. (**k**) Printed 3D microfluidic bellow-type transistor (comprised of cured photomaterial) that is fully sealed to the luminal surface of the COP-COP microchannel at designed locations.*

2.2.2. Negative Master Mold Fabrication via DLW

All microchannel negative master mold patterns were designed using the commercial CAD software, SolidWorks (Dassault Systemes, France). The CAD files were converted to the STL file format, and then imported into the CAM software, DeScribe (Nanoscribe GmbH, Germany) to generate the code for the laser writing path. For all molds, the layer height and hatching parameters were 1 μm and 500 nm, respectively. Si substrates (25 mm × 25 mm) were rinsed successively with acetone and IPA, then dried with inert N_2 gas, and lastly, placed on a hot plate set at 100 °C for 15 min. The negative-tone photoresist, IP-S (Nanoscribe), was deposited onto the Si substrate, which was then loaded into the Nanoscribe Photonic Professional GT DLW system. The DLW printer settings included the use of a 25× objective lens and the DiLL mode configuration. Due to the large print area of the channel mold structures (approximately 3 mm × 3 mm), a stitching-based print methodology was utilized by which the master mold was printed in 280 μm × 280 μm areas that connect together (*e.g.*, **Fig. 2.2 and Movie 2.1**).

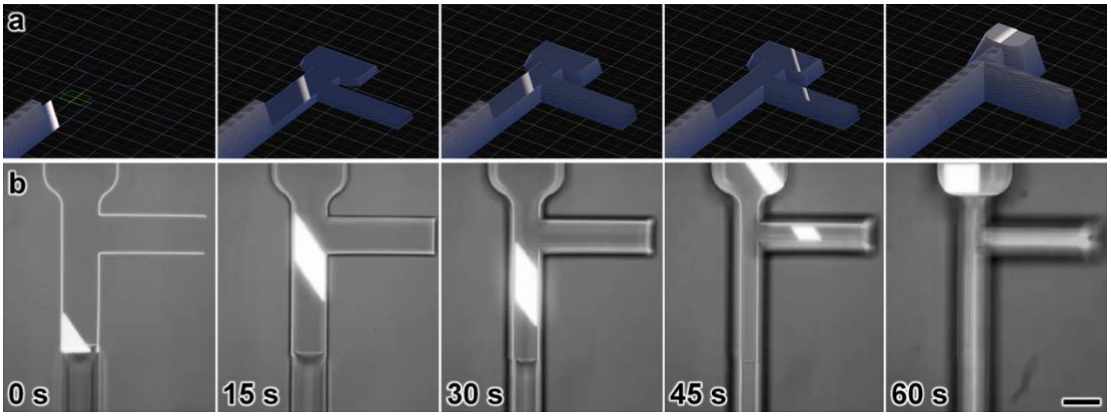

Figure 2.2*: Fabrication of microchannel negative master molds via "stitching"-based DLW. (****a****) Sequential CAM simulations of printing a new 280 µm ⇸ 280 µm area of the mold that is connected to a previously fabricated part of the mold. (****b****) Corresponding sequential brightfield micrographs of results for the DLW fabrication process. Scale Bar = 100 µm (see also* ***Movie 2.1****).*

For the fluidic barrier structure testing, a total of nine microchannel designs were printed, corresponding to three distinct cross-sectional profiles – each at heights of 10 μm, 50 μm, and 100 μm: (i) rectangular (to mimic channels generated *via* conventional, monolithic microfabrication processes) [49] (**Fig. 2.3a**), (ii) trapezoidal (with 20° outward tapering sidewalls) (**Fig. 2.3b**), and (iii) semi-elliptical (**Fig. 2.3c**). All of the microchannels were designed with an aspect ratio of 1. The molds for the microvessel-inspired structures were designed with a circular region (40 μm in height; 120 μm in diameter) intersecting with six identical microfluidic channels (30 μm in height; 50 μm in width; 25°-tapered trapezoidal cross sections). For the *NO* microfluidic transistors, the molds were designed with two intersecting channels (30 μm in height; 50 μm in width; 25°-tapered trapezoidal cross sections). After completion of the DLW-printing process, the substrates were developed by successive rinses in PGMEA for 30 min and IPA for 2 min to remove any remaining uncured photoresist.

2.2.3. COP-COP Microdevice Fabrication

A 3 mm-thick COP sheet (ZEONOR 1060R, Zeon Corp., Japan) was rinsed with IPA, dried with inert N_2 gas, and then brought into contact with the fabricated negative master mold. The COP sheet was hot embossed for 3 min at 120 °C to facilitate the replication of the microchannel designs from the mold (*e.g.*, **Fig. 2.3d-f**). Through holes for inlet and outlet ports were drilled in the molded COP at desired locations. The surface of a 100 μm-thick COP film (microfluidic ChipShop GmbH, Germany) was exposed to vapor-phase cyclohexane at 30 °C for 2 min. Immediately after the vapor-exposure process, the 100 μm-thick COP film and the micromolded 3 mm-thick COP sheet were brought into contact for 1 min at room temperature (20-25 °C) to facilitate permanent COP-COP bonding, resulting in a final device with enclosed microchannels (**Fig. 2.5**). A key attribute of the 100 μm-thick COP film is that its refractive index (1.53) [86] closely matches that of both borosilicate glass substrates (1.52) and the immersion oil (1.52) that are conventionally used for oil-immersion-mode DLW.

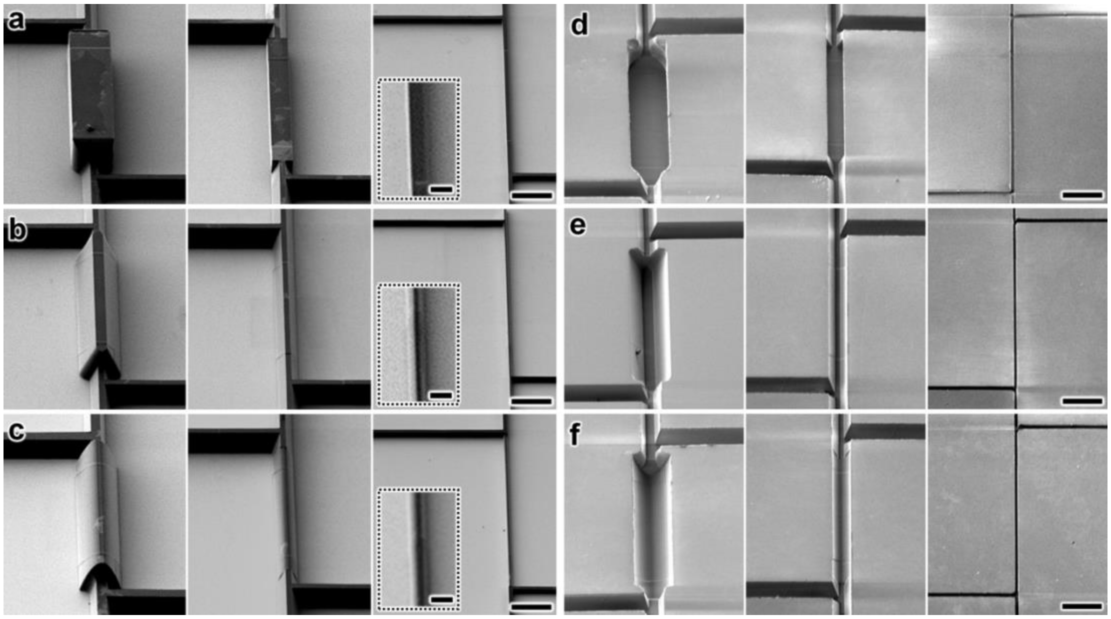

*Figure 2.3: Fabrication results for (**a-c**) DLW-printed negative master molds and (**d-f**) hot embossing-replicated COP corresponding to channel heights of: (Left) 100 µm, (middle) 50 µm, and (right) 10 µm. (**a**) Rectangular channel molds. (**b**) Trapezoidal (20) channel molds. (**c**) Semi-ovular channel molds. (**d**) Replicated rectangular channels. (**e**) Replicated trapezoidal channels. (**f**) Replicated semi-ovular channels. Scale bars = 100 µm; Inset scale bars = 10 µm*

2.2.4. COP Microchannel Replication using PDMS Negative Master Molds

In this work, COP microchannels were replicated using Si substrates with DLW-printed patterns as the negative master mold *via* hot embossing protocols (**Fig. 2.1a-c**). One caveat to this approach, however, is that the high temperatures and pressures applied during hot embossing processes can limit the overall lifespan of the negative master mold. Thus, for cases that demand high numbers of COP replication steps for a single mold design, we present a secondary approach in which an additional negative master mold is fabricated using the silicone elastomer, PDMS.

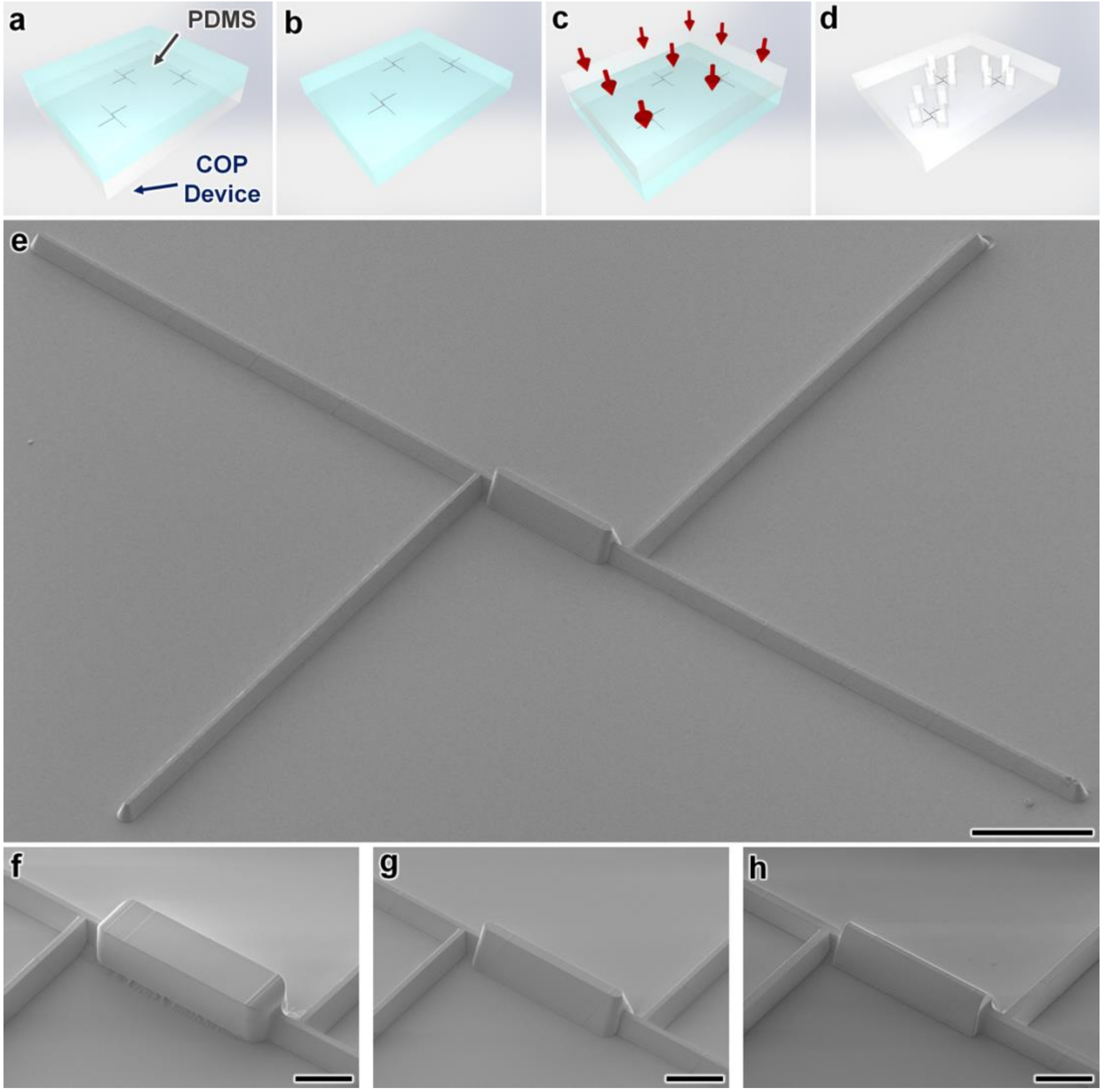

*Figure 2.4: COP replication using PDMS negative master molds. (**a-d**) Conceptual illustrations. (**a**) Replication of PDMS using a micromolded COP sheet. (**b**) Fabricated PDMS negative master mold. (**c**) Hot embossing-based replication of micromolded COP using PDMS mold. (**d**) Micromolded COP. (**e-h**) Micrographs of fabrication results for PDMS molds (100 μm in height) with various channel profiles. (**e**) Expanded view of the PDMS mold for the trapezoidal cross-sectional profile. Scale bar = 300 μm. Close-up views of results corresponding to the (**f**) rectangular, (**g**) trapezoidal, and (**h**) semi-elliptical cross-sectional profiles. Scale bars = 100 μm.*

The initial steps of the protocol are consistent with those depicted in **Figure 2.1a-d**, with a 3-mm-thick COP sheet being replicated from a DLW-patterned Si substrate. Once the micromolded COP sheet has been produced, however, it is rinsed with IPA and dried with inert N2 gas. A 5:1 (base:curing agent) mixture of PDMS (Sylgard 184, Dow Corning, Corning, NY) is poured over the COP sheet, degassed in vacuum for 30 min, and then placed on a hot plate set at 60 C for 2 hours (**Fig. 2.4a**). After thermal curing, the PDMS is peeled off of the COP (**Fig. 2.4b**). Thereafter, the molded PDMS can serve as a negative master for additional COP replication steps. Specifically, the PDMS replica can be used in place of the original DLW-patterned Si negative master mold to facilitate PDMS-based hot embossing of 3-mm-thick COP sheets at 120 C for 5 min (**Fig. 2.4c and d**). Fabrication results for PDMS negative master molds corresponding to various microchannel profiles are presented in **Figure 2.4e-h**. The benefit of this approach is that the overall lifespan of the original DLW-based mold can be extended significantly, thereby limiting the time and labor associated with DLW of multiple negative master molds.

2.2.5. Microstructure Fabrication via isDLW

The 3D models for the fluidic barrier, microvessel, and microfluidic transistor microstructures were all generated using SolidWorks (Dassault Systemes) and imported into DeScribe (Nanoscribe) for writing-path generation. The negative-tone photoresist, IP-L 780 (Nanoscribe), was loaded into the COP-COP microchannels. The microchip was then fixed on a holder (with immersion oil placed on the underside of the 100 μm-thick COP film) and loaded into the Nanoscribe Photonic Professional GT DLW system. The DLW printer settings included the use of a 63x objective lens in the oil-immersion mode configuration. All structures were printed *via* a “ceiling-to-floor”, point-by-point, layer-by-layer writing-path routine. After completion of the DLW process, remaining uncured photoresist was cleared from the devices by infusing the organic solvent, PGMEA, for 10 min, IPA for 3 min, and lastly, pressurized air into the microchannels. To facilitate this development process for the circular center region of the microvessel-inspired tubular structures, two intervening microchannels (*i.e.*, one input and one output) for developer infusion and material removal were integrated into the design

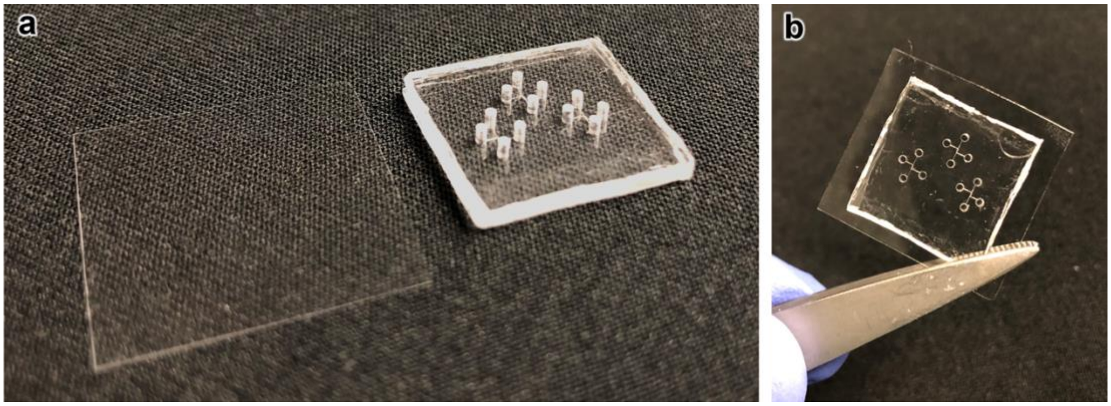

***Figure 2.5**: Fabrication results for the COP-COP microfluidic device. (**a**) Image of COP components prior to the bonding process. (Left) A 100-µm-thick COP sheet. (Right) Micromolded COP with access ports at inlet and outlet locations. (**b**) Image of a COP-COP microfluidic device following the vapor-phase solvent bonding process.*

2.2.6. Optical Characterization

All scanning electron microscopy (SEM) characterizations were carried out using the Hitachi SU-70 Schottky field emission gun SEM (Hitachi, Japan). To facilitate SEM imaging of *is*DLW-fabricated microstructures, the COP-COP bonding and *is*DLW printing protocols were modified to enable detachment of the 100 μm-thick COP base. Specifically, the cyclohexane exposure time was reduced to achieve a relatively weak bond between the 100 μm-thick COP film and the micromolded COP sheet. In addition, printed structures were designed with a slightly smaller height, such that the *is*DLW printing process would terminate approximately 2 μm from the thin COP film (*i.e.*, to prevent the structures from sealing to the base). In combination, these modifications allowed for the 100 μm-thick COP film to be manually removed following the *is*DLW process.

2.2.7. Microfluidic Experimentation

For all fluidic experiments, MAESFLO software (Fluigent, France) was utilized to interface with the Fluigent Microfluidic Control System (MFCS) and flow rate platform, which supported simultaneous input pressure regulation and pressure/flow rate data registration. Fluids were introduced into the COP microdevices using FEP tubing (Cole-Parmer, Vernon Hills, IL) and stainless-steel catheter couplers (20 ga., Instech, Plymouth Meeting, PA). For experiments in which specific ports required sealing, stainless steel catheter plugs (Instech) were inserted into the COP through holes. Data from all completed experiments were processed using MATLAB software (MathWorks, Natick, MA) to calculate the mean and standard deviation (S.D.) of the flow rate data with respect to specified input pressure increments corresponding to the fluidic barriers and microfluidic transistor experiments. For testing with fluorescently labelled fluids, methylene blue and rhodamine B dyes (MilliporeSigma, St. Louis, MO) were infused into the microdevices *via* distinct inlet ports. Microscopic imaging was performed using an inverted microscope (Motic AE31, Motic, Canada) connected to a charge-coupled device (CCD) camera (Moticam Pro 285B, Motic), while fluorescence imaging was performed using an inverted fluorescence microscope (Axio Observer.Z1, Zeiss, Germany) connected to a CCD camera (Axiocam 503 Mono, Zeiss).

2.3. Fluidic Barrier Structures

2.3.1. Printing Parameters of COP-based isDLW

An important criteria for *is*DLW is that the base material through which the laser passes must have sufficient optical transparency such that photopolymerization phenomena are not disrupted, particularly for microstructures printed at taller heights (*i.e.*, farther away from the objective lens). Although the “ceiling-to-floor” printing strategy employed in this work limits laser aberrations caused by previously cured microstructures in the laser path, remaining factors – namely, the optical properties of the uncured photoresist and the thin COP base – could still disrupt DLW-based photopolymerization events. Experiments in which the laser power was held constant during the *is*DLW fabrication process revealed malformed microstructures for which components at taller heights did not appear to cure effectively (*e.g.*, **Fig. 2.6**). To overcome such issues, two key parameters can be dynamically adjusted: (*i*) increasing the laser power with increasing height, or (*ii*) decreasing the laser scanning speed with increasing height. To maintain a consistent overall print time, it is preferable to first set the scanning speed at a constant magnitude (10 mm s^{-1} in this case), and then vary the laser power accordingly. A challenge in determining the appropriate laser power for a given height is that the exposure energy must be large enough to effectively initiate photopolymerization reactions, yet not too large such that photomaterial burning failures (*e.g.*, disruptive microbubble generation) occur.

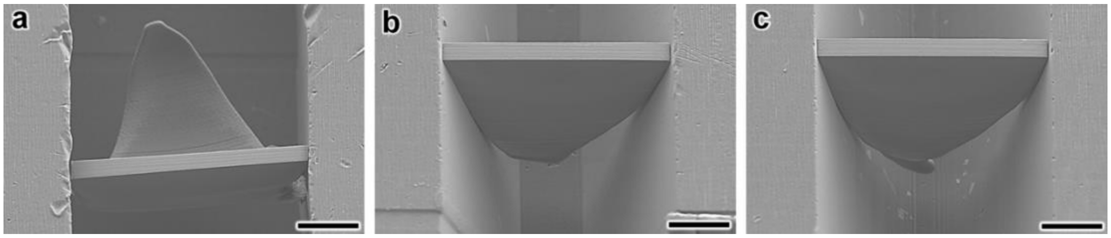

Figure 2.6*: Micrographs of fabrication results for isDLW of 10-µm-thick fluidic barrier structures in 100-µm-tall microchannels of various profiles (aspect ratio = 1) corresponding to a constant laser power (20 mW) and laser scanning speed (10 mm s1). (****a****) Rectangular cross-sectional profile. (****b****) Trapezoidal (20) cross-sectional profile. (****c****) Semi-elliptical cross-sectional profile. Scale bars = 20 µm.*

We conducted fabrication experiments at varying heights and laser powers, and then performed optical characterizations of the results to establish an optimal parameter space for COP-based *is*DLW. From these results, the below formula was empirically conceived to describe the relationship between the laser power and the channel height:

$$P = 16.9 \times e^{(9.1\times10^{-3})H} \tag{2}$$

where P is the laser power in mW and H is the writing height in μm measured as the distance from the COP base surface of the microchannel. It is important to note that these results are based on a specific set of materials (*e.g.*, 100 μm-thick COP substrate, IP-L 780 photoresist) and DLW printing parameters (*e.g.*, 300 nm layer height, 200 nm hatching distance, 10 mm s^{-1} scanning speed), and that any changes to such conditions may alter the observed laser power-height correlation. Nonetheless, by using this data to vary the laser power with printing height (using 10 μm intervals), we observed that microstructures could be successfully fabricated in COP-COP channels with heights ranging from 10 μm up to 100 μm (*e.g.*, **Fig. 2.7** and **Movie 2.2**).

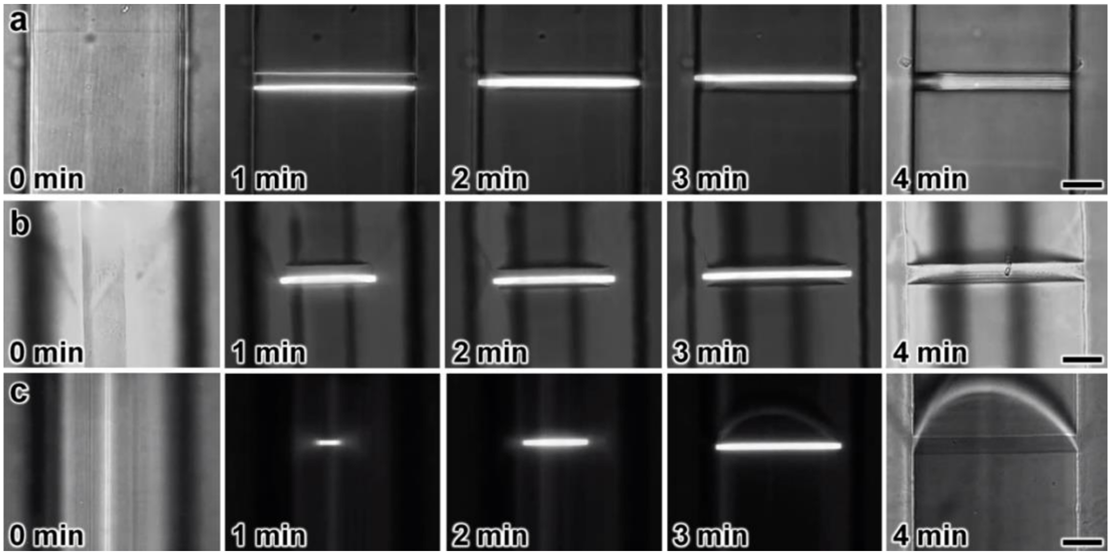

Figure 2.7*: Sequential micrographs of isDLW-printing of 10-µm-thick fluidic barrier structures inside 100-µm-tall channels by varying the laser power with height. (****a****) Rectangular cross-sectional profile. (****b****) Trapezoidal cross-sectional profile. (****c****) Semi-elliptical cross-sectional profile. Scale bars = 25 µm (see also* ***Movie 2.2****).*

Both the height and the shape of the microchannel cross-sectional profile – in particular, the degree of sidewall tapering – can significantly affect the efficacy of *is*DLW with respect to structure-to-channel sealing integrity. While we and other groups, [42,43] have previously hypothesized that sidewalls of microchannel profiles that lack significant outward tapering induce a "shadowing" effect that disrupts the laser path (*i.e.*, preventing *is*DLW in proximity to the sidewalls), the inability to remove the channel base following *is*DLW prevented confirmation of such phenomena. To investigate the potential for shadowing events to contribute to *is*DLW structure-to-channel sealing failures, here we utilized a weak COP-COP bonding approach to enable facile removal of the 100 μm-thick COP film following the *is*DLW printing process, thereby allowing for optical characterization of the *in situ* fabrication results.

For negative master mold fabrication, conventional photolithography-based methods are considerably faster than the point-by-point, layer-by-layer DLW approach utilized in this work. The caveat to the use of such microfabrication processes, however, is that the resulting microchannels typically exhibit relatively straight sidewalls. To explore the applicability of monolithic microfabrication protocols for *is*DLW, we fabricated COP-COP microdevices with rectangular channel cross sections at varying heights, and then printed 10 μm-thick microstructures designed to fully adhere along the top and sidewall surfaces of the microchannel (**Fig. 2.8b**). The fabrication results revealed that for 100 μm-tall channels, a significant portion of the microstructure did not appear to effectively photopolymerize in the regions adjacent to the sidewalls (**Fig. 2.8b – left**), despite the laser scanning in these locations (**Fig. 2.7** and **Movie 2.2a**). Although not as drastic, similar photocuring failures in proximity to the sidewalls at taller heights also occurred for cases with 50 μm-tall channels (**Fig. 2.8b – middle**). In contrast, for the 10 μm-tall rectangular microchannels, we did not observe any such fabrication issues (**Fig. 2.8b – right**). These results suggest that conventional microfabrication protocols for negative master mold manufacturing should only be utilized in cases of *is*DLW corresponding to microchannels with small heights (*e.g.*, 10 μm).

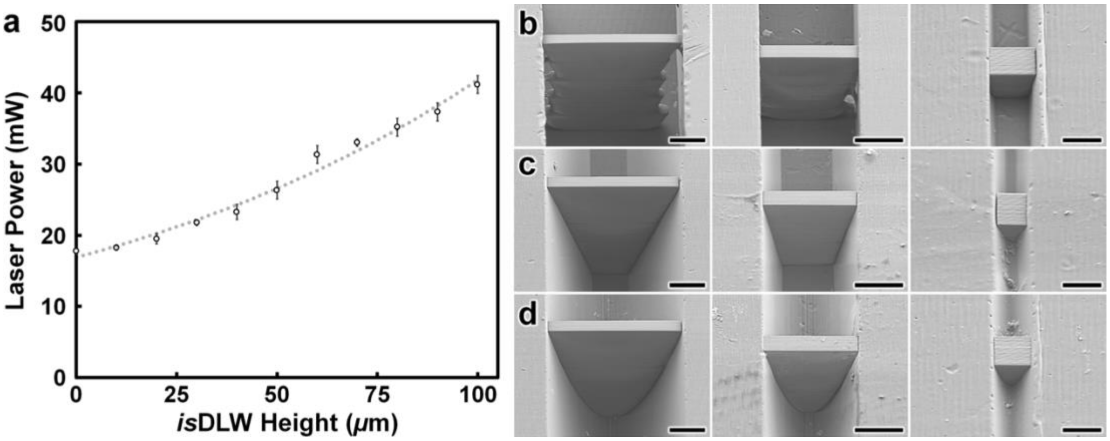

*Figure 2.8: IsDLW fabrication results for fluidic barrier microstructures. (**a**) Average laser power associated with successful isDLW prints and distinct heights (while maintaining a constant laser scanning speed). Dotted line represents eqn. 2; error bars = S.D. for n = 3 experiments. (**b–d**) SEM micrographs of fluidic barrier structures printed in COP–COP channels with (**b**) rectangular, (**c**) trapezoidal, and (**d**) semi-elliptical profiles corresponding to channel heights of: (left) 100 μm, (middle) 50 μm, and (right) 10 μm. Scale bars = (left, middle) 25 μm; (right) 10 μm.*

In addition to the rectangular channel profiles, we also investigated COP-COP microchannels of varying heights with trapezoidal (20°-tapered) and semi-elliptical cross sections (**Fig. 2.8c and d**). Unlike the rectangular channel results, we did not observe any height-based disparities in microstructure polymerization adjacent to the sidewalls. Rather, for both the trapezoidal and semi-elliptical cases, the *is*DLW results revealed undisrupted microstructure prints along the entire top and sidewall surfaces of the microchannels for every height examined (**Fig. 2.8c and d**). In combination, these fabrication results suggest that for tall microchannels (*e.g.*, ≥ 50 μm), conventional microfabrication protocols for master mold construction are ill suited for *is*DLW processes in which microstructures are printed in proximity to the channel sidewalls. For such cases, alternative methods of negative master mold fabrication that yield microchannels with effectively tapered sidewalls (*e.g.*, *via* DLW) should be utilized instead.

2.3.2. Fluidic Seal Testing

A critical metric of performance for *is*DLW strategies is the fluidic sealing integrity, which is related to the degree of structure-to-channel adhesion along the entire luminal surface of the microchannel. To quantify the sealing behavior for COP-based *is*DLW, we performed microfluidic burst-pressure experiments in which a ramping input pressure was applied on one side of an *is*DLW-printed barrier structure (with a plug in the other port on the same side), while both outlets on the opposite side of the barrier remained open (**Fig. 2.9a and b**). While gradually increasing the input pressure at a rate of 2 kPa s^{-1}, we optically monitored the 10 μm-thick barriers to determine if the dye-colored fluid remained on one side of the structure (*e.g.*, **Fig. 2.9c**) or if fluid leaked past the structure at a particular pressure magnitude. In addition, we also recorded both the input pressure and fluid flow rates during experimentation to measure any degree of fluid leakage.

Experiments with barrier microstructures printed inside COP-COP microchannels with rectangular cross sections revealed a significant role of channel height in the fluidic sealing performance (**Fig. 2.9d**). Unlike typical burst-pressure tests in which fluid flow is blocked up until a critical pressure at which point the flow rate instantaneously increases dramatically, the data from experiments with the two larger rectangular microchannels did not exhibit such fluidic events. Specifically, from the onset of experimentation for the 50 μm and 100 μm cases, we observed a linear relationship between the applied input pressure and the rate of fluid flow leaking past the barrier structure (**Fig. 2.9d**). This flow behavior suggests that the barriers lacked structure-to-channel sealing prior to experimentation, which is consistent with the results of the malformed barrier microstructures immediately after *is*DLW fabrication (**Fig. 2.8b – left and middle**). For the 10 μm case, however, we did not observe fluidic leakage past the barrier for input pressures up to approximately 500 kPa – the limit of the pressure regulator equipment, and thus, the largest pressures examined (**Fig. 2.9d**). This sealing efficacy is also corroborated by the fabrication results (**Fig. 2.8b – right**).

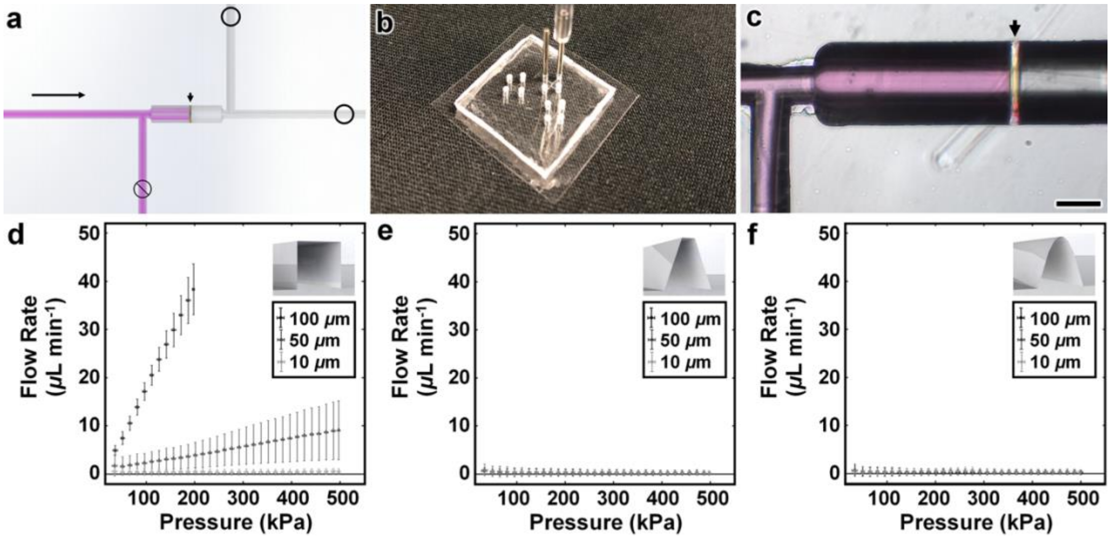

***Figure 2.9**: Microfluidic burst-pressure experimental results for isDLW-printed barrier structures. (**a**) Conceptual illustration of the experimental setup. Long arrow denotes the direction of input pressure; short arrow marks the location of the fluidic barrier structure in the channel. (**b**) Image of a device prepared for experimentation. (**c**) Micrograph of fluidic sealing under an applied input pressure of 500 kPa. Short arrow marks the location of the fluidic barrier structure in a 100 μm-tall trapezoidal channel. Scale bar = 50 μm. (**d–f**) Quantified experimental results corresponding to channels with varying heights and (**d**) rectangular, (**e**) trapezoidal, and (**f**) semi-elliptical profiles. Error bars = S.D. for n = 9 experiments per channel height and profile.*

To investigate the structure-to-channel sealing integrity associated with COP-COP microchannels in relation to channel geometry, we *is*DLW-printed fluidic barrier microstructures in channels with trapezoidal (20°) and semi-elliptical (aspect ratio = 1) cross-sectional profiles of varying heights. In contrast to the rectangular cases, the burst-pressure experiments with trapezoidal and semi-elliptical COP-COP channels did not reveal any such differences in sealing performance as a function of microchannel height (**Fig. 2.9d–f**). Notably, for the pressure ranges investigated (*i.e.*, ≤ 500 kPa), we did not observe any instances of fluidic barrier rupture for the 10 μm, 50 μm, and 100 μm cases corresponding to both the trapezoidal and semi-elliptical microchannel profiles (**Fig. 2.9e and f**). With respect to comparable PDMS-based *is*DLW results from previous chapter (**Fig 1.4**), the burst-pressure results – particularly for the 50 μm and 100 μm channels – represent an order of magnitude improvement in fluidic sealing performance.

Although a number of factors may have contributed to the significant enhancement in fluidic sealing integrity associated with *is*DLW in COP-COP microchannels *versus* PDMS-based systems, one key difference is the mechanical stiffness of COP compared to PDMS. Due to the relatively low elasticity of PDMS, inputting pressures on the order of 10–100 kPa results in visible outward expansion of microfluidic channels. As the microchannels expand, *is*DLW-printed barrier microstructures would be subjected to additional axial loading along the PDMS channel-to-structure interface. Microchannels comprised of COP – which has a Young's modulus that is approximately three orders of magnitude larger than that of PDMS – do not exhibit such deformations, including at pressure ranges up to 500 kPa. The lack of channel expansion for COP-COP systems restricts the overall mechanical loading on an *is*DLW-printed fluidic barrier structure to forces deriving solely from the pressure drop across the barrier.

2.4. Interwoven Bioinspired Microvessels

Although the microfluidic barrier structures provide a model system with which to interrogate structure-to-channel sealing behavior, we anticipate that COP-based *is*DLW is better suited for microfluidic applications that rely on architectures with greater extents of geometric complexity. To explore the potential use of COP-based *is*DLW for such scenarios, we designed a microfluidic system comprising two interwoven microvessel-inspired components – each with an inner diameter of 8 μm and a wall thickness of 2 μm – and examined the manufacturability of the tubular, tortuous 3D microstructures within COP microchannels (**Fig. 2.10a and b**) as well as their ability to isolate distinct fluorescently labelled microfluidic flow streams (**Fig. 2.10c**).

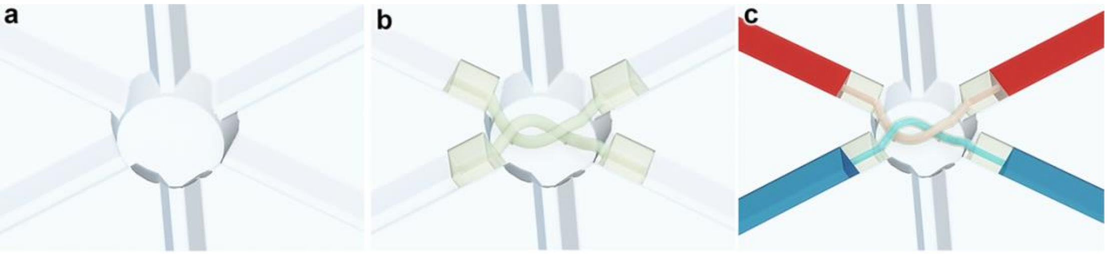

Figure 2.10*: Conceptual illustrations of the: (****a****) empty COP-COP microchannel, (****b****) isDLW-printed microvessel structures, and (****c****) independent loading of distinct fluorescently labelled fluids.*

2.4.1. Fabrication Results

CAM simulations and corresponding printing results for the "ceiling-to-floor", point-by-point, layer-by-layer microvessel *is*DLW fabrication process (within COP-COP microchannels) are presented in **Fig. 2.11a and b**, respectively (see also **Movie 2.3**). To prevent disruptions to the laser path caused by previously photocured structures, both microvessel-inspired structures were manufactured simultaneously. SEM micrographs of the fabrication results revealed effective production of the intricate 3D architectures, including the 8 μm-diameter microcurvature of the luminal surface of the vessel structure and the 2 μm-thick microvessel walls (**Fig. 2.11c and d**).

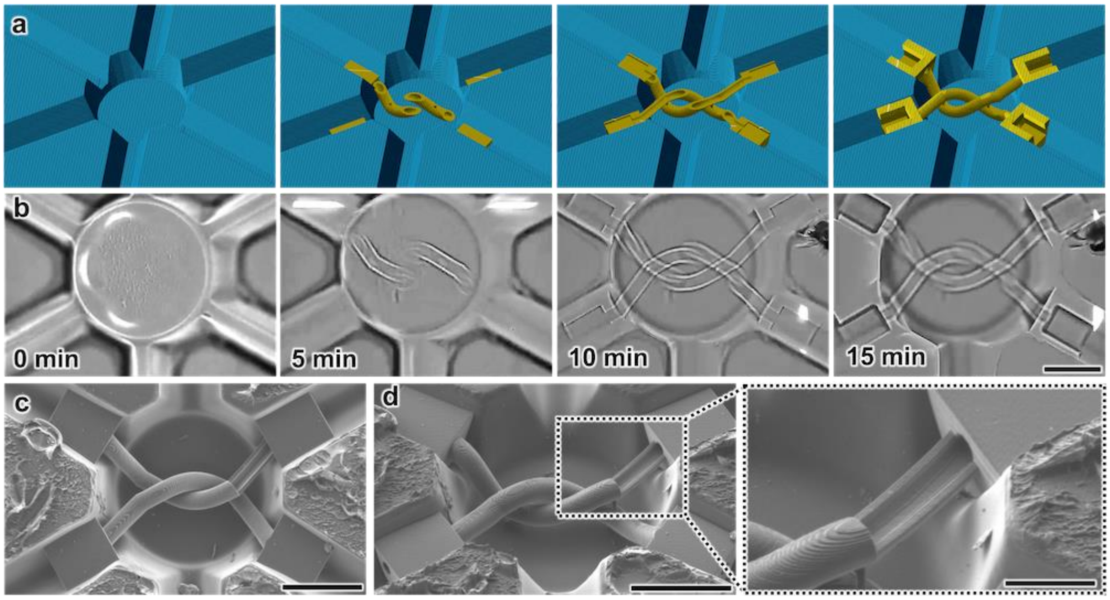

***Figure 2.11**: (**a**,**b**) Sequential images of (**a**) CAM simulations, and (**b**) corresponding fabrication results for the isDLW printing process (see also **Movie 2.3**). Scale bar = 50 µm. (**c**,**d**) SEM micrographs of fabrication results for isDLW-printed microvessel structures designed with one unenclosed tubular region. (**c**) Top view. (**d**) Tilted orientation with expanded view of the unenclosed region. Scale bars = 50 µm; (expanded view) 20 µm.*

2.4.2. Microfluidic Testing

To evaluate the microfluidic integrity of the fully enclosed microvessel-inspired structures, we configured the device such that: (*i*) one microchannel with a microvessel interface was connected to an input with a rhodamine B-dyed fluid, (*ii*) one microchannel interfacing with the other microvessel structure was connected to a methylene blue-dyed fluid input, and (*iii*) the four additional access ports – including those corresponding to the two intervening microchannels not directly connected to any microvessel structures (whose function is to support uncured photoresist removal) – remained open (**Fig. 2.12a**). We then perfused both the rhodamine B-dyed fluid (**Fig.**

2.12b) and the methylene blue-dyed fluid independently through their respective microvessel structures (**Fig. 2.12c**; **Movie 2.4**). Fluorescence micrographs of the microfluidic system confirmed that the flow streams were uncompromised (*i.e.*, leakage/contamination between the discrete microvessels or the intervening microchannels did not occur), with distinct fluorescence signatures corresponding to each microvessel structure (**Fig. 2.12d-f**).

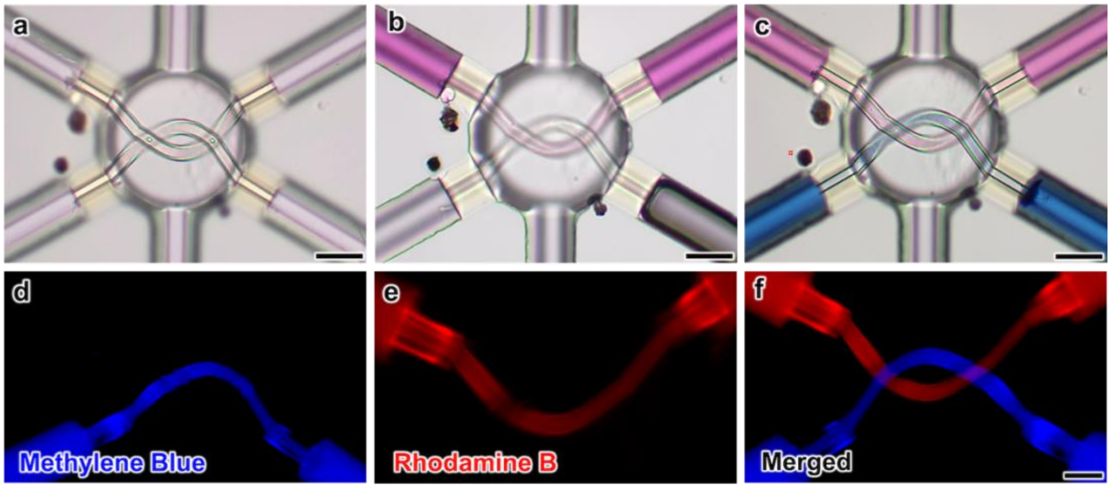

Figure 2.12*: Fluidic testing results of the interweaving microvessel structures: (****a****) prior to microfluidic loading, (****b****) after loading of rhodamine B-labelled fluid (pink), and (****c****) after loading of both rhodamine B-labelled fluid (pink) and methylene blue-labelled fluid (blue). Fluorescence micrographs of the microvessel structures filled with distinctly labelled fluids. (****d****) Methylene Blue, (****e****) Rhodamine, and (****f****) Merged. Scale bars = 50 µm. (see also* ***Movie 2.4****.*

As recent efforts based on alternative additive manufacturing approaches have faced difficulties in recreating fully 3D interweaving tubular structures at sub-100 μm scales [61,87–89], these results suggest that the presented COP-based *is*DLW strategy could serve as an enabling technology for organ-on-a-chip systems that require physiologically accurate 3D nanostructured microfluidic components. One caveat to the fluorescence experimentation is that the photomaterial in this study exhibits autofluorescence at lower wavelengths (*e.g.*, 405 nm and 480 nm); however, as researchers have demonstrated DLW-based manufacturing with a wide range of photomaterials – including those that lack autofluorescence at such wavelengths – applications that rely on detecting fluorescence properties should utilize alternative photomaterials for *is*DLW [90,91].

2.5. "Normally Open" Microfluidic Transistor

The manufacturing of 3D microfluidic systems that comprise active valving elements represents an exemplar with which to investigate the efficacy of COP-based *is*DLW in situations that simultaneously demand sophisticated architectures as well as complex functionalities. Here we designed and printed a bellowed-type *NO* microfluidic transistor inside of COP-COP microchannels that consists of two fundamental regions: (*i*) a source-to-drain flow path that includes a centrally located top orifice for source fluid entry and a laterally positioned orifice for the drain output, and (*ii*) a separate gate area that includes a 3D bellowed microstructure (**Fig. 2.13**). Under an applied source pressure (P_S), the fluid flow through the microfluidic transistor is unobstructed, passing through the top orifice, bypassing the bellowed component, and then flowing out of the lateral orifice (**Fig. 2.13a**). In contrast, when a gate pressure (P_G) of sufficient magnitude is applied, the 3D bellowed component deforms such that its top surface interacts with the source orifice to physically obstruct source-to-drain fluid flow (Q_{SD}) (**Fig. 2.13b**).

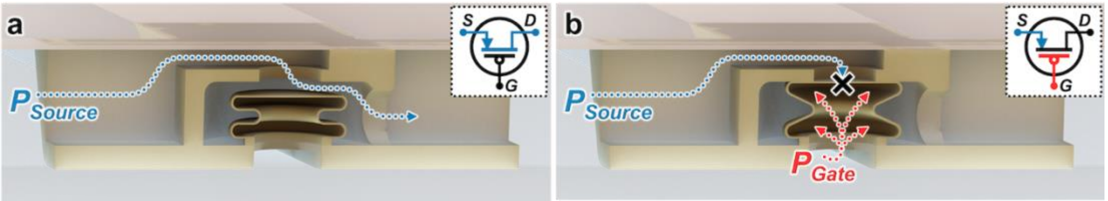

Figure 2.13*: Conceptual illustrations of the operating principle. (****a****) In the absence of a gate pressure (P_G), the source pressure (P_S) drives fluid flow through the microfluidic transistor. (****b****) An applied P_G causes the bellowed microstructure to expand and physically block fluid flow through the microfluidic transistor. Insets include analogous electronic circuit symbols.*

2.5.1. Theoretical Modeling

Here we use theoretical models to examine both the mechanical characteristics of specific components of the transistor assembly, as well as the structural and fluidic operation of the full transistor. First, to investigate the deformation mechanism of the flexible bellowed component. We employ a previously derived analytical model [92] to quantify the theoretical axial stiffness (k) of the bellowed component, which is calculated as,

$$k = \frac{6EI}{n\left(6\pi a^3 + 24fa^2 + f^3 + 3\pi f^2 a\left(1 + \frac{s^2}{12a^2}\right)\right)} \tag{3}$$

and

$$I = \frac{\pi s^3(r_o + r_i)}{12} \tag{4}$$

where E is the modulus of elasticity, I is the area moment of inertia, and n is the number of convolutions. While the dimensional design characteristics of the bellow (**Fig. 2.14a**) are represented by the inner radius of the bellow (r_i), outer radius of the bellow

(r_o), the radius of the convolution (a), the flank distance between the convolutions (f), and the thickness of the bellow (s).

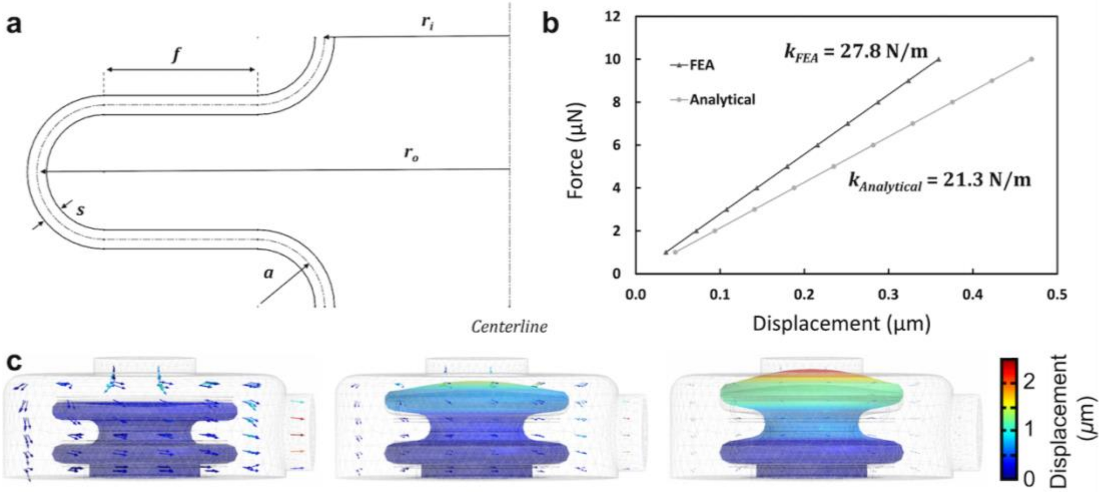

***Figure 2.14**: Theoretical results of the NO microfluidic transistor (**a**) a 2D sketch representing the geometric variables in one convolution (n=1) of the axisymmetric flexible bellow. (**b**) Stiffness characteristics of the flexible bellow for both FEA and analytical (eqn. 3) models, with results corresponding to n=0.5, r_i=7.5 µm, r_o=15 µm, a=1.75 µm, f=4 µm, and s=0.5 µm. (**c**) Sequential 3D COMSOL Multiphysics fluid–structure interaction (FSI) simulation results for fluid velocity field (colored arrows) and displacement distribution for the microfluidic transistor with P_S = 10 kPa and P_G increasing from (left) 0 kPa to (right) 90 kPa (see also **Movie 2.5**).*

To validate the bellow stiffness results obtained from the analytical model described by eqns. 3 and 4, FEA simulations were also performed with the solid mechanics module in COMSOL Multiphysics software. Using these two models, the stiffness was calculated for the following design parameters of n = 0.5, r_i = 7.5 μm, r_o = 15 μm, a = 1.75 μm, f = 4 μm, and s = 0.5 μm, and material properties for IP-L 780 (E = 1.75 GPa and v = 0.49) [67]. Results from the analytical model (eqn. 3) revealed axial stiffness of 21.3 N/m, while results from FEA simulations corresponded to stiffness of 27.8 N/m (**Fig. 2.14b**). In comparison, the stiffness obtained from the analytical model was 23% smaller than the value obtained using FEA. This variation is consistent with previous findings [92], where results calculated using the same analytical model were found to be 28-30% smaller compared to both FEA and experimental results.

Next, to gain insight into the overall fluidic performance, we conduct FEA simulations of the *NO* microfluidic transistor using COMSOL software. First, the 3D CAD model was imported into the FEA software, and simulations were performed using the FSI module under stokes flow conditions and quasi-static structural transient behavior. The photomaterial, IP-L 780 (E = 1.75 GPa and ν = 0.49) [67], and water (ρ = 10^3 kg/m^3; $\eta = 8.9 \times 10^{-4}$ Pa·s) were modelled for the solid elements and input fluid, respectively. To simulate microfluidic transistor operation, the pressure applied to the gate region was modelled as a boundary load assigned to the internal surface of the bellowed element. The pressure applied to the interior of the bellowed structure was varied from 0 kPa to 90 kPa using a parametric sweep function, while the source fluid input was maintained at a constant pressure of 10 kPa (**Fig. 2.14c**; **Movie 2.5**).

Initially for P_G = 0 kPa, Q_{SD} was at its maximum value (**Fig. 2.14c – left**). As P_G increased, however, the bellowed structure deformed toward the source orifice, thereby increasing the hydraulic resistance through the microfluidic transistor and reducing the magnitude of Q_{SD} (**Movie 2.5**). For P_G > 90 kPa, we observed complete obstruction of Q_{SD} based on contributions from two components of the bellowed microstructure: (*i*) deformations stemming from the bellows, and (*ii*) expansion of its top surface into the orifice (**Fig. 2.14c – right**). Although the simulation results for an ideal microfluidic transistor revealed full sealing due to interactions along a single circular edge, it is likely that full Q_{SD} obstruction during experimentation would require a higher degree of contact between the top surface of the bellowed microstructure and the surfaces adjacent to the source orifice.

2.5.2. Fabrication Results

To experimentally characterize the 3D microfluidic bellow-type transistor, we printed the component at a t-junction of a COP-COP device with trapezoidal microchannels of 30 μm in height (**Fig. 2.15a and b; Movie 2.6**). SEM micrographs of a printed cross section revealed effective fabrication of the 500 nm-thick walls of the bellowed microstructure and the 2 μm gap between the bottom surface of the source orifice and the top surface of the bellowed structure, with an absence of stiction-based failure modes (*e.g.*, premature sealing to the source orifice, collapsing of the bellowed components) (**Fig. 2.16a**). During experimental actuation of the *is*DLW-printed microfluidic transistor, varying the magnitude of P_G resulted in optically observable deformations of the bellowed microstructure (**Fig. 2.16b; Movie 2.7**).

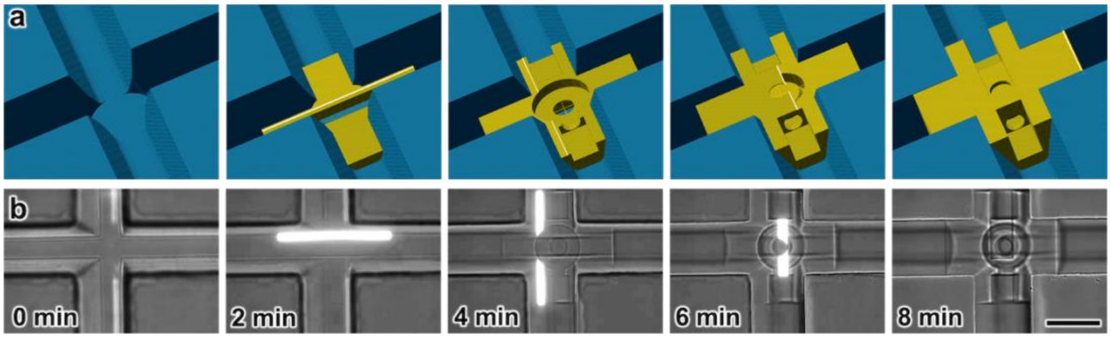

***Figure 2.15**: Sequential images of (**a**) CAM simulations, and (**b**) corresponding fabrication results for the isDLW printing process (see also **Movie 2.6**). Scale bar = 50 μm.*

2.5.3. Microfluidic Testing

We quantified the operational performance of the microfluidic transistor by varying P_S at increasing increments of P_G while monitoring the corresponding Q_{SD} (**Fig. 2.16c**). For P_G ranging from 0 kPa to 100 kPa, increasing P_G resulted in slight reductions in the relatively linear relationships between Q_{SD} and P_S (**Fig. 2.16c**). This behavior is an indication of increasing hydraulic resistance through the source-to-drain flow path within the microfluidic transistor, which is consistent with the simulation results (**Fig. 2.14c; Movie 2.5**). For P_G = 150 kPa, however, the experimental results revealed a full discontinuation of Q_{SD} (**Fig. 2.16c**).

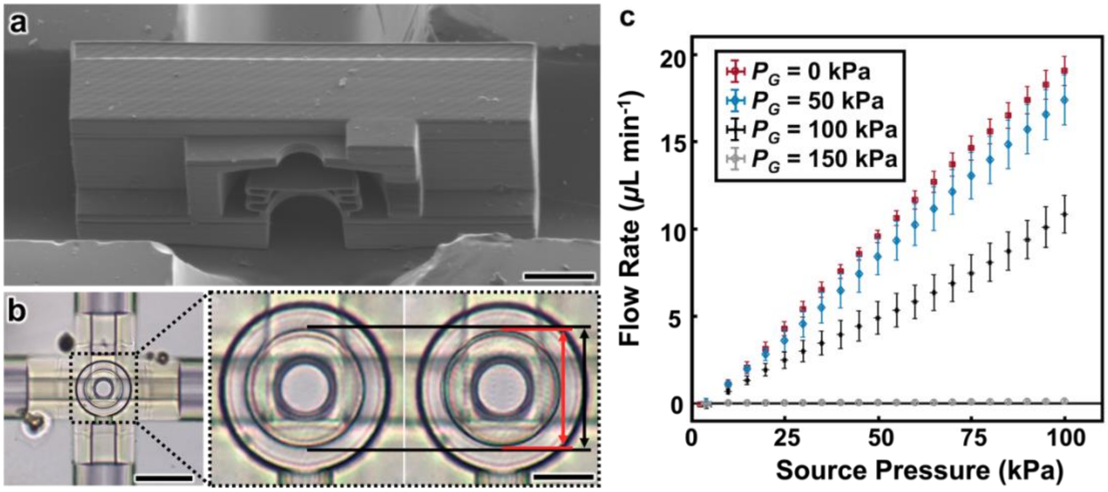

***Figure 2.16**: Results for the COP-based isDLW-printed 3D microfluidic bellow-type transistor. (**a**) SEM micrograph of fabrication results for an isDLW-printed microfluidic transistor cross section. Scale bar = 15 μm. (**b**) Micrographs of the microfluidic transistor during operation. Expanded views: (left) P_G = off; (right) P_G = on. Scale bars = 50 μm; (expanded view) 15 μm. (see also **Movie 2.7**). (**c**) Experimental results for source-to-drain fluid flow (Q_{SD}) versus P_S for varying P_G. Error bars = S.D. for n = 3 experiments.*

One potential basis for the observed trends for $P_G \leq 100$ kPa cases in which $P_G \gg P_S$ (*e.g.*, P_G = 100 kPa; P_S = 25 kPa), yet Q_{SD} persisted (**Fig. 2.16c**) is the effective mechanical stiffness of the bellowed microstructure. Specifically, sealing of the source orifice requires a sufficient magnitude of P_G to fully deform the bellowed structure such that the top surface displaces the complete distance from its initial state to the orifice (**Fig. 2.13b**). In this study, we observed that $P_G = 150$ kPa facilitated the desired functionality (**Fig. 2.16c**); however, it is important to note that the active sealing functionality of the 3D microfluidic bellow-type transistor can be readily tuned *via* geometric modifications. For example, the effective stiffness of the bellowed element can be reduced by increasing the size or the number of convolutions in the bellow, thereby resulting in comparatively larger displacements for a given P_S. Alternatively, the designed distance from the top surface of the bellowed structure to the source orifice can be decreased to limit the amount of deformation required for the initiation of bellow-orifice interactions.

Chapter 3: COP-based *is*DLW of "Normally Closed" Microfluidic Transistor

3.1. Background and Scope

Historically, the manufacturing of miniaturized fluidic systems has relied predominantly on micromachining methods developed for the semiconductor and microelectromechanical systems (MEMS) [24,93] industries. Motivated by the benefits inherent to manipulating fluids at smaller scales (e.g., for chemistry and biology) [94,95], researchers initially focused on adapting such microfabrication protocols for microfluidic device construction [96]. Consequently, the earliest microfluidic systems comprised standard, mechanically stiff semiconductor materials, such as silicon [97] and glass [98], until the introduction of "soft lithography" [99]. Building upon the elastomeric replication methods of Bell Labs [100], the Whitesides group reported a technique for molding and bonding silicone elastomers to form enclosed microchannels [101]. The Quake group harnessed an extension of this protocol in which multiple, discrete layers of micromolded elastomeric materials (and/or membranes) are bonded together – termed "multilayer soft lithography" – to demonstrate a novel microfluidic valve capable of actively regulating fluid flow via a control input [102]. This capability gave rise to the first generation of integrated fluidic circuits (IMCs), which investigators employed for a diversity of chemical, biological, and biomedical applications [103–105].

In response to the increasing numbers of microfluidic valves incorporated into IMCs, and in turn, the demands for off-chip equipment required to perform on-chip fluidic processes – i.e., the "tyranny of microfluidic interconnects" – investigators have explored additional strategies to realize IMCs with autonomous functionalities [93,106,107]. Drawing inspiration from electronic circuitry [108], researchers pioneered a second generation of IMCs by adapting multi-layer soft lithography to achieve fundamental fluidic analogues, including two-layer fluidic capacitors [70], three-layer fluidic diodes [70,71] and *NO* fluidic transistors [71], and five-layer *NO* pressure-gain fluidic transistors [109]. Although IMCs based on such components found only limited use in chemical and biological communities over the past decade, the emergence of "soft robotics" – classes of robots based on compliant materials that are actuated via fluidic means – has reinvigorated interest in self-regulating IMCs [110–112]. In particular, Wehner et al. leveraged their previously reported multi-layer soft lithography-based microfluidic oscillator to successfully demonstrate an untethered soft "octobot" capable of autonomous, periodic actuation of its tentacles [72]. Unfortunately, multi-layer soft lithography protocols suffer from a wide range of drawbacks, including: (*i*) cost, time, and labor-intensive manufacturing processes, (*ii*) limited device reproducibility (e.g., due to manual alignment and bonding procedures), (*iii*) access and training-based restrictions associated with clean rooms and equipment, and (*iv*) geometric (e.g., planar) limitations inherent to photolithography and micromolding [2,113,114]. Consequently, there is significant interest in alternative methodologies for IMC construction [7,68].

Recently, a third generation of IMCs has emerged founded on the use of additive manufacturing (or colloquially, “three-dimensional (3D) printing”) technologies [115]. Although our group and others have demonstrated the ability to fabricate microfluidic circuitry using a variety of additive manufacturing approaches, including extrusion-based printing (e.g., direct ink writing) [116], vat photopolymerization (e.g., stereolithography) [64,117,62,118,119], and material jetting (e.g., multijet modeling and polyjet printing) [120,121], such efforts have remained at relatively large scales (e.g., in the submillimeter-to-millimeter range rather than sub-100-μm) and only involved *NO* microfluidic transistor operational modes [63,64,116]. To leverage the unparalleled precision and geometric versatility of DLW [122,123] for microfluidic circuit element manufacturing, our group recently introduced an approach termed *is*DLW by which 3D microfluidic components can be printed directly inside of – and notably, fully sealed to – enclosed microchannels [43,45]. In this Chapter, we build on our developments in *is*DLW-based microfluidic circuitry introduce the first 3D printed *NC* microfluidic transistor [46], the transistor is designed so that it allows for gate activation characteristics to be customized geometrically. Next, with respect to soft robotics [124–128], and in particular, soft microbotics applications [129–131], we investigate an *is*DLW-printed microfluidic system comprising soft microgrippers integrated with distinct microfluidic transistors for which all microgripper actuation states are regulated by the magnitude of a single gate pressure input [47].

3.2. “Normally Closed” Microfluidic transistor

3.2.1. Concepts

The fabrication of the *NC* microfluidic transistor involves two key stages: *(i)* fabrication of the COP microfluidic device (**Fig. 3.1a**), and *(ii) is*DLW of the microfluidic transistor directly inside of (and fully sealed to) the COP-COP channels (**Fig. 3.1b**), The *is*DLW approach involves filling the microchannels with a liquid-phase photomaterial, and then selectively curing the photomaterial point-by-point, layer-by-layer, *via* two-photon polymerization phenomena (**Fig. 3.1b**). The *NC* microfluidic transistor is comprised of two key elements: *(i)* a free-floating sealing disc (3D printed without support structures), and *(ii)* a bellowed microstructure (wall thickness ≈ 500 nm) with a centrally located micropost (4 μm in diameter) on the top surface (**Fig. 3.1c**). In the absence of a P_G input, fluidic forces cause the disc to seal atop the centrally located orifice, thereby obstructing Q_{SD} through the microfluidic transistor (**Fig. 3.1d**). When a P_G of sufficient magnitude is applied, however, the bellowed microstructure expands such that the micropost physically disengages the disc's seal on the orifice, which in turn, promotes Q_{SD} (**Fig. 3.1e**).

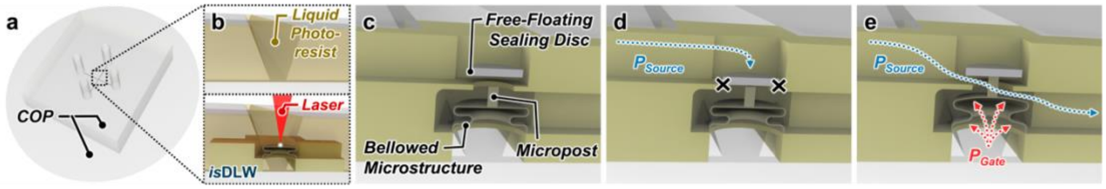

***Figure 3.1**: NC microfluidic transistor concept. (**a**) COP microfluidic device is filled with photoresist and loaded into the two-photon DLW 3D nanoprinter. (**b**) Expanded view of (top) liquid-phase photoresist in the microchannel and (bottom) isDLW of the 3D microfluidic transistor directly inside of the COP-COP microchannel. (**c**–**e**) Microfluidic transistor design and operation. (**c**) Initial state directly after printing. (**d**) “Closed” state. In the absence of a gate input, the sealing disc obstructs source-to-drain fluid flow (Q_{SD}). (**e**) “Open” state. An applied gate pressure (P_G) results in vertical expansion of the bellowed microstructure, causing the micropost to physically displace the sealing disc to allow Q_{SD} through the component.*

3.2.2. Fabrication Results

CAM simulations and corresponding micrographs of the fabrication results for *is*DLW-based 3D printing of the *NC* microfluidic transistor in COP-COP microchannels are presented in **Figure. 3.2 (***also see* **Movie 3.1)**. The total print time for the 30-μm-tall microfluidic components was approximately 9 min. The free-floating sealing disc was printed as the final step, directly inside of the rectangular compartment. Due to the quasi-static flow conditions within the sealing compartment, the 2-μm-thick disc was able to be 3D printed without the need for support structures.

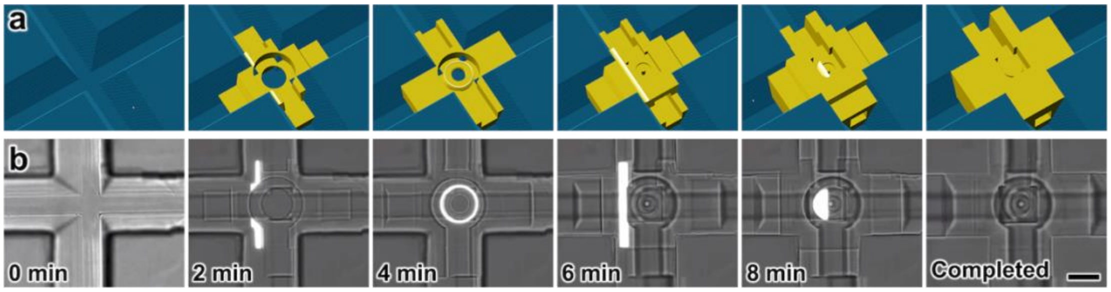

***Figure 3.2**: Fabrication results for the NC microfluidic transistor. (**a**) CAM simulations. (**b**) Corresponding isDLW results. Total time = 9 min; scale bar = 25 µm. (total time ≈ 9 min; see **Movie 3.1**)*

3.2.3. Theoretical Simulations

We performed FEA simulations under a constant P_S and varying P_G to provide insight into the operational behavior of an ideal 3D *NC* microfluidic transistor (**Fig. 3.3**). The FEA simulations were performed using FSI module under stokes flow conditions and quasi-static structural transient behavior. The solid elements were modeled as the photomaterial, IP-L 780 (E = 1.75 GPa and $\nu = 0.49$) [67], while the input fluid was modeled as water ($\rho = 10^3$ kg/m^3; $\eta = 8.9 \times 10^{-4}$ Pa·s). The pressure applied at the gate region was assigned to the interior surface of the bellow microstructure and was modeled as a boundary load to simulate the operating conditions. To simplify the computation, the sealing disc was set to be fixed atop the micropost. The simulations were performed for a constant P_S of 10 kPa, with P_G increasing from 0 kPa to 100 kPa by increments of 10 kPa.

In the absence of a P_G input, Q_{SD} remained fully blocked; however, increasing the magnitude of P_G caused the bellow microstructure to expand, thereby displacing the disc away from the orifice and facilitating Q_{SD} (**Fig. 3.3a**). The simulation results revealed a key constraint for the presented design as cases associated with P_G inputs that are too high could cause the bellow microstructure to inflate to such a degree that its top surface could physically seal along the underside of the orifice – similar to the *NO* 3D microfluidic transistor reported previously. Such phenomena provide a basis for the decreasing slopes of the Q_{SD} - P_G relationships exhibited at higher P_G (**Fig. 3.3b**). One caveat to the simulation results is that, by setting the sealing disc as a moving boundary (i.e., the disc's position is determined by the micropost's location), the fluidic forces applied to the disc were not considered. Although this simplification could lead to variations between theoretical and experimental results, we expect that divergences from the disc's planar orientation (as modeled) to an inclined configuration would likely enhance the P_G-mediated "open state" Q_{SD} performance.

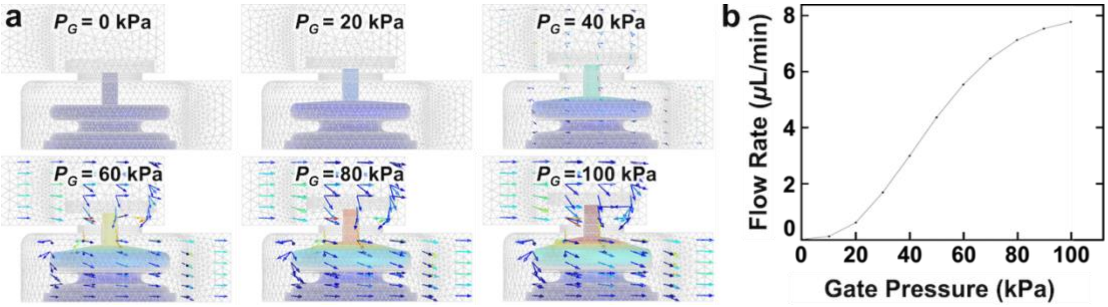

***Figure 3.3**: (**a**) Finite element analysis (FEA) fluid-structure interaction (FSI) simulation results (P_S = 10 kPa). (**b**) Simulation results for Q_{SD} versus P_G (P_S = 10 kPa).*

3.2.4. Microfluidic Testing

We conducted preliminary optical characterizations of the *is*DLW-printed microfluidic transistor by infusing fluids into the device and then using both brightfield (**Fig. 3.4a-c**) and fluorescence (**Fig. 3.4d-f**) microscopy to evaluate performance. For example, applying a P_S without a P_G input caused the disc to instantly move towards the central orifice; however, applying a P_G input resulted in optically observable displacements of the sealing disc away from the orifice (**Fig. 3.4b and c; Movie 3.2**). In addition, we investigated the capacity for the microfluidic transistor to isolate the source-to-drain and gate flow paths – a critical requirement for operational functionality – by loading two distinct fluorescently labeled fluids corresponding to each flow path (**Fig. 3.4d-f**). The fluorescence microscopy results revealed that the two distinct fluorescence signatures were successfully maintained within their respective channels, without any visible signs of undesired cross-contamination found in either opposing flow path.

To quantify the fluidic performance of the *NC* microfluidic transistor. Experimental testing was performed – using DI water – by varying P_S from 0 kPa to 150 kPa at a rate of 1 kPa/s, while recording the corresponding Q_{SD} through the microfluidic transistor (**Fig. 3.4g**). The same procedure was then repeated for distinct P_G inputs, ranging from 0 to 300 kPa using 50 kPa increments. Data from all completed experiments were then collected and processed using MATLAB software to calculate and plot the mean and standard deviation (S.D.) of Q_{SD}.

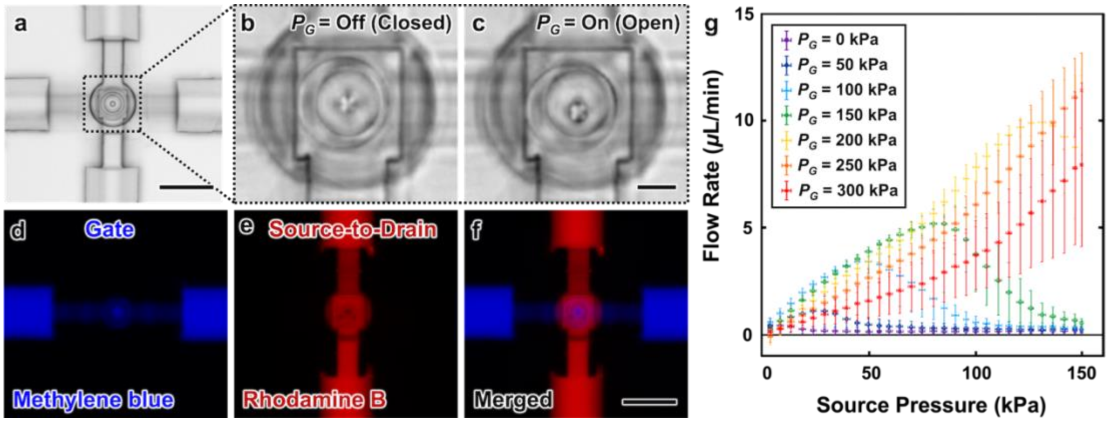

***Figure 3.4**: Experimental results for NC microfluidic transistor operation. **(a–c)** Brightfield micrographs of the **(a)** microfluidic transistor, with expanded views corresponding to the **(b)** "closed" state (P_G =Off), and **(c)** "open" state (P_G =On). Scale bars = **(a)** 50 μm (see **Movie 3.2**); **(b, c)** 10 μm. **(d-f)** fluorescence micrographs corresponding to distinct dyed fluids inputted into the: **(d)** gate microchannel, and **(e)** source-to-drain microchannel. **(f)** merged. Scale bar=50 μm. **(g)** Microfluidic testing results for Q_{SD} versus P_S at varying P_G. error bars = S.D. For n=6 experiments*

The experimental results revealed three fundamental operational modes exhibited by the microfluidic transistor based on the magnitude of the P_G inputs (**Fig. 3.4g**). For P_G = 0 kPa, the transistor effectively blocked Q_{SD} over the entire range of P_S investigated (*i.e.*, $P_S \leq 150$ kPa). This behavior can be attributed to the disc effectively obstructing flow through the central orifice in cases where there was no contribution from the bellowed microstructure. Which is unlike *NC* transistors demonstrated before in literature [106,132–137], where the initial "closed status" (when P_G = 0) of the transistor is contingent on the condition that P_S is small enough not to deform the elastomeric layer used to block the flow to the drain. The second mode corresponded to P_G inputs from 50 kPa to 200 kPa, for which we observed that Q_{SD} initially increased with increasing P_S until it reached a maximum Q_{SD} ($Q_{SD,\max}$), after which the magnitude of Q_{SD} decreased (approaching 0 μL/min). We found that the $Q_{SD,\max}$ inflection point was highly dependent on P_G, with larger P_G inputs leading to larger magnitudes of $Q_{SD,\max}$ occurring at larger P_S inputs. One potential basis for these results is the force balance associated with the floating disc and the bellowed microstructure. Specifically, the $Q_{SD,\max}$ inflection points suggest that for a given P_G, there is a magnitude of P_S at which the fluidic forces induced by the source flow overcome the opposing forces from the central micropost and bellowed microstructure. Such phenomena would cause the disc to approach its initial state, resealing the central orifice. It should be noted that although the results for $P_G \geq 250$ kPa did not reveal $Q_{SD,\max}$ values, it is likely that this absence is due to P_S not being large enough, rather than $Q_{SD,\max}$ values not existing for $P_G \geq 250$ kPa.

The third mode is associated with the trend that increasing P_G did not necessarily lead to larger magnitudes of Q_{SD} in many cases. For example, for P_S =100 kPa, a P_G input of 300 kPa led to significantly lower Q_{SD} compared to a P_G input of 200 kPa (*i.e.*, 3.72 ± 1.61 μL/min *versus* 7.84 ± 0.65 μL/min, respectively). Such results are likely due to the bellowed microstructure deforming to such a degree that the top surface begins approaching the central orifice, which would increase the hydrodynamic resistance through the microfluidic transistor, and in turn, reduce Q_{SD}. These results suggest that P_G should be tuned for particular conditions (rather than arbitrarily increasing P_G).

3.3. IMC for Soft Microrobotic actuation

3.3.1. Concepts

A fundamental benefit inherent to additive manufacturing technologies is the ability to readily customize the geometries of printed components. For the *NC* microfluidic transistor, a number of geometric factors could be adjusted to alter its performance, such as the dimensions of the bellow microstructure (e.g., wall thickness, number of bellows, bellow diameter) as well as the diameter of the sealing disc. In this section, we explore the effects of modifying the sealing disc diameter to influence the relationship between P_G and Q_{SD} – i.e., to tune the gate activation pressure required for the microfluidic transistor to transition from the "closed state" to the "open state". We then use this ability to demonstrate sequential actuation of two identical microgrippers within an integrated microfluidic circuit.

The Bulk microfluidic platform was fabricated using the COP-based *is*DLW process (**Fig. 3.5a-e**). The two microfluidic transistors are designed similarly to what was described in the previous section with the exception being the diameter of the free-floating sealing disc: (*i*) D1 = 25 μm, and (*ii*) D2 = 26 μm (**Fig. 3.5f-i**). On the other hand, the operation of the soft microgrippers is similar to that of established soft actuators at larger scales [138,139], with two mirrored actuators comprising asymmetric bellows that yield deformation toward one another during inflation routines. Such components can be modeled as fluidic capacitors [72].

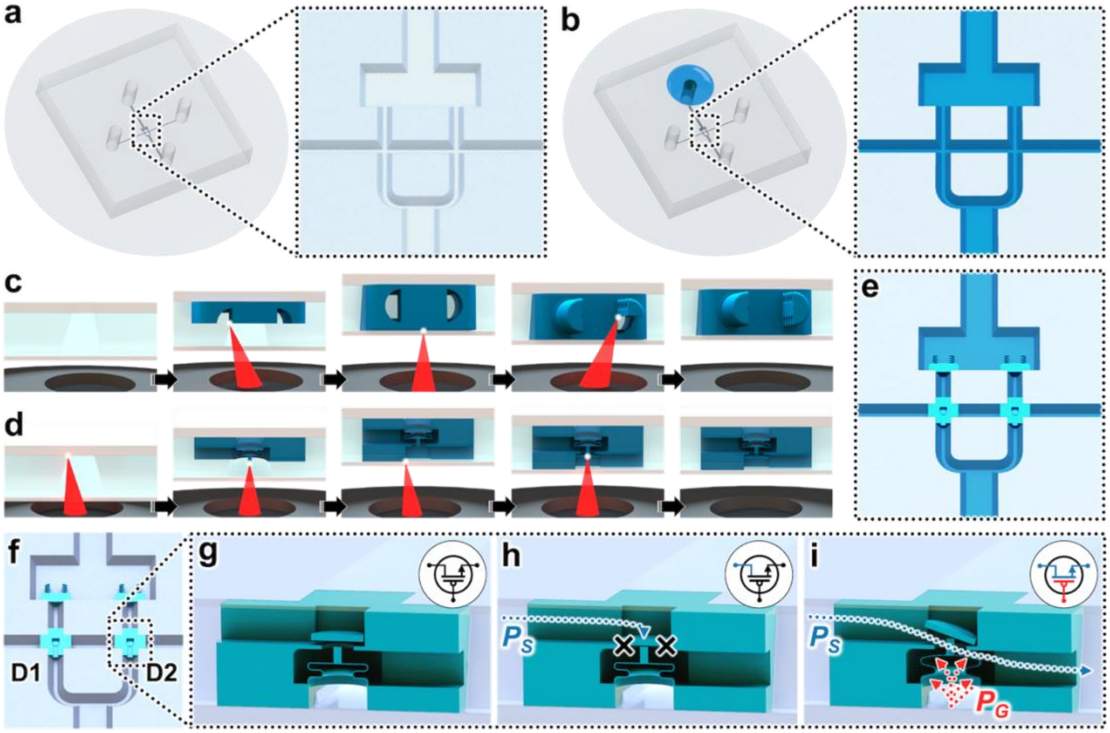

***Figure 3.5**: Conceptual illustrations of the isDLW strategy for 3D printing NC microfludic transistors and soft microgrippers in a COP microfluidic system. (**a**) Enclosed COP-COP microdevice with empty microchannels. (**b**) Infusion of a liquid-phase photomaterial into the COP–COP microchannels. (**c,d**) A focused femtosecond IR laser selectively polymerizes the photomaterial in a "ceiling-to-floor", point-by-point, layer-by-layer process to print the: (**c**) soft microgrippers, and (**d**) NC microfludic transistors. (**e**) Printed microfluidic components (comprised of cured photomaterial) that are fully adhered to the luminal surface of the COP–COP microchannel at designed locations. (**f**) The microfluidic system following development. (**g–h**) NC microfludic transistor operating principle. (**g**) Initial state directly after printing. (**h**) "Closed State". In the absence of a gate input, an applied source pressure (P_S) causes the free-floating disc to seal atop the central orifice, thereby obstructing source-to-drain fluid flow (Q_{SD}). (**i**) "Open State". Under the application of a gate pressure (P_G) of sufficient magnitude, the bellow microstructure expands in a manner that causes the central micropost to physically displace the sealing disc from the orifice to promote Q_{SD}.*

3.3.2. Fabrication Results of IMC System

CAM simulations and corresponding micrographs of fabrication results for DLW-based printing of the negative master mold are shown in **Fig. 3.6a and b**, respectively. Due to the large print area of the channel mold structures (approximately 5 mm × 5 mm), we employed a stitching-based print methodology by which the master mold was printed in 300 μm × 300 μm areas that connect together. This process resulted in a total print time of approximately 16 minutes (**Fig. 3.6b; Movie 3.3**). The print time could be reduced dramatically by using an objective lens with a lower magnification (e.g., 10×) [140]. One caveat to using a lower magnification objective lens is that the feature resolution would be diminished slightly; however, it is unlikely that such a change would negatively affect the mold due to its scale and simple geometry. SEM micrographs revealed effective printing of the 40-μm-tall, trapezoidal microchannel molds (**Fig. 3.6c**) and its microreplication using the COP sheet (**Fig. 3.6d**).

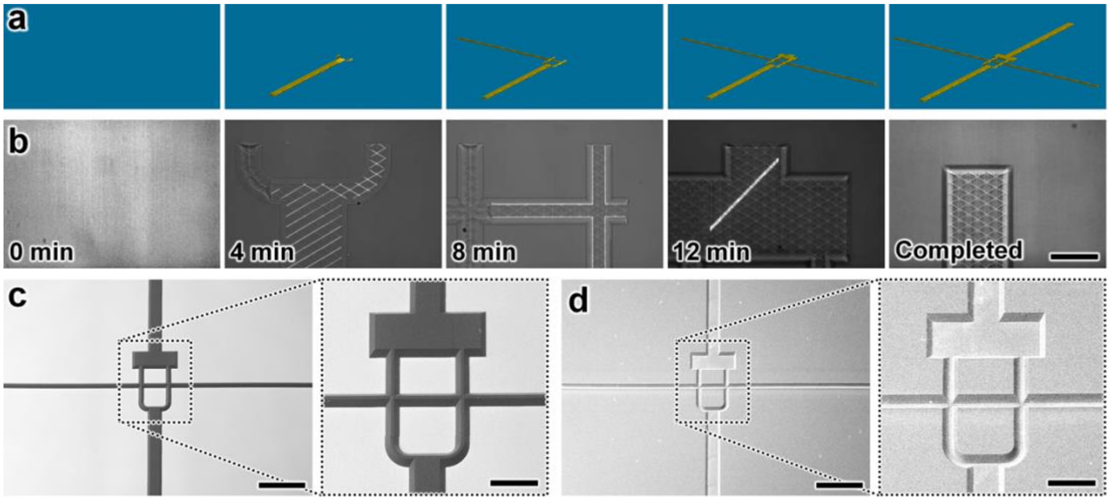

Figure 3.6*: Fabrication results for DLW-printing of the trapezoidal microchannel negative master mold and subsequent COP-based microreplication.* ***(a,b)*** *Sequential* ***(a)*** *CAM simulations, and* ***(b)*** *corresponding micrographs of the DLW printing process (see* **Movie 3.3***). Total time ≈ 16 min; Scale bar = 50 µm.* ***(c,d)*** *SEM micrographs of the* ***(c)*** *DLW-printed master mold, and* ***(d)*** *hot embossing- replicated COP sheet. Scale bars = 500 µm; Expanded view scale bars = 100 µm.*

The *is*DLW fabrication process of the *NC* transistors was performed as described in section 3.2 (**Fig. 3.7a and b**). On the other hand, for the microgrippers, the fabrication process consisted of three steps: (*i*) printing of the structure-to-microchannel interfacing component, (*ii*) printing one soft actuator, and then (*iii*) printing the remaining soft actuator (**Fig. 3.7c and d; Movie 3.4**). The total print time for a complete soft microgripper (i.e., consisting of two soft actuators) was less than 6 minutes (**Fig. 3.7d; Movie 3.4**). SEM micrographs of fabrication results for a microfluidic transistor and a soft microgripper are presented in **Fig. 3.7e and f**, respectively.

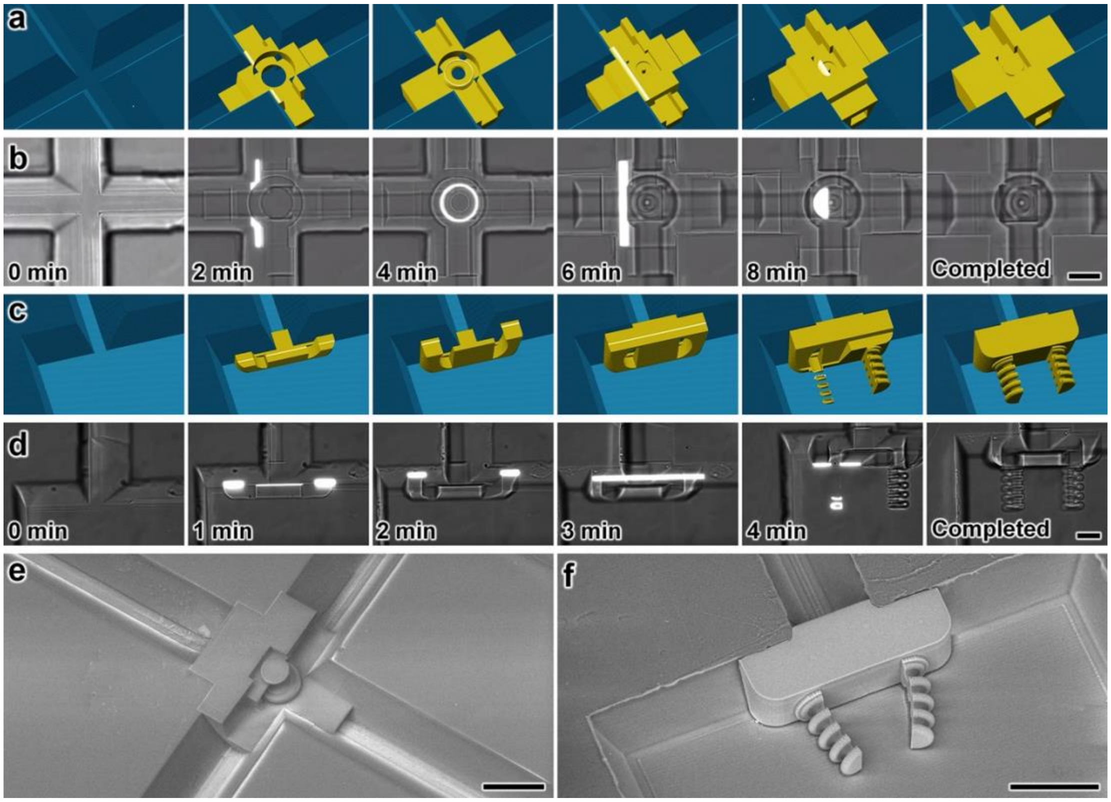

Figure 3.7: *Fabrication results for isDLW-printing of NC microfluidic transistors and soft microgrippers. (**a–d**) Sequential (**a,c**) CAM simulations, and (**b,d**) corresponding micrographs of the isDLW printing process for (**a,b**) NC microfluidic transistor (total time ≈ 9 min; see **Movie 3.1**), and (**c,d**) soft microgripper (total time ≈ 6 min; see **Movie 3.4**). Scale bars = 25 μm. (**e,f**) SEM micrographs of a: (**e**) NC microfluidic transistor cross section, and (**f**) soft microgripper. Scale bars = 50 μm.*

3.3.3. Microfluidic Testing of D1 and D2 Transistors

To quantify the fluidic performance of each microfluidic transistor, we measured the magnitude of Q_{SD} corresponding to distinct, constant P_S inputs and varying P_G inputs (**Fig. 3.8**). Experimental results for the D1 microfluidic transistor revealed three fundamental operational modes based on the magnitude of the P_G input (**Fig. 3.8a**). For lower P_G magnitudes (e.g., $P_G < 100$ kPa), the sealing disc effectively obstructed Q_{SD} for all P_S inputs examined. The second mode involved the gate activation and the corresponding onset of Q_{SD}, which occurred for P_G magnitudes in the range of approximately 100 kPa to 150 kPa for the P_S inputs tested. Consistent with the simulation results (**Fig. 3.3b**), we observed a third mode at higher P_G magnitudes as the slope relating Q_{SD} to P_G began decreasing with increasing P_G (**Fig. 3.8a**).

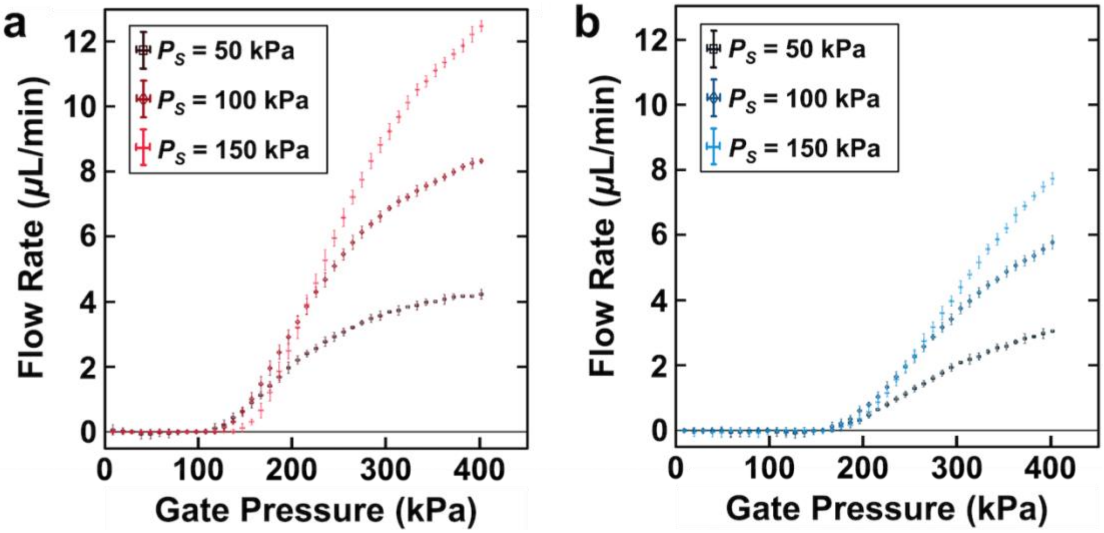

*Figure 3.8: Quantified experimental results of the NC transistors for Q_{SD} versus P_G at varying P_S for the: (**a**) D1 microfluidic transistor (disc diameter = 25 μm), and (**b**) D1 microfluidic transistor (disc diameter = 26 μm). Error bars denote S.D.*

In particular, for a P_S input of 50 kPa, Q_{SD} appeared to approach a maximum value, after which it is expected that the magnitude of Q_{SD} would instead begin plateauing or decreasing with increasing P_G. Overall, the results for the D2 microfluidic transistor were consistent with the trends shown with D1; however, we found that the increase in the sealing disc diameter resulted in a slight shift in the data toward higher P_G magnitudes (**Fig. 3.8b**). For example, the gate activation region instead occurred in the range of approximately 150 kPa to 175 kPa for the P_S inputs investigated. In addition, the Q_{SD} - P_G relationships for the D2 microfluidic transistor exhibited reduced slopes (and smaller Q_{SD} magnitudes) compared to their D1 counterparts (**Fig. 3.8**). In combination, these results suggest an important role for the sealing disc diameter in regulating the gate activation region. One caveat, however, is that the P_G input should be tailored to particular target conditions rather than increasing the P_G input arbitrarily, as doing so could yield the opposite of the desired effect at higher P_G magnitudes—i.e., reestablishing a "closed state".

3.3.4. Integrated NC Microfluidic Transistors and Soft Microgrippers

To initially explore the integration of the *NC* microfluidic transistors with the soft microgrippers, we designed a microfluidic system in which a soft microgripper was printed downstream of a single *NC* microfluidic transistor (**Fig. 3.9**). First, we applied a constant P_S without any P_G input. In this case, the microfluidic transistor effectively maintained its "closed state", blocking Q_{SD}, and in turn, precluding unintended microgripper deformation (**Fig. 3.9a-c**). However, by applying P_G input, the microfluidic transistor transitions to its "open state", permitting fluid flow through the component and into the soft microgrippers to yield successful actuation (**Fig. 3.9d-f; Movie 3.5**).

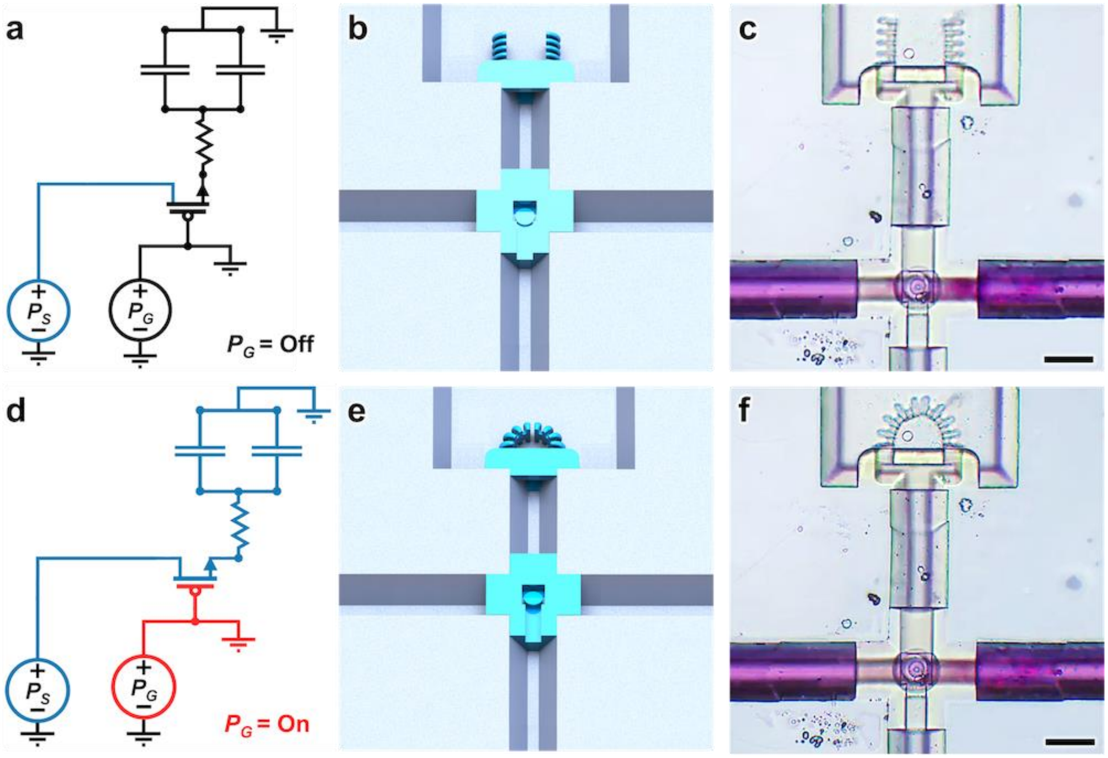

***Figure 3.9**: An integrated microfluidic system consisting of one microfluidic transistor and one soft microgripper (positioned downstream of the transistor drain) (**a,d**) Analogous circuit diagrams, (**b,e**) conceptual illustrations, and (**c,f**) brightfield micrographs of experimental results corresponding to the two fundamental operational modes based on a constant P_S input and a varying P_G input: (**a-c**) P_G = Off and (**d-f**) P_G = On. (see **Movie 3.5**). Scale bars= 50 µm.*

Next, we designed an IMC comprising two distinct *NC* microfluidic transistors (i.e., corresponding to the D1 and D2 discs) and two sets of soft microgrippers to yield hard-coded operations based on the magnitude of the P_G input (while an applied P_S remains constant at a set magnitude) (**Fig. 3.10a–f**). Specifically, under a constant P_S input, the functionality of the microfluidic system entails three fundamental P_G-mediated operational modes. In the absence of a P_G input, the P_S causes both microfluidic transistors to enter their “closed states” and prevent microgripper actuation (**Fig. 3.10a and d**). A second mode involves the application of an intermediate P_G magnitude that is high enough to yield gate activation for the D1 microfluidic transistor, but not so for the D2 microfluidic transistor. As a result, only the D1 microfluidic transistor is able to transition to the "open state", and thus, only the first set of microgrippers actuate (**Fig. 3.10b and e**). Lastly, under a high P_G input, the gates of both the D1 and D2 microfluidic transistors are activated (i.e., inducing the "open state"), resulting in both sets of soft microgrippers actuating (**Fig. 3.10c and f**).

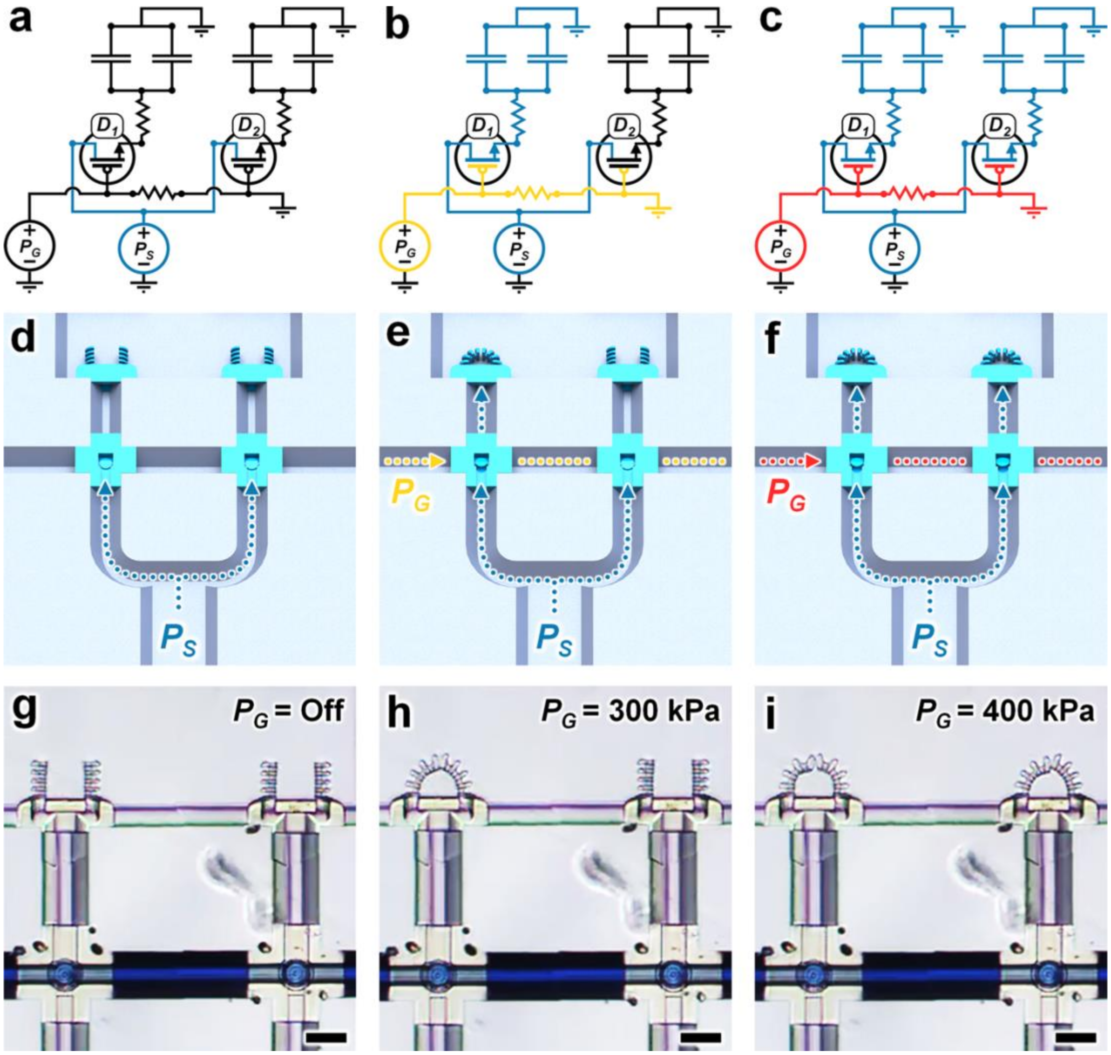

Figure 3.10*: An integrated microfluidic system consisting of the D1 and D2 NC microfluidic transistors with identical soft microgrippers positioned downstream of each drain. (****a–c****) Analogous circuit diagrams and (****d–f****) conceptual illustrations corresponding to the three fundamental operational modes based on a constant* P_S *input and a single varying* P_G *input: (****a,d****)* P_G *= Off; (****b,e****)* P_G *= Intermediate (i.e., capable of activating the gate of the D1 microfluidic transistor, but not that of the D2 microfluidic transistor); and (****c,f****)* P_G *= High (i.e., capable of activating the gates of the both microfluidic transistors). (****g–i****) Brightfield micrographs of experimental results for the microfluidic system under a constant* P_S *of 100 kPa and distinct* P_G *magnitudes: (****g****)* P_G *=0kPa;(****h****)* P_G *=300kPa; and (****i****)* P_G *=400kPa (see* ***Movie 3.6****). Scalebars= 50 µm.*

To experimentally investigate these capability, the P_S input was set at a constant magnitude of 100 kPa, while the P_G input was varied between three target magnitudes corresponding to the three operational states: (*i*) P_G = 0 kPa, both microfluidic transistors remained in the “closed state” – none of the soft microgrippers actuated (**Fig. 3.10g**); (*ii*) P_G = 300 kPa, the D1 microfluidic transistor exhibited gate activation and “open state” behavior – the corresponding (i.e., downstream) soft microgrippers actuated (**Fig. 3.10h**); and (*iii*) P_G = 400 kPa, both microfluidic transistors exhibited gate activation and “open state” behavior – both soft microgrippers actuated (**Fig. 3.10i**). During microfluidic testing, we observed that the actuation of the microgrippers was not instantaneous, but rather required more than one second to deform fully as designed (**Movie 3.6**). One potential basis for this trend is that akin to the time associated with charging an electronic capacitor, so too does each actuator – operating as a fluidic capacitor – necessitate an inflation time to physically expand to store fluid volume. In cases that demand more rapid microgripper actuation capabilities, it is expected that a higher P_S input would reduce such time delays. Nonetheless, these results demonstrate the ability to hard code P_G-mediated operational functionalities into unified IMC-microrobotic systems.

Chapter 4: Deterministic Lateral Displacement of Submicron Particles

4.1. Background and scope

In the past, researchers have primarily employed and/or adapted conventional microfabrication protocols for the production of microfluidic technologies. The associated feature resolutions have provided researchers with a number of scaling-induced benefits (*e.g.*, laminar flow profiles, low reagent volumes, and rapid reaction times) that have proven powerful for biomedical applications including organ modeling [141], diagnostics [142], and drug delivery [143,144]. One particular example of note is DLD – a continuous-flow microfluidic approach for guiding target suspended particles away from their initial laminar flow streams. DLD systems are typically comprised of high numbers of micro/nanoscale posts (or alternatively, pillars) that are arrayed at a slight angle with respect to the flow direction, with the key benefit that the size of displaced particles can be readily customized by modifying basic geometric design parameters that underlie post placement [145,146]. DLD was first reported in 2004 by Huang et al., [147] Who introduced this microfluidic technology as a substitute to conventional techniques for particle separation such as ultracentrifugation, [148–150] electrophoresis, [151–153] and ultrafiltration. [154,155] Generally, microfluidic-based particle separation technologies can be divided to two types, active [33,156–162] and passive [163–167] technologies. Active methods require the use of external forces such as electric, magnetic, and acoustic for particle separation. Passive methods on the other hand use the geometry of the channel or that of embedded structures to produce a hydrodynamic effect that supports the separation of suspended particles.

Motivated by the advantages of DLD – namely, passive and label-free particle processing – many groups have developed DLD arrays to efficiently sort, transport, isolate, and concentrate particles covering a wide range of scales (*e.g.*, DNA, bacteria, and stem cells) [168,169]. For designs tailored to submicron particles [170], however, fabricating such DLD devices has demanded increasingly complex manufacturing protocols. In particular, Wunsch *et al*. recently introduced an approach that combined photolithography, reactive-ion etching, e-beam lithography, deep-UV lithography, and glass-Si bonding methods to realize a nanoparticle-based DLD system [171]. Although beneficial for extracellular vesicle [171,172] and DNA [173,174] separations, such fabrication processes can be exceedingly time, labor, and cost-intensive, while posing additional training and access-based restrictions associated with equipment and/or facilities requirements [20]. Thus, alternative methodologies for producing DLD systems capable of processing submicron-scale particles are in critical demand.

Over the past decade, researchers have increasingly explored the use of submillimeter-scale additive manufacturing (or colloquially, “three-dimensional (3D) printing”) technologies for fabricating microfluidic devices, such as using stereolithography and multijet/polyjet printing. Recently, Jusková *et al.* used stereolithography to demonstrate the first 3D printed DLD systems [175,176]. One caveat, however, is that the minimum size of the target particles was on the order of 20 μm to 120 μm due to the resolution limitations of stereolithography – capabilities that are not suitable for applications that rely on DLD processing of submicron particles. Consequently, here we investigate the use of DLW – a two-photon polymerization based additive manufacturing technique with resolutions in the 100 nm range – for printing DLD systems that target submicron-scale particles.

4.2. Concept

In this chapter, we present a novel DLW-based manufacturing strategy for DLD array fabrication [48]. In previous chapters, we introduced *is*DLW strategies for printing microfluidic structures directly inside of (and fully sealed to) enclosed microchannels comprising PDMS and the thermoplastic COP. These studies revealed that COP is far superior as a substrate for direct attachment of DLW-printed features compared to PDMS. Unfortunately, the optical properties of a bottom substrate (*e.g.*, glass or COP) can slightly diminish the resolution and repeatability of DLW – particularly with respect to height-based power variations – to a degree that would compromise the precision required for submicron particle-based DLD arrays. To bypass such issues, here we instead utilize an unenclosed COP microchannel, with a liquid-phase photomaterial dispensed such that it completely fills the entirety of the microchannel (**Fig. 4.1a and b**).

Using a Dip-in Laser Lithography (DiLL) configuration in which the objective lens of the laser is immersed in the photomaterial, the DLD array is defined *via* selective photopolymerization events. Specifically, a tightly focused femtosecond pulsed IR laser is scanned point-by-point, layer-by-layer to induce localized 2PP in designed locations, first defining the boundaries (**Fig. 4.1c**) to the DLD array (fully sealed to the COP walls), and then printing the arrayed posts (**Fig. 4.1d**). Due to the precision afforded by the DLW printer, the DLD microstructures can be fabricated such that the height of the COP microchannel and the DLD array are effectively identical. As a result, once the print has been developed, a thin COP film can be permanently bonded to both the COP microchannel as well as the tops of the DLW-printed microstructures, thereby completely sealing the microfluidic device (**Fig. 4.1e**).

The fundamental design parameters for DLD arrays include the gap spacing between the posts (*G*) and the angle of the post array with respect to the flow direction (θ). The critical diameter D_C – *i.e.*, the minimum particle size that will be passively displaced or “railed” along the arrayed microposts – can be calculated using an empirical model [177]:

$$D_C = 1.4 \times \tan\theta^{0.48} \tag{5}$$

Although the height of the posts (*H*) is not included in eqn. 5, increasing *H* improves the potential throughput of a given DLD array design. Unfortunately, larger *H* can also lead to stiction-based failure modes for densely packed microposts. To prevent such issues while setting *H* to be much larger than the diamond-shaped posts ($3.5\ \mu\text{m} \times 3.5 \mu\text{m}$) [178], we leveraged the geometric versatility of DLW to construct horizontal support structures (*i.e.*, perpendicular to *H*) that reinforce the microposts at their midpoints (for $H = 22\ \mu\text{m}$). The support structures (diameter = 2 μm) connect the microposts along θ as well as perpendicular to the flow direction. These conditions are designed to promote a consistent *G* throughout the array while limiting the potential for the support structures to interfere with the capacity for the DLD system to effectively rail the suspended particles away from their original flow streams (**Fig. 4.1g and f**).

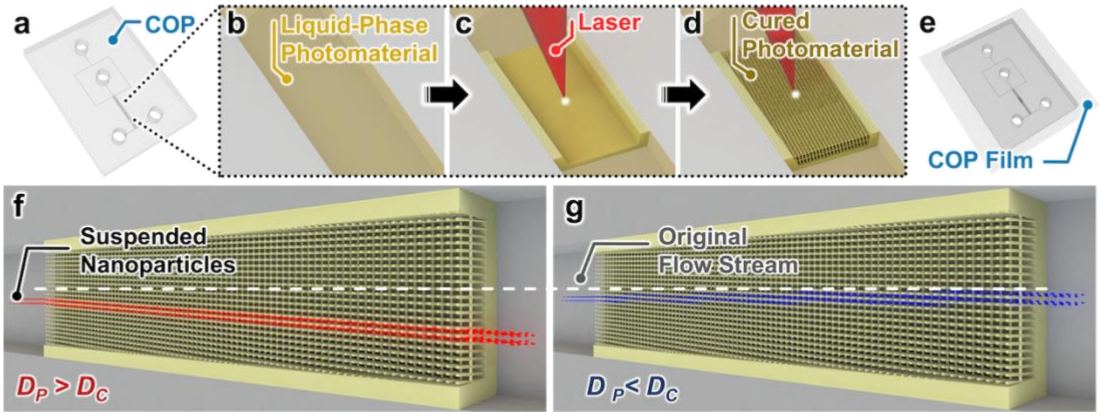

Figure 4.1 *Conceptual illustrations of the DLW-based methodology for additively manufacturing DLD arrays. (**a**) Micropatterned COP with an expanded view of the (**b**) unenclosed microchannel filled with a liquid-phase photomaterial. (**c**) The DLW process for printing the boundaries of the DLD fully adhered to the COP channel walls, and then the (**d**) DLD microstructures. (**e**) The sealed DLD microfluidic device following solvent-based bonding of a thin COP film to the micropatterned COP with embedded DLD array. (e,f) Passive effect of DLD system on particles suspended under continuous-flow conditions. (**f**) lateral displacement of larger particles ($D_P>D_C$) along the posts (arrayed at an angle with respect to the flow direction), away from their initial flow streams. (**g**) Smaller particles ($D_P<D_C$)* traveling along original flow stream.

4.3. Materials and Methods

4.3.1. COP channel fabrication and printing of DLD array

To manufacture the unenclosed COP microchannel, we employed a previously reported DLW-based method for COP-based microreplication. Briefly, the microchannel molds were modeled using the CAD software, SolidWorks (Dassault Systemes, France), exported as STL files, and then imported into the CAM software, DeScribe (Nanoscribe, Karlsruhe, Germany), for slicing and laser writing path generation. It is important to note that the microchannel geometry corresponding to the location of the eventual DLD array was designed with a trapezoidal cross-section to prevent print failures along the side walls.

A Si substrate (25 mm ×25 mm) was rinsed with acetone and IPA, and then dried with N_2 gas before being place on a 100 °C hot plate for 15 min. A drop of IP-S photoresist (Nanoscribe) was dispensed onto the Si substrate, which was then loaded into the Nanoscribe Photonic Professional GT printer in the DiLL configuration for DLW of the negative mold using a 25× objective lens. After the DLW process, the substrate was developed using PGMEA and IPA, and then dried with N_2 gas. A 4-mm-thick COP sheet (ZEONOR 1060R, Zeon Corp., Japan) was rinsed with IPA and dried with N_2 gas. Using the printed negative master mold, the patterns were replicated onto the COP sheet *via* hot embossing for 3 min at 120 °C. Afterward, ports were drilled at inlet/outlet locations.

Similar to the unenclosed COP microchannel, the DLD array design was modeled in SolidWorks and imported into DeScribe for fabrication with the Nanoscribe DLW printer. A drop of IP-Dip photoresist (Nanoscribe) was dispensed directly onto the unenclosed COP microchannel – *i.e.*, fully covering the intended location of the DLD array – and then loaded into the Nanoscribe printer in the DiLL configuration for DLW of the DLD structures using a 25x objective lens. The unenclosed DLD array was developed using PGMEA and IPA, and then dried with N_2 gas.

To achieve a fully enclosed microfluidic system, we employed a solvent-based bonding process using cyclohexane solvent. A thin COP film (microfluidic ChipShop GmbH, Germany) was exposed to cyclohexane vapor at 30 °C for approximately 2 min. Directly after the vapor exposure process, the exposed surface of the COP film was brought into contact with the unenclosed surface of the micropatterned COP (and embedded DLD array) to facilitate a permanent bond, thereby fluidically sealing the device.

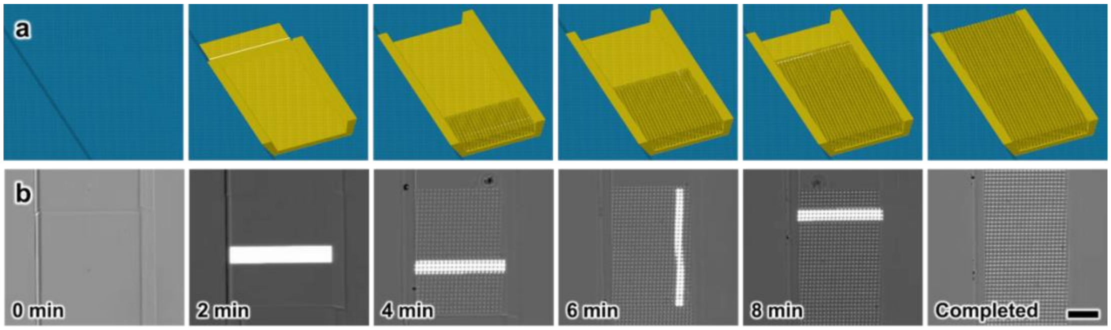

***Figure 4.2**: Fabrication results for DLW-based printing of a DLD array (800 µm in length) in an unenclosed COP microchannel (30 µm in height). (**a**) CAM simulations and (**b**) corresponding micrographs of the DLW printing process. Total print time ≈ 9 min; Scale bar =50µm.*

4.3.2. Experimental Characterization

Optical characterizations *via* scanning electron microscopy (SEM) were performed using a TM4000 Tabletop SEM (Hitachi, Tokyo, Japan). Microfluidic experiments were conducted using Fluigent Microfluidic Control System (MFCS) and flow rate platforms along with MAESFLO software (Fluigent, France). Two input solutions/suspensions were prepared for microfluidic testing: (*i*) a buffer solution comprised of DI water and 1% (v/v) Tween 20 (MilliporeSigma, St. Louis, USA), and (*ii*) a nanoparticle suspension comprised of DI water, 1% (v/v) Tween 20, and 0.01% (v/v) 860 nm fluorescent polystyrene particles (Thermo Fisher Scientific, Waltham, USA). The distinct fluidic samples were inputted into the microfluidic chip using fluorinated ethylene propylene tubing (Cole-Parmer, Vernon Hills, IL) and stainless-steel couplers (20 ga., Instech, Plymouth Meeting, PA). Fluorescence results were obtained *via* an inverted fluorescence microscope (Axio Observer.Z1, Zeiss, Germany) connected to a charge-coupled device (CCD) camera (Axiocam 503 Mono, Zeiss). To quantify the magnitude of lateral displacement, time-lapse fluorescence micrographs were processed using ImageJ (NIH, Bethesda, MD) to measure the mean-to-mean and peak-to-peak shifts in fluorescence intensity corresponding to the paths of the flowing suspended fluorescent particles: (*i*) directly prior to entering the DLD array, and (*ii*) directly after exiting the DLD array. Results in the text are presented as mean ± standard deviation.

4.4. Results and Discussion

4.4.1. Fabrication Results

CAM simulations and corresponding micrographs of the fabrication results for DLW-based printing of an 800-μm-long DLD array (comprised of four adjacently printed segments) directly inside of an unenclosed trapezoidal COP microchannel are presented in **Fig. 4.2a and b**, respectively. Among the geometric design variables that govern the size of particles that can be railed using DLD (eqn. 5), G is particularly susceptible to unintended variations due to DLW process conditions. Specifically, the size of the 2PP point (or "voxel") can be modified by adjusting either the laser power or the scanning speed. In this study, we set the scanning speed to remain constant at 10 mm/s (*i.e.*, to ensure consistency with prior work) and investigated the effects of varying laser power on *G*. Fabrication results for identically designed DLD arrays (G = 1 μm), but varying laser power revealed that lower laser powers produced smaller microposts, and thus, significantly larger *G* ($p < 0.01$) (**Fig. 4.3a**). For example, DLD arrays printed with laser powers of 22.5 mW, 25 mW, and 27.5 mW yielded average *G* of 1.51 ± 0.04 μm (**Fig. 4.3ai**), 1.21 ± 0.04 μm (**Fig. 4.3a*ii***), and 1.02 ± 0.05 μm (**Fig. 4.3a*iii***), respectively. These results suggest that a laser power of 27.5 mW produced DLD arrays that closely matched those of the original design. With respect to eqn. 5, we found that applying an incorrect laser power could lead to unintended alterations of D_C. By selecting a laser power corresponding to designed DLD geometric parameters, we observed that DLW could be effectively employed for DLD array manufacturing (*e.g.*, **Fig. 4.3b**).

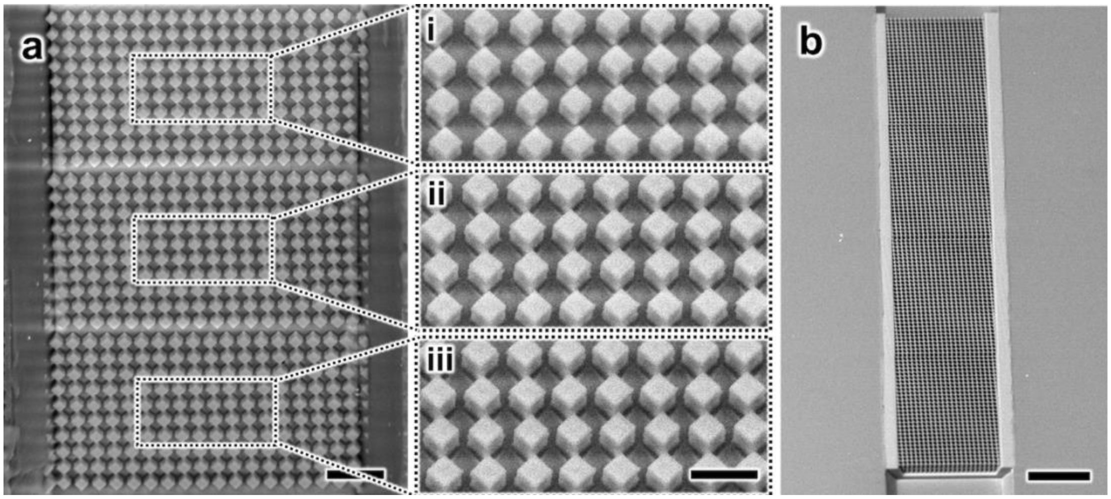

Figure 4.3: *SEM micrographs of DLW fabrication results. (**a**) Three identically designed DLD arrays printed using distinct laser powers of: (i) 22.5 mW, (ii) 25 mW, and (iii) 27.5 mW. Scale bars = 20 μm ; (i -iii) 10 μm . (**b**) SEM micrograph of a DLW-printed DLD array (800 μm in length) in an unenclosed COP microchannel (30 μm in height). Scale bar = 100 μm.*

4.4.2. DLD of Submicron Particles

To evaluate the core functionality of the DLW-printed DLD array, we performed continuous-flow microfluidic experiments with submicron fluorescent polystyrene particles (860 nm in diameter) and monitored particle displacement behaviors under fluorescence microscopy. For microfluidic testing, we fabricated a DLD system (180 μm in width; 500 μm in length) inside of a 200-μm-wide and 30-μm-high COP microchannel that comprised diamond-shaped microposts (3.5 μm×3.5 μm; $H = 22$ μm) arrayed with G of 2.5 μm and θ of 0.05 radians (**Fig. 4.4a**). These DLD array design parameters correspond to a D_C of 831 nm (eqn. 5), which satisfies the condition of being adequately smaller than the size of the target 860 nm particles. To prevent undesired particle-side wall interactions (*i.e.*, boundary effects) that can compromise DLD phenomena [145], we inputted a buffer solution distributed to both sides of the particle suspension channel, thereby hydrodynamically focusing the particle stream toward the center of the microchannel before entering the DLD array (**Fig. 4.4b**).

Fluorescence imaging during microfluidic experimentation revealed several key results. First, consistent with prior DLD works [171,179], we observed a degree of particle clogging at the entrance of the DLD array, as evident by the increased fluorescence intensities corresponding to the pathway of the particles flowing into the array (**Fig. 4.4c**). One potential basis for this result is the occurrence of particle agglomeration prior to microfluidic loading, resulting in adherent sets of particles with effective diameters that are larger than G. Although the surfactant, Tween 20, was included in the particle suspension (as well as the buffer solution) to preclude such issues, it is possible that some agglomeration persisted. The inclusion of additional particle filters prior to the DLD entryway could further limit such clogging events in the DLD array. Nonetheless, we found that suspended particles were able to bypass the initial clogging region, continuously flowing directly through this area and then the full DLD array (**Fig. 4.4c and d**). It is likely that the larger *H* contributed to the ability for mobile suspended particles to circumvent immobilized ones (*e.g.*, entering the DLD array at different heights to avoid the clogging events).

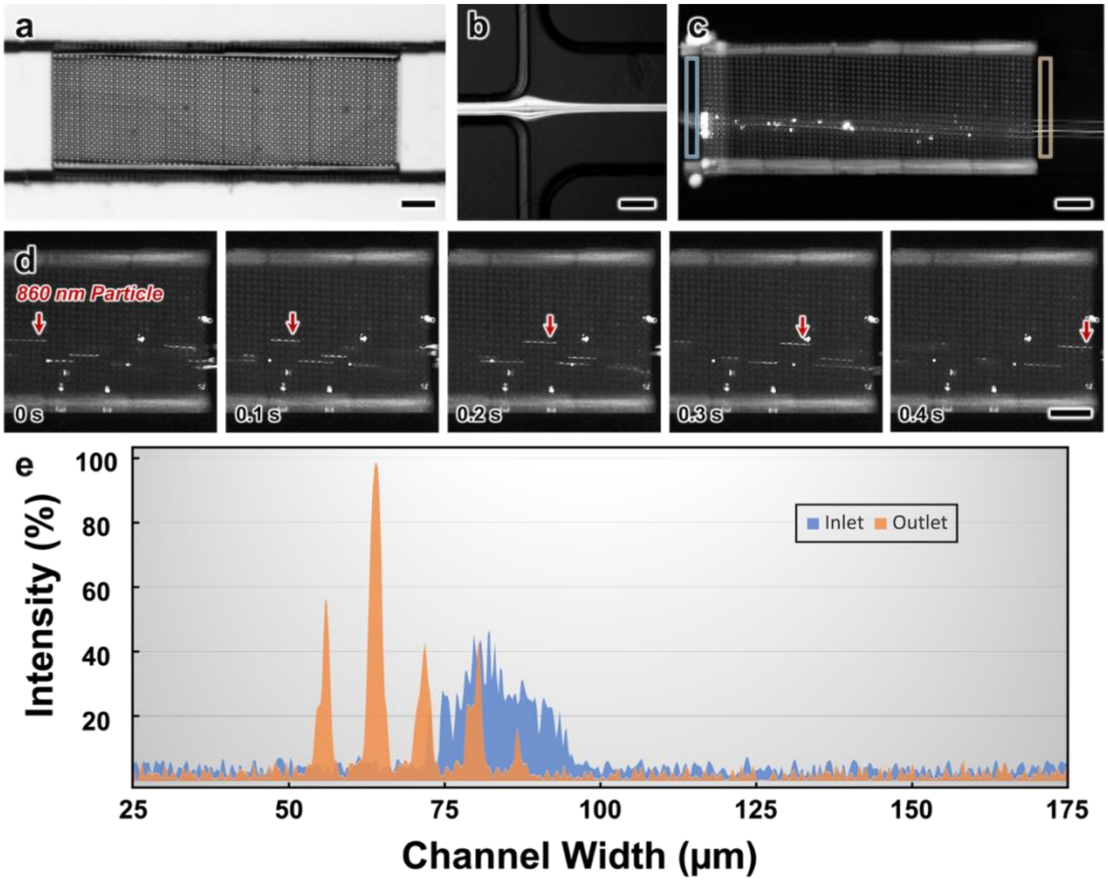

Figure 4.4 *Experimental results for microfluidic DLD of 860 nm fluorescent polystyrene particles. (**a**) Brightfield image of the DLW-printed DLD array. (**b**) Input microchannels corresponding to the particle suspension (middle) and buffer solution (top; bottom). (**c**) Fluorescence micrograph of particle streams through the DLD array. (**d**) Sequential fluorescence micrographs during particle transport through the DLD array. Scale bars =50μm. (**e**) Fluorescence intensity along the width of the microfluidic channel (as represented in part c) at the inlet (blue region) and outlet (orange region) of the DLD array.*

To evaluate the efficacy of the DLW-printed DLD array in guiding the target 860 nm particles away from their initial flow streams, we quantified the changes in fluorescence intensity characteristics (**Fig. 4.4e**) – a measure of the lateral shift of suspended particles during their transport through the microfluidic system – preceding and succeeding the DLD array. The quantified experimental results for particle flow behavior corresponding to the 500-μm-long DLD array revealed intensity shifts that suggest lateral displacement of 15.3 ± 8.6 μm (mean-to-mean) and 16.3 ± 8.9 μm (peak-to-peak). In combination, the experimental results demonstrate that the presented DLW-based approach is suitable for fabricating DLD arrays capable of processing submicron particles.

Chapter 5: Conclusion

5.1. Summery

Submicron additive manufacturing or "3D printing" approaches hold significant promise for the microfluidics community; however, without facile methods that allow for fluidic access to printed components (*i.e.*, macro-to-micro interfaces), the utility of such technologies remains limited. In **chapter 1** [43], we presented a sol-gel-based *is*DLW strategy that used PDMS-to-Glass microfluidic platforms. This strategy provided a fundamental foundation for a new class of microfluidic technologies that benefit from the 3D architectural control and submicron-scale resolution inherent to DLW, while bypassing the impediments that stem from facilitating the micro-to-macro interfaces that are critical to the system's utility. results from investigating the role of microchannel geometry in the sealing efficacy of *is*DLW-printed microstructures offers new means to inform the design of future *is*DLW-based microfluidic systems. Experiments with microfluidic barrier walls revealed increased structural sealing in sol-gel coated channels (up to 75 kPa), as well as established a correlation between microchannel height/profile and sealing integrity of the structures. Furthermore, we applied the same strategy to fabricate microfluidic diodes within 25-μm-high channels. After investigating the ideal operation of the diode using theoretical simulations, we presented results from microfluidic and optical experiments that characterize the fluidic performance of the diode and demonstrate its capability for effective unidirectional rectification of fluid flow.

Although our initial efforts demonstrated the potential of sol-gel-based *is*DLW strategies in PDMS platforms, the limited sealing performance as well as the drawbacks inherent to PDMS as a material (*e.g.,* gas permeability, poor compatibility with organic solvents, elasticity) rendered it poorly suited for *is*DLW of microfluidic systems. As a result, in **chapter 2** [45], we investigated the use of COP as an enabling material for *is*DLW due to a number of benefits that it shares with PDMS-on-Glass platforms (*e.g.*, capacity for micromolding and bonding, optical transparency), while overcoming several of the key limitations. The low gas permeability of COP allowed for microstructures to be *is*DLW-printed directly onto native COP surfaces, bypassing the need for extraneous microchannel processing steps, like the sol-gel coating step or post-process loading of silane-based glues through sacrificial channels [42]. The high resistance of COP to organic solvents facilitated the use of standard DLW developers (*e.g.*, PGMEA), thereby avoiding the need for undesired alterations to development protocols due to microchannel material incompatibility. In addition, the relatively high Young's modulus of COP (> 1 GPa) prevented pressure-based microchannel deformations that can exert undesired axial loading on microstructure-to-channel interfaces and lead to premature fluidic sealing failures.

To investigate the luminal adhesion of microfluidic structures printed using COP-based *is*DLW, we printed monolithic 10-μm-thick fluidic barrier structures inside of COP-COP microchannels of varying channel heights and cross-sectional profiles. For the trapezoidal and semi-elliptical channels in particular, burst-pressure experiments revealed consistent microfluidic sealing for input pressures up to 500 kPa independent of microchannel height (**Fig. 2.9**) – an order of magnitude improvement compared to the sol-gel coated PDMS (**Fig. 1.4**). Notably, the 500 kPa limit was a constraint of the experimental setup, and thus, it is possible that COP-based *is*DLW-printed barriers are able to withstand significantly higher pressures. We also fabricated interweaving microvessel-inspired architectures with inner diameters $< 10\ \mu$m to assess COP-based *is*DLW of 3D microfluidic systems in which the overall structure remains static during operation. To our knowledge, no prior report has demonstrated geometrically complex, biomimetic microfluidic structures at such scales with full micro-to-macro integration.

To provide insight into the use of COP-based *is*DLW for printing 3D microfluidic systems capable of dynamic operations *via* active control schemes, we designed and characterized a novel *NO* microfluidic transistor within 30-μm-tall COP-COP channels. For a sufficiently large P_G, the experimental results revealed full blocking of fluid flow through the microfluidic circuit element (**Fig. 2.16c**). As the operational performance of the microfluidic transistor is a function of the geometric design of the bellowed component, the concepts established here could be extended to enable 3D integrated microfluidic circuits comprising microfluidic transistors with differing bellow structures designed to activate at distinct P_G magnitudes – an approach that could overcome the “tyranny of microfluidic interconnects” at unprecedented length scales [66,106] At present, however, the reported microfluidic bellow-type *NO* transistor represents, to the best of our knowledge, the smallest 3D printed active microfluidic valving component reported in the literature [63–65].

In **chapter 3**, we leveraged the COP-based *is*DLW approach to present *NC* microfluidic transistors for which the gate activation dynamics can be tuned via geometric means [46]. After that, we demonstrated the integration of distinct *NC* transistors and soft microrobotic end effectors into a unified, hard-coded microfluidic system capable of executing multiple operational states in response to a single varying P_G input [47]. To our knowledge, this represents the first demonstration of 3D printed *NC* microfluidic transistors as well as the smallest *NC* microfluidic transistors (fabricated by any means) reported in the literature [106,132–137]. Both theoretical and experimental results revealed that the microfluidic transistor enabled active control of fluid flow across the source-to-drain microchannel through interactions between its two key dynamic components: (*i*) a bellow microstructure, and (*ii*) a free-floating sealing disc. Additionally, experimental results of a microfluidic system comprised of two sets of *NC* transistors and soft microgrippers revealed that microgripper deformation was prevented in the absence of a gate input; however, increasing the gate pressure to 300 kPa – at constant source pressure – induced actuation of one set of microgrippers, while a further increase to 400 kPa led to both sets of microgrippers actuating successfully. These results suggest that the presented *is*DLW-based strategy for manufacturing and integrating 3D microfluidic circuit elements and microrobotic end effectors could offer unique potential for emerging soft robotic applications.

In **chapter 4**, we explored the use of DLW for 3D printing DLD arrays at scales that enable hydrodynamic processing of submicron particles. To do so, we presented a manufacturing methodology that entailed DLW-printing DLD arrays in unenclosed COP microchannels and then fluidically sealing the devices *via* solvent-bonding processes. DLW fabrication results revealed a critical role for laser power in controlling *G*, with an approximately 22% increase in laser power resulting in a 48% decrease in *G* and a demonstrated resolvable *G* as low as 1.02 ± 0.05 μm. Microfluidic experimentation with 860 nm particles revealed successful lateral displacements quantified as 15.3 ± 8.6 μm (mean-to-mean) and 16.3 ± 8.9 μm (peak-to-peak) over a 500-μm-long DLW-printed DLD array. These results suggest that the presented strategy could be expanded to mixed suspensions with varying particle size ranges for sorting, isolation, and/or purification based DLD applications. Nonetheless, the present study serves as a fundamental proof of concept for the use of DLW for DLD array fabrication, while also marking the first report of a 3D printed DLD system capable of processing submicron-scale particles (to our knowledge). Extensions of this DLW-based strategy offer potential to advance numerous DLD-based biomedical research and applications that involve particles at smaller scales.

5.2. Future Directions

Building on the microfluidic technologies introduced in this dissertation. We can leverage the fabrication strategies developed here to explore various future directions. For the microfluidic circuitry work presented in **chapters 1-3**, all circuitry elements comprised a single, and relatively rigid photomaterial (i.e., IP-L 780); however, by employing multi-material DLW methodologies [90,91], material properties of the photoresist used can be tailored to compliment the functionality of the printed element.

For instance, a more flexible material can be used to print the bellowed microstructure in the transistors. Also, nanocomposite materials or smart materials like liquid crystalline elastomers (LCEs) can be used to enable the actuation of the printed elements in response to magnetic [180,181], thermal [182], and light-based [183,184] external stimuli. Additionally, even though the *is*DLW process used to fabricate these circuitry elements is based on printing inside of microchannels, the underlying concepts could be adapted to print microfluidic circuits that are integrated with externally printed mechano-fluidic soft robotic components [185], which can be particularly beneficial for medical device applications. Furthermore, the circuitry elements introduced here take advantage of the geometric versatility of DLW to improve on existing and functionally-analogues components (diodes, transistors, etc.). However, it might be favorable to leverage these advantages to design new circuitry elements that perform unique and/or consolidated fluidic functions.

Similar to the interweaving microvessel structures presented in **chapter 2,** the ability to recreate biomimetic microfluidic systems at physiologically accurate length scales provides a promising pathway not only to the manufacturing of biological phantoms (*e.g.*, with microvasculature) [186–188], but also toward cellularized *in vitro* platforms, such as for modeling components of the kidney, liver, and/or blood–brain barrier [25,87,88]. One possible direction that can be explored in this field involves benefiting from the material versatility of DLW to fabricate biological platforms comprised of different photomaterials. For example, by using flexible or optically transparent materials [189–191], it is possible to create platforms that model soft tissue components or facilitate applications that require cell imaging. Alternatively, another direction that can be investigated involves the use of objective lenses with lower magnification (e.g., 10x) to print these biomimetic platforms. Although this would cause a reduction in resolution, it will allow for rapid fabrication of larger scaled sub-millimeter structures (>100 μm) with a feature size that is still unmatched by other 3D printing technologies, which would be beneficial to model larger anatomical structures.

For the work presented in **chapter 4**. The DLD structure was designed to process 860 nm particles with G of 2.5 μm, θ of 0.05 radians, and H of 22 μm. However, these geometric parameters can be readily modified to tailor D_C (eqn. 5) for desired applications (*e.g.*, $D_C < 250$ nm *via* the lowest G demonstrated in this work and $\theta =$ 0.025 radians). Similarly, the methodology could also be extended to printed multi-tiered DLD systems with significantly larger H to yield high throughput processing [176] or gravity driven adaptations [192]. Also, as prior works have reported that modifying the shape of monolithic DLD posts can improve particle sorting efficiencies [178,193,194], the architectural versatility inherent to DLW could be leveraged to support 3D investigations of such concepts.

5.3. Scientific Contributions

In this section, we summarize the notable scientific contributions leveraged in each chapter of this dissertation.

In **Chapter 1**,

- We develop a sol-gel-based *is*DLW strategy for fabrication of microstructures within PDMS-on-Glass microfluidic platforms.
- We introduce a 25-μm-tall microfluidic diode – which is considered the smallest 3D printed component of its kind in the literature. We then demonstrate the diode's ability to unidirectionally rectify fluid flow in a PDMS microfluidic channel.

In **Chapter 2**,

- We report a novel strategy that utilizes COP as an enabling material for *is*DLW, with printed structure-to-channel microfluidic sealing results that represent an order-of-magnitude improvement over the state of the art.
- We fabricate interwoven bioinspired microvessels with inner diameters < 10 μm and wall thicknesses of 2 μm – the smallest reported in the literature to our knowledge – which successfully isolated distinct fluorescently labelled microfluidic flow streams.
- We demonstrate *NO*-type microfluidic transistors composed of flexible bellowed actuators (wall thicknesses $\approx$ 500 nm) inside of 30-μm-tall COP channels, which, to our knowledge, represent the smallest 3D printed fluidic valves reported in literature.

In **Chapter 3**,

- We introduce *NC*-type microfluidic transistors composed of flexible and free-floating actuators within 40-μm-tall COP channels. This represents the first demonstration of 3D printed microfluidic transistors capable of *NC* operations as well as the smallest *NC* transistor (fabricated by any means) reported in the literature.

- We illustrate a method to customize the gate activation properties of the transistors *via* simple, geometric means that doesn't require any change to the overall size of the structure.
- As an exemplar, we combine distinct microfluidic transistors with soft microrobotic grippers in an integrated microfluidic circuit and demonstrate the ability to achieve sequential gripper actuation by controlling a single gate pressure input.

In **Chapter 4**,

- We introduce a DLW-based process to additively manufacture DLD arrays inside of COP microchannels.
- We present the first demonstration of a 3D printed DLD array capable of successful processing of submicron-scale particles (860 nm).

In Combination, we believe that because the *is*DLW strategies presented here rely primarily on DLW-based fabrication, access to conventional clean room-based microfabrication facilities is not required for replicating and/or applying the methodologies described in this work. As a result, researchers with access to a DLW printer can readily disseminate electronic files of 3D models to enable on-site printing of new microfluidic systems, opening new pathways for investigators from diverse academic disciplines to leverage the benefits afforded by these scales for wide-ranging chemical, mechanical, and biological applications.

5.4. Journal Publications and Conferences Presentations

The work presented here resulted in **three first authored** journal publications, a **second authored** journal publication, and a **first authored** conference paper that was selected for an **oral presentation** at the international IEEE MEMS 2020 conference (~5-10% accepted out of ~700 abstracts). Below, is a list of these papers, in addition to multiple (first and co-authored) journal publications and conference presentations related to various AM technologies and processes that are outside the scope of this dissertation.

Journal Publications:

- **Abdullah T. Alsharhan**, Ruben Acevedo, Roseanne Warren, and Ryan D. Sochol, "3D Microfluidics via Cyclic Olefin Polymer-Based In Situ Direct Laser Writing," Lab on a Chip, Vol. 19, Issue 17, pp. 2799-2810, 2019. (Featured on the Front Cover of the journal issue).

- Andrew C. Lamont, **Abdullah T. Alsharhan**, and Ryan D. Sochol, "Geometric Determinants of In-Situ Direct Laser Writing," Scientific Reports, Nature Publishing Group, Vol. 9, pp. 394, 2019.

- **Abdullah T. Alsharhan**, Anthony J. Stair, Ruben Acevedo, Talha Razaulla, Roseanne Warren, and Ryan D. Sochol, "Direct Laser Writing for Deterministic Lateral Displacement of Submicron Particles," Journal of Microelectromechanical Systems, Vol. 29, Issue 5, pp. 906-911, 2020.

- **Abdullah T. Alsharhan**, Olivia Young, Xin Xu, Anthony J. Stair, and Ryan D. Sochol, "Integrated 3D Printed Microfluidic Circuitry and Soft Microrobotic Actuators via In Situ Direct Laser Writing," Journal of Micromechanics and Microengineering, 2021.

- Connor D. Armstrong, Noah Todd, **Abdullah T. Alsharhan**, David I. Bigio, and Ryan D. Sochol, "A 3D Printed Morphing Nozzle to Control Fiber Orientation During Composite Additive Manufacturing," Advanced Materials Technologies, Vol. 6, Issue 1, pp. 2000829, 2021. (Featured as a Frontispiece).

- Andrew C. Lamont, Michael A. Restaino, **Abdullah T. Alsharhan**, Zhuolin Liu, Daniel X. Hammer, Ryan D. Sochol, and Anant Agrawal*, “Direct Laser Writing of a Titanium Dioxide-Laden Retinal Cone Phantom for Adaptive Optics-Optical Coherence Tomography,” Optical Materials Express, Vol. 10, Issue 11, pp. 2757-2767, 2020.

Conference Presentations:

- (Oral) **Abdullah T. Alsharhan**, Anthony J. Stair, Ryan R. Utz, Andrew C. Lamont, Michael A. Restaino, Ruben Acevedo, and Ryan D. Sochol, “A 3D Nanoprinted Normally Closed Microfluidic Transistor,” Proceedings of the 33rd IEEE International Conference on Micro Electro Mechanical Systems (IEEE MEMS 2020), Vancouver, Canada. (Art in Microtechnology Award Finalist).

- (Oral) **Abdullah T. Alsharhan,** Timotei Centea, and Satyandra K. Gupta, "Enhancing Mechanical Properties of Thin-Walled Structures Using Non-Planar Extrusion Based Additive Manufacturing." Proceedings of the ASME 2017 12th International Manufacturing Science and Engineering Conference collocated with the JSME/ASME 2017 6th International Conference on Materials and Processing. Volume 2: Additive Manufacturing; Materials. Los Angeles, California, USA. June 4–8, 2017.

- (Oral) Michael Restaino, Noah Eckman, **Abdullah T. Alsharhan**, Andrew C. Lamont, Asha Hall, and Ryan D. Sochol, “Direct Laser Writing of Three-Dimensional Graphene-Laden Microstructures Inside Enclosed Microfluidic Channels,” Proceedings of the 23rd International Conference on Miniaturized Systems for Chemistry and Life Sciences (µTAS 2019), Basel, Switzerland.

- Andrew C. Lamont, Michael Restaino, **Abdullah T. Alsharhan**, Zhoulin Liu, Daniel X. Hammer, Anant Agrawal, and Ryan D. Sochol, “Direct Laser Writing of Titanium Dioxide-Laden Retinal Cone Phantoms” Proceedings of the 33rd IEEE International Conference on Micro Electro Mechanical Systems (IEEE MEMS 2020), Vancouver, Canada.

Bibliography

1. S. V. Murphy and A. Atala, "3D bioprinting of tissues and organs," Nat. Biotechnol. **32**, 773–785 (2014).
2. N. Bhattacharjee, A. Urrios, S. Kang, and A. Folch, "The upcoming 3D-printing revolution in microfluidics," Lab. Chip **16**, 1720–1742 (2016).
3. A. D. Valentine, T. A. Busbee, J. W. Boley, J. R. Raney, A. Chortos, A. Kotikian, J. D. Berrigan, M. F. Durstock, and J. A. Lewis, "Hybrid 3D Printing of Soft Electronics," Adv. Mater. **29**, 1703817 (2017).
4. H.-W. Kang, S. J. Lee, I. K. Ko, C. Kengla, J. J. Yoo, and A. Atala, "A 3D bioprinting system to produce human-scale tissue constructs with structural integrity," Nat. Biotechnol. **34**, 312–319 (2016).
5. M. A. Skylar-Scott, S. Gunasekaran, and J. A. Lewis, "Laser-assisted direct ink writing of planar and 3D metal architectures," Proc. Natl. Acad. Sci. **113**, 6137–6142 (2016).
6. D. B. Kolesky, R. L. Truby, A. S. Gladman, T. A. Busbee, K. A. Homan, and J. A. Lewis, "3D Bioprinting of Vascularized, Heterogeneous Cell-Laden Tissue Constructs," Adv. Mater. **26**, 3124–3130 (2014).
7. A. K. Au, W. Huynh, L. F. Horowitz, and A. Folch, "3D-Printed Microfluidics," Angew. Chem. Int. Ed. **55**, 3862–3881 (2016).
8. Y. Zhang, F. Zhang, Z. Yan, Q. Ma, X. Li, Y. Huang, and J. A. Rogers, "Printing, folding and assembly methods for forming 3D mesostructures in advanced materials," Nat. Rev. Mater. **2**, (2017).
9. F. Kotz, K. Arnold, W. Bauer, D. Schild, N. Keller, K. Sachsenheimer, T. M. Nargang, C. Richter, D. Helmer, and B. E. Rapp, "Three-dimensional printing of transparent fused silica glass," Nature **544**, 337–339 (2017).
10. C. C. J. Alcântara, F. C. Landers, S. Kim, C. De Marco, D. Ahmed, B. J. Nelson, and S. Pané, "Mechanically interlocked 3D multi-material micromachines," Nat. Commun. **11**, 5957 (2020).
11. L. Jonušauskas, T. Baravykas, D. Andrijec, T. Gadišauskas, and V. Purlys, "Stitchless support-free 3D printing of free-form micromechanical structures with feature size on-demand," Sci. Rep. **9**, 17533 (2019).
12. T. Gissibl, S. Thiele, A. Herkommer, and H. Giessen, "Two-photon direct laser writing of ultracompact multi-lens objectives," Nat. Photonics **10**, 554–560 (2016).
13. P.-I. Dietrich, M. Blaicher, I. Reuter, M. Billah, T. Hoose, A. Hofmann, C. Caer, R. Dangel, B. Offrein, U. Troppenz, M. Moehrle, W. Freude, and C. Koos, "In situ 3D nanoprinting of free-form coupling elements for hybrid photonic integration," Nat. Photonics **12**, 241–247 (2018).
14. J. Fischer and M. Wegener, "Three-dimensional optical laser lithography beyond the diffraction limit," Laser Photonics Rev. **7**, 22–44 (2013).
15. X. Zhou, Y. Hou, and J. Lin, "A review on the processing accuracy of two-photon polymerization," AIP Adv. **5**, 030701 (2015).
16. A. E. Goodling, S. Nagelberg, B. Kaehr, C. H. Meredith, S. I. Cheon, A. P. Saunders, M. Kolle, and L. D. Zarzar, "Colouration by total internal reflection and interference at microscale concave interfaces," Nature **566**, 523 (2019).

17. M. Hippler, E. Blasco, J. Qu, M. Tanaka, C. Barner-Kowollik, M. Wegener, and M. Bastmeyer, "Controlling the shape of 3D microstructures by temperature and light," Nat. Commun. **10**, 232 (2019).
18. D. Nishiguchi, I. S. Aranson, A. Snezhko, and A. Sokolov, "Engineering bacterial vortex lattice via direct laser lithography," Nat. Commun. **9**, 4486 (2018).
19. E. Montinaro, M. Grisi, M. Letizia, L. Pethö, M. Gijs, R. Guidetti, J. Michler, J. Brugger, and G. Boero, "3D printed microchannels for sub-nL NMR spectroscopy," PloS One **13**, e0192780 (2018).
20. R. D. Sochol, E. Sweet, C. C. Glick, S.-Y. Wu, C. Yang, M. Restaino, and L. Lin, "3D printed microfluidics and microelectronics," Microelectron. Eng. **189**, 52–68 (2018).
21. M. R. Gullo, S. Takeuchi, and O. Paul, "Multicellular Biohybrid Materials: Probing the Interplay of Cells of Different Types Precisely Positioned and Constrained on 3D Wireframe-Like Microstructures," Adv. Healthc. Mater. **6**, 1601053 (2017).
22. C. Barner-Kowollik, M. Bastmeyer, E. Blasco, G. Delaittre, P. Müller, B. Richter, and M. Wegener, "3D Laser Micro- and Nanoprinting: Challenges for Chemistry," Angew. Chem. Int. Ed. **56**, 15828–15845 (2017).
23. A. Vyatskikh, S. Delalande, A. Kudo, X. Zhang, C. M. Portela, and J. R. Greer, "Additive manufacturing of 3D nano-architected metals," Nat. Commun. **9**, 593 (2018).
24. E. K. Sackmann, A. L. Fulton, and D. J. Beebe, "The present and future role of microfluidics in biomedical research," Nature **507**, 181–189 (2014).
25. A. Marino, O. Tricinci, M. Battaglini, C. Filippeschi, V. Mattoli, E. Sinibaldi, and G. Ciofani, "A 3D Real-Scale, Biomimetic, and Biohybrid Model of the Blood-Brain Barrier Fabricated through Two-Photon Lithography," Small **14**, 1702959 (2018).
26. J. Wang, Y. He, H. Xia, L.-G. Niu, R. Zhang, Q.-D. Chen, Y.-L. Zhang, Y.-F. Li, S.-J. Zeng, J.-H. Qin, and others, "Embellishment of microfluidic devices via femtosecond laser micronanofabrication for chip functionalization," Lab. Chip **10**, 1993–1996 (2010).
27. T. W. Lim, Y. Son, Y. J. Jeong, D.-Y. Yang, H.-J. Kong, K.-S. Lee, and D.-P. Kim, "Three-dimensionally crossing manifold micro-mixer for fast mixing in a short channel length," Lab. Chip **11**, 100–103 (2011).
28. Y. He, B.-L. Huang, D.-X. Lu, J. Zhao, B.-B. Xu, R. Zhang, X.-F. Lin, Q.-D. Chen, J. Wang, Y.-L. Zhang, and others, "“Overpass” at the junction of a crossed microchannel: An enabler for 3D microfluidic chips," Lab. Chip **12**, 3866–3869 (2012).
29. M. H. Olsen, G. M. Hjortø, M. Hansen, Ö. Met, I. M. Svane, and N. B. Larsen, "In-chip fabrication of free-form 3D constructs for directed cell migration analysis," Lab. Chip **13**, 4800 (2013).
30. D. Wu, J. Xu, L.-G. Niu, S.-Z. Wu, K. Midorikawa, and K. Sugioka, "In-channel integration of designable microoptical devices using flat scaffold-supported femtosecond-laser microfabrication for coupling-free optofluidic cell counting," Light Sci. Appl. **4**, e228–e228 (2015).

31. K. Sugioka, J. Xu, D. Wu, Y. Hanada, Z. Wang, Y. Cheng, and K. Midorikawa, "Femtosecond laser 3D micromachining: a powerful tool for the fabrication of microfluidic, optofluidic, and electrofluidic devices based on glass," Lab Chip **14**, 3447–3458 (2014).
32. D. Wu, S.-Z. Wu, J. Xu, L.-G. Niu, K. Midorikawa, and K. Sugioka, "Hybrid femtosecond laser microfabrication to achieve true 3D glass/polymer composite biochips with multiscale features and high performance: the concept of ship-in-a-bottle biochip: Hybrid femtosecond laser microfabrication for true 3D ship-in-a-bottle biochip," Laser Photonics Rev. **8**, 458–467 (2014).
33. M. R. Lee, H. K. Lee, Y. Yang, C. S. L. Koh, C. L. Lay, Y. H. Lee, I. Y. Phang, and X. Y. Ling, "Direct Metal Writing and Precise Positioning of Gold Nanoparticles within Microfluidic Channels for SERS Sensing of Gaseous Analytes," ACS Appl. Mater. Interfaces **9**, 39584–39593 (2017).
34. L. Amato, Y. Gu, N. Bellini, S. M. Eaton, G. Cerullo, and R. Osellame, "Integrated three-dimensional filter separates nanoscale from microscale elements in a microfluidic chip," Lab. Chip **12**, 1135 (2012).
35. H. Wang, Y.-L. Zhang, W. Wang, H. Ding, and H.-B. Sun, "On-chip laser processing for the development of multifunctional microfluidic chips," Laser Photonics Rev. **11**, 1600116 (2017).
36. M. Iosin, T. Scheul, C. Nizak, O. Stephan, S. Astilean, and P. Baldeck, "Laser microstructuration of three-dimensional enzyme reactors in microfluidic channels," Microfluid. Nanofluidics **10**, 685–690 (2011).
37. Y.-J. Liu, J.-Y. Yang, Y.-M. Nie, C.-H. Lu, E. D. Huang, C.-S. Shin, P. Baldeck, and C.-L. Lin, "A simple and direct reading flow meter fabricated by two-photon polymerization for microfluidic channel," Microfluid. Nanofluidics **18**, 427–431 (2015).
38. D. Dendukuri, D. C. Pregibon, J. Collins, T. A. Hatton, and P. S. Doyle, "Continuous-flow lithography for high-throughput microparticle synthesis," Nat. Mater. **5**, 365–369 (2006).
39. S. E. Chung, W. Park, S. Shin, S. A. Lee, and S. Kwon, "Guided and fluidic self-assembly of microstructures using railed microfluidic channels," Nat. Mater. **7**, 581–587 (2008).
40. J. R. Tumbleston, D. Shirvanyants, N. Ermoshkin, R. Janusziewicz, A. R. Johnson, D. Kelly, K. Chen, R. Pinschmidt, J. P. Rolland, A. Ermoshkin, and others, "Continuous liquid interface production of 3D objects," Science aaa2397 (2015).
41. A. C. Lamont, E. C. Reggia, and R. D. Sochol, "In situ nano 3D printing of a microfluidic diode," in (IEEE, 2017), pp. 1304–1307.
42. J. Lölsberg, J. Linkhorst, A. Cinar, A. Jans, A. J. Kuehne, and M. Wessling, "3D Nanofabrication inside rapid prototyped microfluidic channels showcased by wet-spinning of single micrometre fibres," Lab. Chip **18**, 1341–1348 (2018).
43. A. C. Lamont, A. T. Alsharhan, and R. D. Sochol, "Geometric Determinants of In-Situ Direct Laser Writing," Sci. Rep. **9**, 394 (2019).
44. J. N. Lee, C. Park, and G. M. Whitesides, "Solvent compatibility of poly (dimethylsiloxane)-based microfluidic devices," Anal. Chem. **75**, 6544–6554 (2003).

45. A. T. Alsharhan, R. Acevedo, R. Warren, and R. D. Sochol, "3D microfluidics *via* cyclic olefin polymer-based *in situ* direct laser writing," Lab. Chip **19**, 2799–2810 (2019).
46. A. T. Alsharhan, A. J. Stair, R. R. Utz, A. C. Lamont, M. A. Restaino, R. Acevedo, and R. D. Sochol, "A 3D Nanoprinted Normally Closed Microfluidic Transistor," in *2020 IEEE 33rd International Conference on Micro Electro Mechanical Systems (MEMS)* (2020), pp. 131–134.
47. A. Alsharhan, O. M. Young, X. Xu, A. J. Stair, and R. D. Sochol, "Integrated 3D Printed Microfluidic Circuitry and Soft Microrobotic Actuators via In Situ Direct Laser Writing," J. Micromechanics Microengineering (2021).
48. A. T. Alsharhan, A. J. Stair, R. Acevedo, T. Razaulla, R. Warren, and R. D. Sochol, "Direct Laser Writing for Deterministic Lateral Displacement of Submicron Particles," J. Microelectromechanical Syst. **29**, 906–911 (2020).
49. S. Yadavali, H.-H. Jeong, D. Lee, and D. Issadore, "Silicon and glass very large scale microfluidic droplet integration for terascale generation of polymer microparticles," Nat. Commun. **9**, 1222 (2018).
50. N. Cho, S. Goodwin, J. Budassi, K. Zhu, W. McCombie, and others, "Fragmentation of Surface Adsorbed and Aligned DNA Molecules using Soft Lithography for Next-Generation Sequencing," J Biosens Bioelectro **8**, (2017).
51. K. Mogi, Y. Sugii, T. Yamamoto, and T. Fujii, "Rapid fabrication technique of nano/microfluidic device with high mechanical stability utilizing two-step soft lithography," Sens. Actuators B Chem. **201**, 407–412 (2014).
52. J. H. L. Beal, A. Bubendorfer, T. Kemmitt, I. Hoek, and W. Mike Arnold, "A rapid, inexpensive surface treatment for enhanced functionality of polydimethylsiloxane microfluidic channels," Biomicrofluidics **6**, 036503 (2012).
53. G. Kumi, C. O. Yanez, K. D. Belfield, and J. T. Fourkas, "High-speed multiphoton absorption polymerization: fabrication of microfluidic channels with arbitrary cross-sections and high aspect ratios," Lab. Chip **10**, 1057 (2010).
54. C. N. LaFratta, O. Simoska, I. Pelse, S. Weng, and M. Ingram, "A convenient direct laser writing system for the creation of microfluidic masters," Microfluid. Nanofluidics **19**, 419–426 (2015).
55. D. Barata, E. Provaggi, C. van Blitterswijk, and P. Habibovic, "Development of a microfluidic platform integrating high-resolution microstructured biomaterials to study cell–material interactions," Lab. Chip **17**, 4134–4147 (2017).
56. C. Bleilevens, J. Lölsberg, A. Cinar, M. Knoben, O. Grottke, R. Rossaint, and M. Wessling, "Microfluidic cell sorting: Towards improved biocompatibility of extracorporeal lung assist devices," Sci. Rep. **8**, 8031 (2018).
57. D. Wu, B. Zhao, Z. Dai, J. Qin, and B. Lin, "Grafting epoxy-modified hydrophilic polymers onto poly(dimethylsiloxane) microfluidic chip to resist nonspecific protein adsorption," Lab. Chip **6**, 942 (2006).
58. A.-J. Wang, J.-J. Feng, and J. Fan, "Covalent modified hydrophilic polymer brushes onto poly(dimethylsiloxane) microchannel surface for electrophoresis separation of amino acids," J. Chromatogr. A **1192**, 173–179 (2008).

59. J. Bu, Y. J. Kim, Y.-T. Kang, T. H. Lee, J. Kim, Y.-H. Cho, and S.-W. Han, "Polyester fabric sheet layers functionalized with graphene oxide for sensitive isolation of circulating tumor cells," Biomaterials **125**, 1–11 (2017).
60. R. D. Sochol, S. Li, L. P. Lee, and L. Lin, "Continuous flow multi-stage microfluidic reactors via hydrodynamic microparticle railing," Lab. Chip **12**, 4168–4177 (2012).
61. J. G. Dawson, D. C. Hesley, N. Katagiri, C. P. Nguyen, S. A. Mannuel, T. G. Wun, A. B. Chow, N. R. Gupta, J. V. Bonventre, and R. D. Sochol, "Bioinspired vascular structures via 3d printing and suspended microfluidics," in *2017 IEEE 30th International Conference on Micro Electro Mechanical Systems (MEMS)* (IEEE, 2017), pp. 426–429.
62. K. C. Bhargava, B. Thompson, and N. Malmstadt, "Discrete elements for 3D microfluidics," Proc. Natl. Acad. Sci. **111**, 15013–15018 (2014).
63. A. K. Au, N. Bhattacharjee, L. F. Horowitz, T. C. Chang, and A. Folch, "3D-printed microfluidic automation," Lab. Chip **15**, 1934–1941 (2015).
64. H. Gong, A. T. Woolley, and G. P. Nordin, "High density 3D printed microfluidic valves, pumps, and multiplexers," Lab. Chip **16**, 2450–2458 (2016).
65. Y.-S. Lee, N. Bhattacharjee, and A. Folch, "3D-printed Quake-style microvalves and micropumps," Lab. Chip **18**, 1207–1214 (2018).
66. R. D. Sochol, E. Sweet, C. C. Glick, S. Venkatesh, A. Avetisyan, K. F. Ekman, A. Raulinaitis, A. Tsai, A. Wienkers, K. Korner, K. Hanson, A. Long, B. J. Hightower, G. Slatton, D. C. Burnett, T. L. Massey, K. Iwai, L. P. Lee, K. S. J. Pister, and L. Lin, "3D printed microfluidic circuitry via multijet-based additive manufacturing," Lab. Chip **16**, 668–678 (2016).
67. E. D. Lemma, F. Rizzi, T. Dattoma, B. Spagnolo, L. Sileo, A. Qualtieri, M. D. Vittorio, and F. Pisanello, "Mechanical Properties Tunability of Three-Dimensional Polymeric Structures in Two-Photon Lithography," IEEE Trans. Nanotechnol. **16**, (2017).
68. R. D. Sochol, A. Lu, J. Lei, K. Iwai, L. P. Lee, and L. Lin, "Microfluidic bead-based diodes with targeted circular microchannels for low Reynolds number applications," Lab. Chip **14**, 1585–1594 (2014).
69. M. L. Adams, M. L. Johnston, A. Scherer, and S. R. Quake, "Polydimethylsiloxane based microfluidic diode," J. Micromechanics Microengineering **15**, 1517–1521 (2005).
70. D. C. Leslie, C. J. Easley, E. Seker, J. M. Karlinsey, M. Utz, M. R. Begley, and J. P. Landers, "Frequency-specific flow control in microfluidic circuits with passive elastomeric features," Nat. Phys. **5**, 231?235 (2009).
71. B. Mosadegh, C.-H. Kuo, Y.-C. Tung, Y.-S. Torisawa, T. Bersano, H. Tavana, and S. Takayama, "Integrated Elastomeric Components for Autonomous Regulation of Sequential and Oscillatory Flow Switching in Microfluidic Devices," Nat. Phys. **6**, 433–437 (2010).
72. M. Wehner, R. L. Truby, D. J. Fitzgerald, B. Mosadegh, G. M. Whitesides, J. A. Lewis, and R. J. Wood, "An integrated design and fabrication strategy for entirely soft, autonomous robots," Nature **536**, 451–455 (2016).

73. M. Denz, G. Brehm, C. Y. Hémonnot, H. Spears, A. Wittmeier, C. Cassini, O. Saldanha, E. Perego, A. Diaz, M. Burghammer, and others, "Cyclic olefin copolymer as an X-ray compatible material for microfluidic devices," Lab. Chip **18**, 171–178 (2018).
74. J. S. Jeon, S. Chung, R. D. Kamm, and J. L. Charest, "Hot embossing for fabrication of a microfluidic 3D cell culture platform," Biomed. Microdevices **13**, 325–333 (2011).
75. R. K. Jena, C. Y. Yue, and Y. C. Lam, "Micro fabrication of cyclic olefin copolymer (COC) based microfluidic devices," Microsyst. Technol. **18**, 159–166 (2012).
76. C.-Y. Yen, M.-C. Chang, Z.-F. Shih, Y.-H. Lien, and C.-W. Tsao, "Cyclic Block Copolymer Microchannel Fabrication and Sealing for Microfluidics Applications," Inventions **3**, 49 (2018).
77. S. A. Aghvami, A. Opathalage, Z. K. Zhang, M. Ludwig, M. Heymann, M. Norton, N. Wilkins, and S. Fraden, "Rapid prototyping of cyclic olefin copolymer (COC) microfluidic devices," Sens. Actuators B Chem. **247**, 940–949 (2017).
78. O. Rahmanian and D. L. DeVoe, "Pen microfluidics: rapid desktop manufacturing of sealed thermoplastic microchannels," Lab. Chip **13**, 1102–1108 (2013).
79. M. Berenguel-Alonso, M. Sabés-Alsina, R. Morató, O. Ymbern, L. Rodríguez-Vázquez, O. Talló-Parra, J. Alonso-Chamarro, M. Puyol, and M. López-Béjar, "Rapid Prototyping of a Cyclic Olefin Copolymer Microfluidic Device for Automated Oocyte Culturing," SLAS Technol. Transl. Life Sci. Innov. **22**, 507–517 (2017).
80. S. Liu, Y. Fan, K. Gao, and Y. Zhang, "Fabrication of Cyclo-olefin polymer-based microfluidic devices using CO2 laser ablation," Mater. Res. Express **5**, 095305 (2018).
81. N. Keller, T. M. Nargang, M. Runck, F. Kotz, A. Striegel, K. Sachsenheimer, D. Klemm, K. Länge, M. Worgull, C. Richter, D. Helmer, and B. E. Rapp, "Tacky cyclic olefin copolymer: a biocompatible bonding technique for the fabrication of microfluidic channels in COC," Lab. Chip **16**, 1561–1564 (2016).
82. P. Ganser, C. Baum, D. Chargin, A. F. Sauer-Budge, and A. Sharon, "A practical approach for the optimization of channel integrity in the sealing of shallow microfluidic devices made from cyclic olefin polymer," Biomed. Microdevices **20**, 24 (2018).
83. C.-W. Tsao and D. L. DeVoe, "Bonding of thermoplastic polymer microfluidics," Microfluid. Nanofluidics **6**, 1–16 (2009).
84. J. Greener, W. Li, J. Ren, D. Voicu, V. Pakharenko, T. Tang, and E. Kumacheva, "Rapid, cost-efficient fabrication of microfluidic reactors in thermoplastic polymers by combining photolithography and hot embossing," Lab Chip **10**, 522–524 (2010).
85. J. Steigert, S. Haeberle, T. Brenner, C. Müller, C. Steinert, P. Koltay, N. Gottschlich, H. Reinecke, J. Rühe, R. Zengerle, and others, "Rapid prototyping of microfluidic chips in COC," J. Micromechanics Microengineering **17**, 333 (2007).

86. T. Kohara, "Development of new cyclic olefin polymers for optical uses," in *Macromolecular Symposia* (Wiley Online Library, 1996), Vol. 101, pp. 571–579.
87. B. Grigoryan, S. J. Paulsen, D. C. Corbett, D. W. Sazer, C. L. Fortin, A. J. Zaita, P. T. Greenfield, N. J. Calafat, J. P. Gounley, A. H. Ta, and others, "Multivascular networks and functional intravascular topologies within biocompatible hydrogels," Science **364**, 458–464 (2019).
88. N. Y. Lin, K. A. Homan, S. S. Robinson, D. B. Kolesky, N. Duarte, A. Moisan, and J. A. Lewis, "Renal reabsorption in 3D vascularized proximal tubule models," Proc. Natl. Acad. Sci. **116**, 5399–5404 (2019).
89. D. Lei, Y. Yang, Z. Liu, B. Yang, W. Gong, S. Chen, S. Wang, L. Sun, B. Song, H. Xuan, and others, "3D printing of biomimetic vasculature for tissue regeneration," Mater. Horiz. (2019).
90. A. C. Lamont, M. A. Restaino, M. J. Kim, and R. D. Sochol, "A Facile Multi-Material Direct Laser Writing Strategy," Lab. Chip (2019).
91. F. Mayer, S. Richter, J. Westhauser, E. Blasco, C. Barner-Kowollik, and M. Wegener, "Multimaterial 3D laser microprinting using an integrated microfluidic system," Sci. Adv. **5**, eaau9160 (2019).
92. A. Jönsson and M. Hermann, *Static Characteristics of Flexible Bellows* (1997).
93. Q. Zhang, M. Zhang, L. Djeghlaf, J. Bataille, J. Gamby, A.-M. Haghiri-Gosnet, and A. Pallandre, "Logic digital fluidic in miniaturized functional devices: Perspective to the next generation of microfluidic lab-on-chips," ELECTROPHORESIS **38**, 953–976 (2017).
94. K. S. Elvira, X. C. i Solvas, R. C. R. Wootton, and A. J. deMello, "The past, present and potential for microfluidic reactor technology in chemical synthesis," Nat. Chem. **5**, 905–915 (2013).
95. F. J. H. Hol and C. Dekker, "Zooming in to see the bigger picture: Microfluidic and nanofabrication tools to study bacteria," Science **346**, (2014).
96. S. F. Berlanda, M. Breitfeld, C. L. Dietsche, and P. S. Dittrich, "Recent Advances in Microfluidic Technology for Bioanalysis and Diagnostics," Anal. Chem. (2020).
97. H. T. G. van Lintel, F. C. M. van De Pol, and S. Bouwstra, "A piezoelectric micropump based on micromachining of silicon," Sens. Actuators **15**, 153–167 (1988).
98. D. J. Harrison, K. Fluri, K. Seiler, Z. Fan, C. S. Effenhauser, and A. Manz, "Micromachining a Miniaturized Capillary Electrophoresis-Based Chemical Analysis System on a Chip," Science **261**, 895–897 (1993).
99. G. M. Whitesides, "The origins and the future of microfluidics," Nature **442**, 368–373 (2006).
100. G. D. Aumiller, E. A. Chandross, W. J. Tomlinson, and H. P. Weber, "Submicrometer resolution replication of relief patterns for integrated optics," J. Appl. Phys. **45**, 4557–4562 (1974).
101. D. C. Duffy, J. C. McDonald, O. J. Schueller, and G. M. Whitesides, "Rapid Prototyping of Microfluidic Systems in Poly(dimethylsiloxane)," Anal. Chem. **70**, 4974–4984 (1998).

102. M. A. Unger, H. P. Chou, T. Thorsen, A. Scherer, and S. R. Quake, "Monolithic Microfabricated Valves and Pumps by Multilayer Soft Lithography," Science **288**, 113–6 (2000).
103. T. Thorsen, S. J. Maerkl, and S. R. Quake, "Microfluidic Large-Scale Integration," Science **298**, 580–584 (2002).
104. C.-C. Lee, G. Sui, A. Elizarov, C. J. Shu, Y.-S. Shin, A. N. Dooley, J. Huang, A. Daridon, P. Wyatt, D. Stout, H. C. Kolb, O. N. Witte, N. Satyamurthy, J. R. Heath, M. E. Phelps, S. R. Quake, and H.-R. Tseng, "Multistep Synthesis of a Radiolabeled Imaging Probe Using Integrated Microfluidics," Science **310**, 1793–1796 (2005).
105. F. K. Balagaddé, L. You, C. L. Hansen, F. H. Arnold, and S. R. Quake, "Long-Term Monitoring of Bacteria Undergoing Programmed Population Control in a Microchemostat," Science **309**, 137–140 (2005).
106. B. Mosadegh, T. Bersano-Begey, J. Y. Park, M. A. Burns, and S. Takayama, "Next-generation integrated microfluidic circuits," Lab. Chip **11**, 2813–2818 (2011).
107. P. Frank, D. Gräfe, C. Probst, S. Haefner, M. Elstner, D. Appelhans, D. Kohlheyer, B. Voit, and A. Richter, "Autonomous Integrated Microfluidic Circuits for Chip-Level Flow Control Utilizing Chemofluidic Transistors," Adv. Funct. Mater. **27**, 1700430 (2017).
108. N. Vourdas, D. C. Moschou, K. A. Papadopoulos, D. Davazoglou, and V. N. Stathopoulos, "A new microfluidic pressure-controlled Field Effect Transistor (pFET) in digital fluidic switch operation mode," Microelectron. Eng. **190**, 28–32 (2018).
109. J. A. Weaver, J. Melin, D. Stark, S. R. Quake, and M. A. Horowitz, "Static control logic for microfluidic devices using pressure-gain valves," Nat. Phys. **6**, 218–223 (2010).
110. Z. Li and S.-J. Kim, "Autonomous microfluidic actuators for periodic sequential flow generation," Sci. Adv. **5**, eaat3080 (2019).
111. P. Rothemund, A. Ainla, L. Belding, D. J. Preston, S. Kurihara, Z. Suo, and G. M. Whitesides, "A soft, bistable valve for autonomous control of soft actuators," Sci. Robot. **3**, (2018).
112. N. Napp, B. Araki, M. T. Tolley, R. Nagpal, and R. J. Wood, "Simple passive valves for addressable pneumatic actuation," in *2014 IEEE International Conference on Robotics and Automation (ICRA)* (2014), pp. 1440–1445.
113. K. Iwai, K. C. Shih, X. Lin, T. A. Brubaker, R. D. Sochol, and L. Lin, "Finger-powered microfluidic systems using multilayer soft lithography and injection molding processes," Lab. Chip **14**, 3790 (2014).
114. R. D. Sochol, B. P. Casavant, M. E. Dueck, L. P. Lee, and L. Lin, "A dynamic bead-based microarray for parallel DNA detection," J. Micromechanics Microengineering **21**, 054019 (2011).
115. A. V. Nielsen, M. J. Beauchamp, G. P. Nordin, and A. T. Woolley, "3D Printed Microfluidics," Annu. Rev. Anal. Chem. **13**, 45–65 (2020).
116. R. Su, J. Wen, Q. Su, M. S. Wiederoder, S. J. Koester, J. R. Uzarski, and M. C. McAlpine, "3D printed self-supporting elastomeric structures for multifunctional microfluidics," Sci. Adv. **6**, eabc9846 (2020).

117. H. Gong, A. T. Woolley, and G. P. Nordin, "3D printed selectable dilution mixer pumps," Biomicrofluidics **13**, 014106 (2019).
118. C. I. Rogers, K. Qaderi, A. T. Woolley, and G. P. Nordin, "3D printed microfluidic devices with integrated valves," Biomicrofluidics **9**, 016501 (2015).
119. D. Hee Kang, N. Kyong Kim, S.-W. Park, W. Lee, and H. Wook Kang, "A microfluidic circuit consisting of individualized components with a 3D slope valve for automation of sequential liquid control," Lab. Chip **20**, 4433–4441 (2020).
120. E. Sweet, R. Mehta, Y. Xu, R. Jew, R. Lin, and L. Lin, "Finger-powered fluidic actuation and mixing via MultiJet 3D printing," Lab. Chip **20**, 3375–3385 (2020).
121. E. H. Childs, A. V. Latchman, A. C. Lamont, J. D. Hubbard, and R. D. Sochol, "Additive Assembly for PolyJet-Based Multi-Material 3D Printed Microfluidics," J. Microelectromechanical Syst. **29**, 1094–1096 (2020).
122. V. Hahn, P. Kiefer, T. Frenzel, J. Qu, E. Blasco, C. Barner-Kowollik, and M. Wegener, "Rapid Assembly of Small Materials Building Blocks (Voxels) into Large Functional 3D Metamaterials," Adv. Funct. Mater. **30**, 1907795 (2020).
123. J. Lölsberg, A. Cinar, D. Felder, G. Linz, S. Djeljadini, and M. Wessling, "Two-Photon Vertical-Flow Lithography for Microtube Synthesis," Small **15**, 1901356 (2019).
124. S. Chen, Y. Cao, M. Sarparast, H. Yuan, L. Dong, X. Tan, and C. Cao, "Soft Crawling Robots: Design, Actuation, and Locomotion," Adv. Mater. Technol. **5**, 1900837 (2020).
125. D. J. Preston, H. J. Jiang, V. Sanchez, P. Rothemund, J. Rawson, M. P. Nemitz, W.-K. Lee, Z. Suo, C. J. Walsh, and G. M. Whitesides, "A soft ring oscillator," Sci. Robot. **4**, (2019).
126. D. J. Preston, P. Rothemund, H. J. Jiang, M. P. Nemitz, J. Rawson, Z. Suo, and G. M. Whitesides, "Digital logic for soft devices," Proc. Natl. Acad. Sci. **116**, 7750–7759 (2019).
127. N. Vasios, A. J. Gross, S. Soifer, J. T. B. Overvelde, and K. Bertoldi, "Harnessing Viscous Flow to Simplify the Actuation of Fluidic Soft Robots," Soft Robot. **7**, 1–9 (2019).
128. M. Schaffner, J. A. Faber, L. Pianegonda, P. A. Rühs, F. Coulter, and A. R. Studart, "3D printing of robotic soft actuators with programmable bioinspired architectures," Nat. Commun. **9**, 878 (2018).
129. M. Soreni-Harari, R. St. Pierre, C. McCue, K. Moreno, and S. Bergbreiter, "Multimaterial 3D Printing for Microrobotic Mechanisms," Soft Robot. **7**, 59–67 (2019).
130. P. Cabanach, A. Pena-Francesch, D. Sheehan, U. Bozuyuk, O. Yasa, S. Borros, and M. Sitti, "Zwitterionic 3D-Printed Non-Immunogenic Stealth Microrobots," Adv. Mater. **32**, 2003013 (2020).
131. C. Velez, D. K. Patel, S. Kim, M. Babaei, C. R. Knick, G. L. Smith, and S. Bergbreiter, "Hierarchical Integration of Thin-Film NiTi Actuators Using Additive Manufacturing for Microrobotics," J. Microelectromechanical Syst. **29**, 867–873 (2020).

132. J. Kim, M. Kang, E. C. Jensen, and R. A. Mathies, "Lifting Gate Polydimethylsiloxane Microvalves and Pumps for Microfluidic Control," Anal. Chem. **84**, 2067–2071 (2012).
133. O. D. Rahmanian and D. L. DeVoe, "Single-use thermoplastic microfluidic burst valves enabling on-chip reagent storage," Microfluid. Nanofluidics **18**, 1045–1053 (2015).
134. K. Li, K. Morton, M. Shiu, K. Turcotte, L. Lukic, G. Veilleux, L. Poncelet, and T. Veres, "Normally Closed Microfluidic Valves with Microstructured Valve Seats: A Strategy for Industrial Manufacturing of Thermoplastic Microfluidics with Microvalves," in *2020 IEEE 33rd International Conference on Micro Electro Mechanical Systems (MEMS)* (2020), pp. 1110–1113.
135. J. Kim, A. M. Stockton, E. C. Jensen, and R. A. Mathies, "Pneumatically actuated microvalve circuits for programmable automation of chemical and biochemical analysis," Lab. Chip **16**, 812–819 (2016).
136. S.-J. Kim, R. Yokokawa, S. C. Lesher-Perez, and S. Takayama, "Constant Flow-Driven Microfluidic Oscillator for Different Duty Cycles," Anal. Chem. **84**, 1152–1156 (2012).
137. Z. Li and S. Kim, "Characterization of Constant Flow-Driven Microfluidic Oscillator," J. Microelectromechanical Syst. **29**, 68–75 (2020).
138. R. F. Shepherd, F. Ilievski, W. Choi, S. A. Morin, A. A. Stokes, A. D. Mazzeo, X. Chen, M. Wang, and G. M. Whitesides, "Multigait soft robot," Proc. Natl. Acad. Sci. **108**, 20400–20403 (2011).
139. B. Mosadegh, P. Polygerinos, C. Keplinger, S. Wennstedt, R. F. Shepherd, U. Gupta, J. Shim, K. Bertoldi, C. J. Walsh, and G. M. Whitesides, "Pneumatic Networks for Soft Robotics that Actuate Rapidly," Adv. Funct. Mater. **24**, 2163–2170 (2014).
140. S. Ristok, S. Thiele, A. Toulouse, A. M. Herkommer, and H. Giessen, "Stitching-free 3D printing of millimeter-sized highly transparent spherical and aspherical optical components," Opt. Mater. Express **10**, 2370–2378 (2020).
141. A. Sontheimer-Phelps, B. A. Hassell, and D. E. Ingber, "Modelling cancer in microfluidic human organs-on-chips," Nat. Rev. Cancer **19**, 65–81 (2019).
142. W. Yu, H. Lin, Y. Wang, X. He, N. Chen, K. Sun, D. Lo, B. Cheng, C. Yeung, J. Tan, D. D. Carlo, and S. Emaminejad, "A ferrobotic system for automated microfluidic logistics," Sci. Robot. **5**, (2020).
143. A. C. Daly, L. Riley, T. Segura, and J. A. Burdick, "Hydrogel microparticles for biomedical applications," Nat. Rev. Mater. **5**, 20–43 (2020).
144. I. Gharib and M. Sawan, "Microfluidic Valve Arrays for Drug Delivery in Organ-On-Chips," in *2020 42nd Annual International Conference of the IEEE Engineering in Medicine Biology Society (EMBC)* (2020), pp. 5025–5028.
145. J. McGrath, M. Jimenez, and H. Bridle, "Deterministic lateral displacement for particle separation: a review," Lab. Chip **14**, 4139–4158 (2014).
146. S.-C. Kim, B. H. Wunsch, H. Hu, J. T. Smith, R. H. Austin, and G. Stolovitzky, "Broken flow symmetry explains the dynamics of small particles in deterministic lateral displacement arrays," Proc. Natl. Acad. Sci. **114**, E5034–E5041 (2017).

147. L. R. Huang, "Continuous Particle Separation Through Deterministic Lateral Displacement," Science **304**, 987–990 (2004).
148. X. Sun, S. M. Tabakman, W.-S. Seo, L. Zhang, G. Zhang, S. Sherlock, L. Bai, and H. Dai, "Separation of Nanoparticles in a Density Gradient: FeCo@C and Gold Nanocrystals," Angew. Chem. Int. Ed. **48**, 939–942 (2009).
149. B. J. Tauro, D. W. Greening, R. A. Mathias, H. Ji, S. Mathivanan, A. M. Scott, and R. J. Simpson, "Comparison of ultracentrifugation, density gradient separation, and immunoaffinity capture methods for isolating human colon cancer cell line LIM1863-derived exosomes," Methods **56**, 293–304 (2012).
150. V. Sharma, K. Park, and M. Srinivasarao, "Shape separation of gold nanorods using centrifugation," Proc. Natl. Acad. Sci. **106**, 4981–4985 (2009).
151. F.-K. Liu, F.-H. Ko, P.-W. Huang, C.-H. Wu, and T.-C. Chu, "Studying the size/shape separation and optical properties of silver nanoparticles by capillary electrophoresis," J. Chromatogr. A **1062**, 139–145 (2005).
152. X. Xu, K. K. Caswell, E. Tucker, S. Kabisatpathy, K. L. Brodhacker, and W. A. Scrivens, "Size and shape separation of gold nanoparticles with preparative gel electrophoresis," J. Chromatogr. A **1167**, 35–41 (2007).
153. M. Hanauer, S. Pierrat, I. Zins, A. Lotz, and C. Sönnichsen, "Separation of Nanoparticles by Gel Electrophoresis According to Size and Shape," Nano Lett. **7**, 2881–2885 (2007).
154. S. Benfer, P. Árki, and G. Tomandl, "Ceramic Membranes for Filtration Applications — Preparation and Characterization," Adv. Eng. Mater. **6**, 495–500 (2004).
155. E. Krieg, H. Weissman, E. Shirman, E. Shimoni, and B. Rybtchinski, "A recyclable supramolecular membrane for size-selective separation of nanoparticles," Nat. Nanotechnol. **6**, 141–146 (2011).
156. H. Jeon, Y. Kim, and G. Lim, "Continuous particle separation using pressure-driven flow-induced miniaturizing free-flow electrophoresis (PDF-induced μ-FFE)," Sci. Rep. **6**, 19911 (2016).
157. E. Ban, Y. S. Yoo, and E. J. Song, "Analysis and applications of nanoparticles in capillary electrophoresis," Talanta **141**, 15–20 (2015).
158. H. S. Zhou, J. Wang, Z. Zhu, and A. Munir, "Experimental investigation of magnetically actuated separation using tangential microfluidic channels and magnetic nanoparticles," IET Nanobiotechnol. **8**, 102–110 (2014).
159. S. H. S. Lee, T. A. Hatton, and S. A. Khan, "Microfluidic continuous magnetophoretic protein separation using nanoparticle aggregates," Microfluid. Nanofluidics **11**, 429 (2011).
160. S. Dash, S. Mohanty, S. Pradhan, and B. K. Mishra, "CFD design of a microfluidic device for continuous dielectrophoretic separation of charged gold nanoparticles," J. Taiwan Inst. Chem. Eng. **58**, 39–48 (2016).
161. M. Boettcher, S. Schmidt, A. Latz, M. S. Jaeger, M. Stuke, and C. Duschl, "Filtration at the microfluidic level: enrichment of nanoparticles by tunable filters," J. Phys. Condens. Matter **23**, 324101 (2011).
162. H. Jeon, H. Lee, K. H. Kang, and G. Lim, "Ion concentration polarization-based continuous separation device using electrical repulsion in the depletion region," Sci. Rep. **3**, 3483 (2013).

163. A. De Momi and Jamie. R. Lead, "Behaviour of environmental aquatic nanocolloids when separated by split-flow thin-cell fractionation (SPLITT)," Sci. Total Environ. **405**, 317–323 (2008).
164. A. De Momi and Jamie. R. Lead, "Size Fractionation and Characterisation of Fresh Water Colloids and Particles: Split-Flow Thin-Cell and Electron Microscopy Analyses," Environ. Sci. Technol. **40**, 6738–6743 (2006).
165. P. Arosio, T. Müller, L. Mahadevan, and T. P. J. Knowles, "Density-Gradient-Free Microfluidic Centrifugation for Analytical and Preparative Separation of Nanoparticles," Nano Lett. **14**, 2365–2371 (2014).
166. R. T. Davies, J. Kim, S. C. Jang, E.-J. Choi, Y. S. Gho, and J. Park, "Microfluidic filtration system to isolate extracellular vesicles from blood," Lab. Chip **12**, 5202–5210 (2012).
167. A. A. S. Bhagat, S. S. Kuntaegowdanahalli, and I. Papautsky, "Inertial microfluidics for continuous particle filtration and extraction," Microfluid. Nanofluidics **7**, 217–226 (2009).
168. Y. Chen, E. S. Abrams, T. C. Boles, J. N. Pedersen, H. Flyvbjerg, R. H. Austin, and J. C. Sturm, "Concentrating Genomic Length DNA in a Microfabricated Array," Phys. Rev. Lett. **114**, 198303 (2015).
169. M. Xavier, S. H. Holm, J. P. Beech, D. Spencer, J. O. Tegenfeldt, R. O. C. Oreffo, and H. Morgan, "Label-free enrichment of primary human skeletal progenitor cells using deterministic lateral displacement," Lab. Chip **19**, 513–523 (2019).
170. K. Kwek Zeming, N. V. Thakor, Y. Zhang, and C.-H. Chen, "Real-time modulated nanoparticle separation with an ultra-large dynamic range," Lab. Chip **16**, 75–85 (2016).
171. B. H. Wunsch, J. T. Smith, S. M. Gifford, C. Wang, M. Brink, R. L. Bruce, R. H. Austin, G. Stolovitzky, and Y. Astier, "Nanoscale lateral displacement arrays for the separation of exosomes and colloids down to 20 nm," Nat. Nanotechnol. **11**, 936–940 (2016).
172. J. T. Smith, B. H. Wunsch, N. Dogra, M. E. Ahsen, K. Lee, K. K. Yadav, R. Weil, M. A. Pereira, J. V. Patel, E. A. Duch, J. M. Papalia, M. F. Lofaro, M. Gupta, A. K. Tewari, C. Cordon-Cardo, G. Stolovitzky, and S. M. Gifford, "Integrated nanoscale deterministic lateral displacement arrays for separation of extracellular vesicles from clinically-relevant volumes of biological samples," Lab. Chip **18**, 3913–3925 (2018).
173. B. H. Wunsch, S.-C. Kim, S. M. Gifford, Y. Astier, C. Wang, R. L. Bruce, J. V. Patel, E. A. Duch, S. Dawes, G. Stolovitzky, and J. T. Smith, "Gel-on-a-chip: continuous, velocity-dependent DNA separation using nanoscale lateral displacement," Lab. Chip **19**, 1567–1578 (2019).
174. R. Ashton, C. Padala, and R. S. Kane, "Microfluidic separation of DNA," Curr. Opin. Biotechnol. **14**, 497–504 (2003).
175. P. Juskova, A. Ollitrault, M. Serra, J.-L. Viovy, and L. Malaquin, "Resolution improvement of 3D stereo-lithography through the direct laser trajectory programming: Application to microfluidic deterministic lateral displacement device," Anal. Chim. Acta **1000**, 239–247 (2018).

176. P. Jusková, L. Matthys, J.-L. Viovy, and L. Malaquin, "3D deterministic lateral displacement (3D-DLD) cartridge system for high throughput particle sorting," Chem. Commun. **56**, 5190–5193 (2020).
177. J. A. Davis, D. W. Inglis, K. J. Morton, D. A. Lawrence, L. R. Huang, S. Y. Chou, J. C. Sturm, and R. H. Austin, "Deterministic hydrodynamics: Taking blood apart," Proc. Natl. Acad. Sci. **103**, 14779–14784 (2006).
178. K. Loutherback, K. S. Chou, J. Newman, J. Puchalla, R. H. Austin, and J. C. Sturm, "Improved performance of deterministic lateral displacement arrays with triangular posts," Microfluid. Nanofluidics **9**, 1143–1149 (2010).
179. T. Zhang, Z.-Y. Hong, S.-Y. Tang, W. Li, D. W. Inglis, Y. Hosokawa, Y. Yalikun, and M. Li, "Focusing of sub-micrometer particles in microfluidic devices," Lab. Chip **20**, 35–53 (2020).
180. E. Kim, S. Jeon, H.-K. An, M. Kianpour, S.-W. Yu, J. Kim, J.-C. Rah, and H. Choi, "A magnetically actuated microrobot for targeted neural cell delivery and selective connection of neural networks," Sci. Adv. **6**, eabb5696 (2020).
181. H. Ceylan, I. C. Yasa, O. Yasa, A. F. Tabak, J. Giltinan, and M. Sitti, "3D-Printed Biodegradable Microswimmer for Theranostic Cargo Delivery and Release," ACS Nano **13**, 3353–3362 (2019).
182. E. Sungur, M.-H. Li, G. Taupier, A. Boeglin, M. Romeo, S. Méry, P. Keller, and K. D. Dorkenoo, "External stimulus driven variable-step grating in a nematic elastomer," Opt. Express **15**, 6784–6789 (2007).
183. H. Zeng, D. Martella, P. Wasylczyk, G. Cerretti, J.-C. G. Lavocat, C.-H. Ho, C. Parmeggiani, and D. S. Wiersma, "High-Resolution 3D Direct Laser Writing for Liquid-Crystalline Elastomer Microstructures," Adv. Mater. **26**, 2319–2322 (2014).
184. H. Zeng, P. Wasylczyk, D. S. Wiersma, and A. Priimagi, "Light Robots: Bridging the Gap between Microrobotics and Photomechanics in Soft Materials," Adv. Mater. **30**, 1703554 (2018).
185. A. Barbot, M. Power, F. Seichepine, and G.-Z. Yang, "Liquid seal for compact micropiston actuation at the capillary tip," Sci. Adv. **6**, eaba5660 (2020).
186. J. Wang, J. Coburn, C.-P. Liang, N. Woolsey, J. C. Ramella-Roman, Y. Chen, and T. J. Pfefer, "Three-dimensional printing of tissue phantoms for biophotonic imaging," Opt. Lett. **39**, 3010–3013 (2014).
187. Y. Liu, P. Ghassemi, A. Depkon, M. I. Iacono, J. Lin, G. Mendoza, J. Wang, Q. Tang, Y. Chen, and T. J. Pfefer, "Biomimetic 3D-printed neurovascular phantoms for near-infrared fluorescence imaging," Biomed. Opt. Express **9**, 2810–2824 (2018).
188. N. Kedia, Z. Liu, R. D. Sochol, J. Tam, D. X. Hammer, and A. Agrawal, "3-D printed photoreceptor phantoms for evaluating lateral resolution of adaptive optics imaging systems," Opt. Lett. **44**, 1825–1828 (2019).
189. A. C. Scheiwe, S. C. Frank, T. J. Autenrieth, M. Bastmeyer, and M. Wegener, "Subcellular stretch-induced cytoskeletal response of single fibroblasts within 3D designer scaffolds," Biomaterials **44**, 186–194 (2015).
190. D. Serien and S. Takeuchi, "Multi-Component microscaffold with 3D spatially defined proteinaceous environment," ACS Biomater. Sci. Eng. **3**, 487–494 (2017).

191. B. Richter, V. Hahn, S. Bertels, T. K. Claus, M. Wegener, G. Delaittre, C. Barner-Kowollik, and M. Bastmeyer, "Guiding cell attachment in 3D microscaffolds selectively functionalized with two distinct adhesion proteins," Adv. Mater. **29**, 1604342 (2017).
192. S. Du and G. Drazer, "Gravity driven deterministic lateral displacement for suspended particles in a 3D obstacle array," Sci. Rep. **6**, 31428 (2016).
193. K. K. Zeming, S. Ranjan, and Y. Zhang, "Rotational separation of non-spherical bioparticles using I-shaped pillar arrays in a microfluidic device," Nat. Commun. **4**, 1625 (2013).
194. S. Ranjan, K. Kwek Zeming, R. Jureen, D. Fisher, and Y. Zhang, "DLD pillar shape design for efficient separation of spherical and non-spherical bioparticles," Lab. Chip **14**, 4250–4262 (2014).